WASP: a **Wa**sp-inspired **S**urgery needle for **P**rostate cancer procedures

Design and prototyping of a low-friction actuation mechanism

Zola Fung-A-Jou

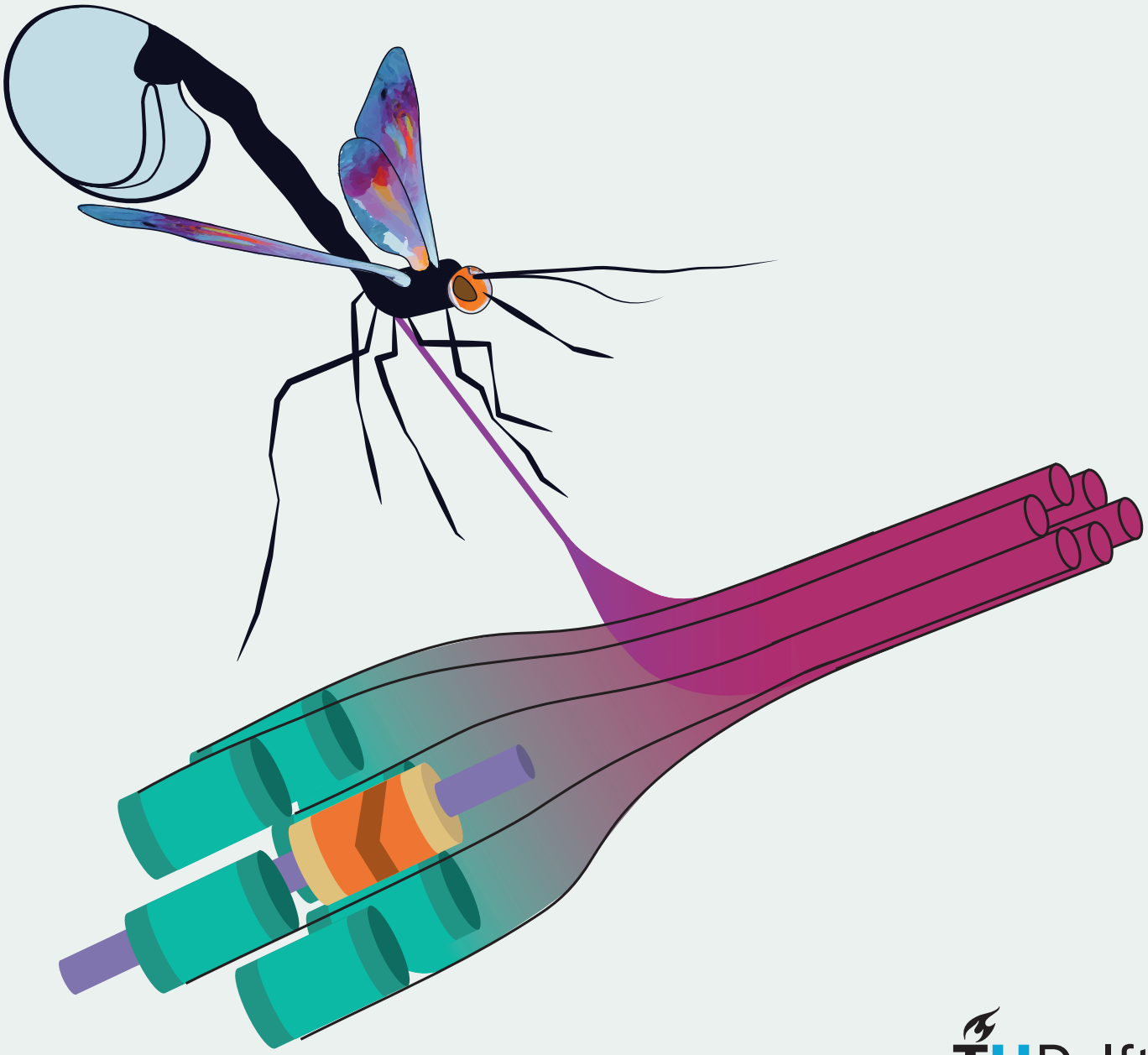

Delft University of Technology

TU Delft

WASP: a **Wa**sp-inspired **S**urgery needle for **P**rostate cancer procedures

Design and prototyping of a low-friction actuation mechanism

by

Zola Fung-A-Jou

to obtain the degree of

Master of Science
in Mechanical Engineering

at the Delft University of Technology,
to be defended on Tuesday December 19, 2023 at 10:45 AM.

Student number:	4459121	
Project duration:	September 1, 2022 – Tuesday 5th December, 2023	
Supervisors:	Ir. J. Bloemberg	TU Delft
	Prof. dr. ir. P. Breedveld	TU Delft
Thesis committee:	Prof. dr. ir. P. Breedveld	TU Delft
	Dr. ir. T. Horeman	TU Delft
	Ir. J. Bloemberg	TU Delft

This thesis is confidential and cannot be made public until December 19, 2025.

All illustrations (including the cover design) are made by: Zola Fung-A-Jou

An electronic version of this thesis is available at `http://repository.tudelft.nl/`.

TU Delft

Preface

I believe that adopting a nature-centred perspective instead of human-centred perspective can contribute to a better world. Nature-centred meaning we position ourselves as humankind within a system equal to all organisms, instead of thinking of ourselves as superior to other organisms. This philosophy matches (in my eyes) with the bio-inspired philosophy: if we design and shape our world more like nature does, we would produce less waste, use less energy and create a more friendly world for all organisms, which in the end will also be beneficial to us as human kind.

Studying at the TU Delft and meeting all the people along the way led to developing this vision. This thesis combines the parts I discovered to be most font of, my love for creating and designing fuelled by my bachelor Industrial Design and the switch to Mechanical Engineering where I learned to design on a more fundamental level. Combine that with my fascination for nature and the result is my master thesis, which I worked on for the past months with ups and downs, joy and some tears.

I would like to give a special thanks to my supervisors: Jette Bloemberg, my daily supervisor, who always had the right thing to say to support me on both an intellectual and personal level throughout this process and Paul Breedveld, for the inspiring, sometimes overwhelming, but enjoyable meetings. Secondly, I want to thank my friends and family. My parents, Eugénie and Christian, for always supporting me and encouraging me to discover and learn. My brothers, Quinten and Xavier, I am grateful to study and live in the same city and continue growing up together. Anouk, Isa, Miek, Mynne, Robbert, Romée, Willem and of course Sam, thank you for being there for me during the project to cheer me up when needed.

With that being said, enjoy reading my thesis!

Zola Fung-A-Jou
Rotterdam, December 2023

Samenvatting

Ik denk dat een verandering van perspectief waar de mens centraal staat naar een perspectief een waar de natuur centraal staat kan bijdragen aan een betere wereld, waar we de mens als organisme plaatsen tussen andere organismes in plaats van superieur eraan. Deze filosofie is naar mijns inzien in lijn met het bio-geïnspireerde ontwerpen. Als we onze wereld meer zouden vormgeven als de natuur zouden we minder afval produceren, minder energie verbruiken en een aangenamere wereld creëren voor alle organismen, wat uiteindelijk ook voor verbetering zou leiden voor onszelf als mensheid. Deze scriptie combineert mijn favoriete onderwerpen die ik tijdens mijn tijd op de TU Delft heb ontdekt. Allereerst, mijn liefde voor creëren en ontwerpen, dat ik heb kunnen ontwikkelen tijdens mijn bachelor Industrieel Ontwerpen. Daarnaast de overstap naar Werktuigbouwkunde waar ik leerde ontwerpen op een meer fundamenteel level en als laatste mijn fascinatie voor de natuur. Het resultaat van deze combinatie is mijn masterscriptie waaraan ik de afgelopen maanden heb gewerkt met hoogte- en dieptepunten, vreugde en enkele tranen.

In dit verslag staat het ontwerp en prototype van de WASP: een naald geschikt voor prostaatkanker behandelingen, geïnspireerd op de legboor (eileider) van de parasiete sluipwesp. Prostaatkanker is de op één na meest vastgestelde kanker bij mannen, met meer dan 1,4 miljoen gevallen wereldwijd per jaar. Een minimaal invasieve behandeling voor prostaatkanker is transperineale laserablatie (TPLA), waarbij een naald de prostaat wordt ingebracht met een laservezel, om zo lokale celdood te veroorzaken. Uitdagingen van TPLA, zoals misplaatsing van de naald door knik, kunnen worden opgelost door te kijken naar het mechanisme van de legboor van de sluipwesp. De sluipwesp kan namelijk weefsel binnendringen met nul netto externe kracht, dankzij een slim duw- en trekmechanisme. De legboor bestaat uit drie segmenten die over de lengte in elkaar haken en ten opzichte van elkaar kunnen schuiven. Bij het binnendringen van een weefsel duwt de wesp één segment naar voren terwijl ze de anderen naar achter trekt met dezelfde externe kracht. Deze beweging genereert wrijvings- en snijkrachten tussen de legboor en het weefsel. Als de wrijvingskrachten van de teruggetrokken segmenten groter zijn dan de wrijvings- en snijkachten van het geduwde segment, beweegt de legboor naar voren met nul netto externe kracht, en verlaagt zo het risico op knik en weefselschade.

De WASP is ontwikkeld volgens hetzelfde principe: zes naaldsegmenten zijn aan elkaar bevestigd met een krimpkous en bewegen in lengte ten opzichte van elkaar. Dit gebeurd in een repeterende beweging, waarbij steeds één van de naaldsegmenten naar voren wordt geduwd en er tegelijkertijd vijf naaldsegmenten naar achteren worden getrokken. Om deze repeterende beweging mogelijk te maken worden de naaldsegmenten worden geduwd en getrokken door een ronddraaiend nokkenmechanisme. Een aandrijfmechanisme is ontworpen zodat de uroloog een koppel kan overbrengen naar het nokkenmechanisme, terwijl een translatie in de lengte as mogelijk is en de naald in stilstaand weefsel kan voortbewegen. Experimenten tonen aan dat de WASP succesvol kan voortbewegen in gelatineconcentraties tot 15 wt% (stijfheid vergelijkbaar met menselijk weefsel). De WASP genereerde een kleine netto duwkracht (F_{push} = 0,18 N) en kan hierom niet volledig als zelfaandrijvend worden beschouwd. Desalniettemin is de netto duwkracht aanzienlijk verminderd in vergelijking met handmatige naald inbrenging en voorkomt de WASP knik. Ook liet een experiment zien dat de WASP een lager gemiddelde slip ratio heeft in vergelijking met eerdere studies, wat zou kunnen suggereren dat een kleine netto duwkracht gunstig, mits knik wordt voorkomen. De vervolgstappen om implementatie van de WASP mogelijk te maken zijn een gebruikersonderzoek en het implementeren van een stuurmechanisme. Zo draagt de WASP bij aan de innovatie van minimaal invasieve chirurgie voor prostaatkanker.

Graag dank ik een aantal mensen zonder wie dit project niet mogelijk was. Allereerst mijn begeleiders: Jette Bloemberg, mijn dagelijkse begeleider, voor alle steun tijdens het project, zowel op persoonlijk vlak waar je altijd het juiste wist te zeggen, als inspiratie om verder te komen in het project. Paul Breedveld, bedankt voor de inspirerende en altijd gekke vergaderingen. Als tweede wil ik mijn familie en vrienden bedanken. Mijn ouders, Eugénie en Christian, voor de steun en aanmoediging om te leren en zelf op onderzoek uit te gaan. Mijn broers, Quinten en Xavier, ik waardeer het dat we in dezelfde stad hebben kunnen studeren en door konden gaan met samen opgroeien. Anouk, Annemiek, Isa, Mynne, Robbert, Romée, Willem en natuurlijk Sam, bedankt dat jullie er voor mij waren tijdens om me op te vrolijken wanneer dat nodig was. De rest van het verslag is in het engels, desondanks veel leesplezier toegewenst!

Contents

WASP: a Wasp-inspired Surgery needle for Prostate cancer procedures

Design and prototyping of a low-friction actuation mechanism

Zola Fung-A-Jou

Abstract **- Prostate cancer is the second most frequently diagnosed cancer in men. A minimal invasive treatment for prostate cancer is transperineal laser ablation (TPLA), which involves inserting a needle containing a laser fibre into the prostate to induce local cell death. The ovipositor of the parasitoid wasp offers a solution to challenges in TPLA, as the wasp can penetrate substrates with zero net external force, minimising the buckling risk and tissue damage. This paper presents the WASP, a design and prototype of a manually actuated needle for TPLA. The actuation mechanism of the WASP transfers a torque while allowing a low-friction translation in the positive y-direction, enabling the needle to travel through stationary tissue. An integrated cam mechanism allows repetitive motion of the needle rods actuated by a single rotation of the urologist. Evaluation of the WASP showed successful travelling through gelatin concentrations up to 15 wt%, a stiffness comparable to human tissue. The WASP generated a small net push force (F_{push} = 0.18 N) and cannot be considered fully self-propelling. Nonetheless, the net push force is notably reduced compared to manual needle insertion and effectively prevents buckling. A performance experiment showed a lower average slip ratio compared to previous studies, which may suggest that a small net push force is beneficial if buckling is prevented. Future steps contain implementing user research and a steering mechanism, to continue innovating minimally invasive surgery for prostate cancer.**

Keywords **- Bioinspiration, Medical, Non invasive surgery, Buckling, TPLA**

Abbreviations

Abbreviation	Definition
2D	Two dimensional
3D	Three dimensional
MRI	Magnetic Resonance Imaging
PMMA	Polymethyl methacrylate
TPLA	Transperineal focal laser ablation
TRUS	Transrectal ulstrasound

1. Introduction

1.1. Transperineal Laser Ablation

The prostate is a male reproductive organ positioned between the penis and bladder outlet (Figure 1). It has a diameter of 4 cm and weighs 30 grams, making it similar in size to a walnut [1]. The primary functions are the production of seminal fluid and regulation of urine [1]. These fluids are carried by the urethra that passes through the prostate [1]. Prostate cancer develops when malignant cells (i.e., cancerous cells) grow within the prostate. It is the second most frequently diagnosed cancer in men and the fourth most common cancer overall [2]. In 2020, over 1.4 million cases of prostate cancer were identified worldwide, with a mortality rate of 375,000 [2]. Death from prostate cancer mainly occurs when cancer cells spread to nearby organs, such as the bladder and bones [3]. There are several treatment options available including invasive procedures, such as surgical removal of the prostate or non-invasive methods like radiation therapy [3]. However, these treatment options can cause incontinence or erectile dysfunction [4].

A novel solution for treating prostate cancer is transperineal laser ablation (TPLA), a local therapy based on laser-tissue interaction to induce cell death [5]. During the procedure the patient

lays in lithonomy position (i.e., on its back with the legs spread upwards) (Figure 2). A transrectal ulstrasound (TRUS) probe is inserted into the rectum to acquire real-time two-dimensional (2D) images of the prostate. Prior to the procedure, an MRI scan was conducted to identify malignant cells that are not clearly visible on the TRUS images. This MRI scan is used as an overlay onto the TRUS probe images, a technique known as MRI-TRUS image fusion. A grit is placed over the MRI-TRUS image (digital) and on the TRUS probe in front of the perineum (physical). The urologist places the needle into grit position to reach the cancerous area. Once the tumour is reached, the laser fiber inside the needle generates light-induced thermal heating that results in cell death (i.e., coagulative necrosis) around the fiber tip [6].

TPLA is a local treatment that requires only local anaesthesia and is minimal invasive, both factors contribute to a short patient recovery time [7, 8]. A challenge in current TPLA procedures is needle placement errors, the difference between the needle tip position and its intended position. Factors that contribute to needle placement errors are, target movement due to patient movement, prostate shape alternations due to the pressure of the TRUS probe or needle, path obstruction (e.g., large blood vessels), human errors and needle deflection inside the tissue [9–12]. Currently, urologists adjust the needle position by pushing and pulling the needle during the procedure [11]. Thereby risking needle buckling and tissue damage, potentially leading to complications and longer recovery time of the patient [13]. Moreover, it can be problematic if the tumour is not reached in the centre, since the centre of the tumour is most aggressive and the thermal heating generated by the laser fibre is weaker towards its ends [14].

1.2. Wasp ovipositor-inspired needles

One way of improving the current TPLA procedure is looking at nature for inspiration, in particular the parasitoid wasp. The parasitoid wasp has an ovipositor (i.e., egg-laying channel), that is used for penetrating soft and hard substrates to inject its eggs into a host (Figure 3a). Interestingly, the wasp can execute this without buckling of its long and slender ovipositor, due to a push and pull mechanism. The ovipositor exists of one dorsal valve and two ventral valves, which are connected with a dovetail interlocking mechanism allowing them to slide with respect to each other (Figure 3b,3c). When penetrating the substrate, the wasp applies an external force (F_{ext}) to

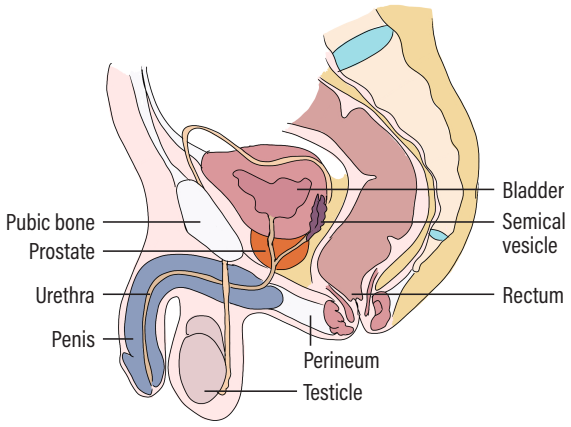

Figure 1: Schematic drawing of the male reproduction organs, the prostate is indicated in orange.

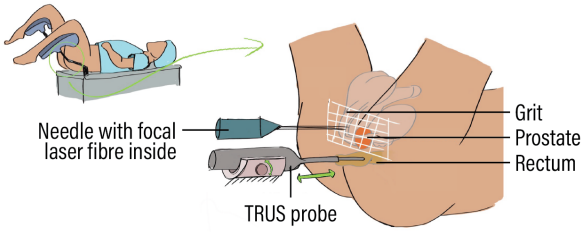

Figure 2: Transperineal laser ablation (TPLA) procedure. On the top left an illustration of the patient in lithonomy position and on the right a close-up of the perineum area, where the transrectal ultrasound (TRUS) probe is inserted into the rectum and the needle is inserted into the perineum via the grit to get to the desired position inside the prostate (orange).

push one valve while pulling the others in opposite direction with the same external force. This movement generates friction forces between the valve and substrate (F_{sub}), between the valves (F_{val}) and cutting forces at the tip (F_{tip}) (Figure 3d). The friction forces between the valves cancel each other out and the sum of the friction and cutting forces of the pulling valve overcome the sum of the friction and cutting forces of the pushed valve. Consequently, the wasp can penetrate the substrate with zero net external force (Figure 3d) [15].

This push-and-pull mechanism of the wasp reduces buckling risk, tissue damage and is suitable for steering [18]. The parallel needle rods move separately from each other, creating a discrete bevel tip that leads to asymmetrical forces acting on the tip, causing the needle to bend in a curved trajectory [18]. Several research groups use the push-and-pull principle of the wasp to innovate medical needles. Matheson & Rodriguez y Baena [19] studied the dovetail interlocking mechanism of the needle rods and focused on the control of these rods. However, this complex

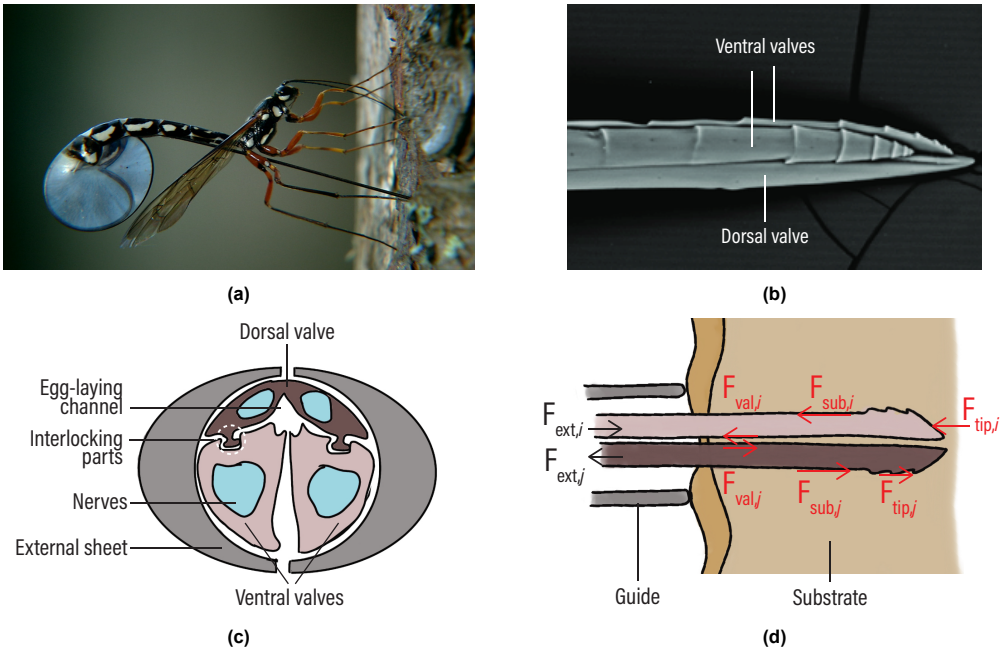

Figure 3: The parasitoid wasp and its ovipositor. (a) Photo of the ichneumon parasitoid wasp [16]. (b) SEM image of the ovipositor of the Ichneumon wasp with its three valves clearly distinguishable, adapted from [17]. (c) Intersection of the ovipositor and its parts. (d) Working principle of the ovipositor, two valves retract while one valve advances creating a higher backward friction force than forward, resulting in penetration with zero net external force.

mechanism resulted in a large outer diameter of 2.5 mm. Scali *et al.* [20] studied a less complex interlocking design in order to decrease diameter size and reached an outer diameter of 0.4 mm. They also researched the required amount of needle rods and the rod motion. Bloemberg *et al.* [21] continued on the work of Scali *et al.* [20] and developed a self-propelling needle that uses the friction and cutting forces acting on the needle to advance through tissue. One needle rod is advanced over a stroke distance while the others are retracted over a fifth of the stroke distance (Figure 4). A self-propelling motion is established if Equation 1.1 is satisfied. That is if the sum of the friction forces of the retracting needle rods ($F_{\mathrm{f},j}$) overcome the sum of the friction and cutting force of the advancing needle rod ($F_{\mathrm{f},i} + F_{\mathrm{c},i}$).

$$\sum F_{\mathrm{f},j} \geq \sum (F_{\mathrm{f},i} + F_{\mathrm{c},i}) \tag{1.1}$$

1.3. Research goal

The current prototypes of wasp-inspired self-propelling needles were build for experimental setups that do not take into account the needle-urologist interaction [19–23]. Most designs actuate the needle rods with individual actuators and electromotors [20, 22, 24]. Bloemberg *et al.* [21]'s design was proved the self-propelling principle of the needle while being actuated by the urologist's hand. However, the needle and actuation unit remained stationary, while the tissue (phantom) was placed on a low-friction cart and pulled over the needle. In clinical practice, the opposite is desired, where the patient remains stationary and the urologist moves the needle through the tissue, steering when necessary, to reach the tumour target. Therefore, the goal of this project is to design and characterise a low-friction needle device for TPLA procedures that uses the self-propelling principle of the parasitoid wasp and can travel through stationary human-like tissue.

1.4. Report structure

Firstly, Section 2 elaborates on the problem and presents the requirements to reach the goal of this project. Section 3 shows the chosen design direction and the final design of the needle device. The manufactured prototype is shown in Section 4, which was tested and evaluated in Section 5. The results of these tests and the limitations of the design are discussed in Section 6, as well as a future perspective of the project. Lastly, a conclusion is made in Section 7.

2. Requirements

2.1. Needle system must-haves

The total needle device consists of two systems: (1) the needle system and (2) the actuation system (Figure 5). The needle system consists of

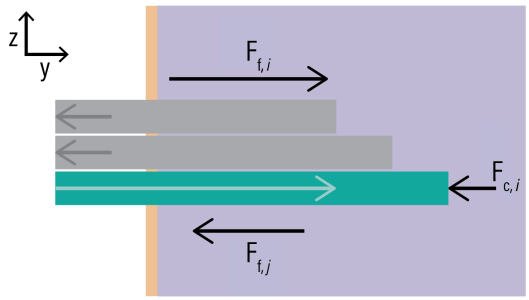

Figure 4: Self-propelling principle. One advancing needle rod (green) generates a friction force ($F_{\mathrm{f},i}$) and cutting force $F_{\mathrm{c},i}$ between the tissue (purple) and two retracting needle rods (grey) generate a friction force ($F_{\mathrm{f},j}$) in the opposite direction [21].

the needle rods that are held together and are able to translate longitudinally with respect to each other in a repetitive motion. The actuation system receives an input from the urologist on one side and acts on the needle rods on the other side. The following requirements for the needle system were established from previous research [20, 21, 25, 26], as the focus of this research is on the actuation system.

1. Self-propelling motion. The self-propelling principle, as described in Section 1.2, was used as starting point of this design to travel through the tissue with a zero external push force [21].

2. Rod sequence. Scali *et al.* [20] researched the rod motion sequence and the corresponding stroke distance (S), to obtain the self-propelling motion. A repetitive motion of one advancing rod and five retracting rods (Figure 6) was chosen, similar to that of Bloemberg *et al.* [21] to compare the design performance.

3. Stroke S [4 mm]. The needle rods need to individually translate back and forth with respect to each other with a stroke distance of S. A stroke value of S = 4.0 mm as found by Scali *et al.* [25] is used to compare the design performance.

4. Number of needle rods [6]. To maintain the self-propelling motion the retracting/advancing rod ratio should be greater than one. Previous research showed that a number of six needle rods is desired and is therefore chosen [25].

5. Total outer needle diameter [<0.9 mm]. A maximum outer diameter of the needle bundle was chosen to be 0.9 mm, to be competitive with the 21-gauge (OD = 0.819 mm) needles used in TPLA procedures [5].

6. Rod length [>100 mm]. The minimal needle rod length is based on the depth of the prostate measured from the perineum. A working distance of 100 mm is sufficient to reach the entire prostate [27, 28].

2.2. Actuation system must-haves

2.2.1. Coupling needle rods

The following requirements were derived from the coupling between the needle rods and the actuation unit.

7. Translate horizontally in the y-direction [S]. The coupling with the needle rods should allow the needle rods to translate with respect to each other in the positive and negative y-direction with a work range S.

8. Travel in the y-direction [>100 mm]. The coupling should allow the needle rods to travel in the positive y-direction over a working distance of 100 mm in order to reach the prostate transperineally.

9. Transfer input motion. The actuation unit should be able to transfer the input motion of the urologist to the output motion needed for the rod sequence.

2.2.2. Interaction urologist

The following requirements resulted from the interaction of the urologist with the actuation unit.

10. Human powered. It was chosen to design a human powered system in order to focus on the needle-urologist interaction. The human gives the power for the movement of the individual needle rods and thereby actuates the needle motion sequence.

11. No interference of the input motion with the self-propelling motion. It is important that the input motion and forces of the urologist do not interfere with the self-propelling motion of the needle, in order for the needle to work and advance through the tissue with zero external push force.

12. Feedback of the needle position [TRUS probe]. The urologist should receive feedback of the needle and tumour position to locate the needle. This feedback is given by the TRUS probe and MRI images as used in the current TPLA procedure (Appendix A).

13. Direct control. The urologist should be able to start and stop the input motion directly i.e., when the urologist stops giving an input the needle rods should stand still.

14. Intuitive control. The actuation and control should be intuitive to minimise the mental load of the urologist. The main tasks is ablating the tumour, which requires all the focus of the urologist.

15. One hand actuation. The urologist should be able the actuate and control the device with one hand, so the other hand is free for remaining tasks of the TPLA procedure.

16. Dimensions [10x10x15 cm^3]. The operating space of the urologist is between the legs of

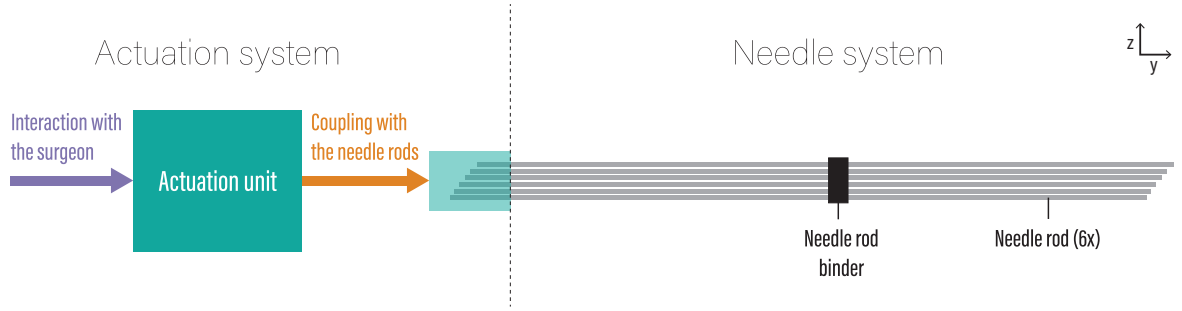

Figure 5: The total needle device with on the right side of the dotted line the needle system and on the left the actuation system.

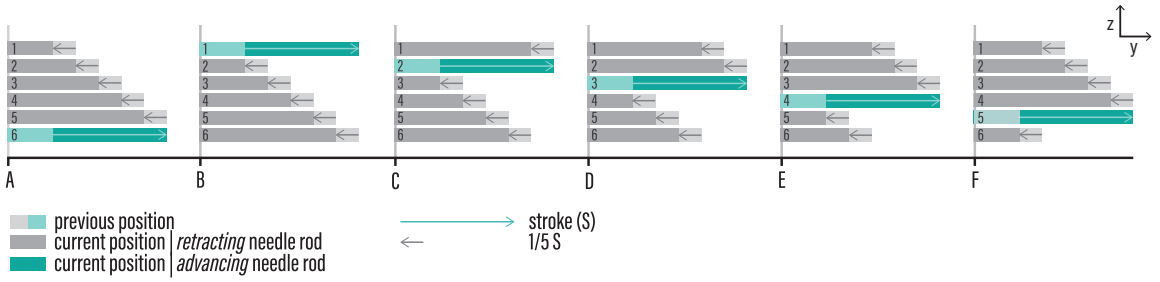

Figure 6: The repetitive needle rod sequence. One needle rod advances (green) over a stroke distance (S) and five needle rods (grey) retract over a fifth of the stroke distance. The letters A-F indicate the steps in the sequence, where each step another rod is advanced. When all rods have advanced once the sequence ends and can start over again.

the patient. The needle device should be working next to other medical instruments such as the TRUS probe with stepper and stabiliser (Appendix A). Therefore dimensions of the actuation system (i.e. without the needle rod length) should be within 10 x 10 x 15 cm^3.

2.3. Overall nice-to-haves

The following nice-to-have requirements make a future version of the design suitable for medical application. The design presented in this study does not have to fulfil these nice-to-have requirements yet, but design decisions made in this study should not obstruct the next version of a design closer to clinical practice.

17. Steering. The main goal of the TPLA procedure is to reach the target area in the centre of where the tumour is located. This requires that the urologist can steer the needle to any desired position.

18. Insertion of a TPLA fibre. To execute a TPLA procedure a laser fibre should be inserted into the tissue. This laser could be integrated as of one of the needle rods or through a hollow core in the needle device.

19. Material energy resistance [1800 J]. The material should be able to resist the energy from the laser fibre used in TPLA, which is 1800 J [5].

20. Material [Magnetic resonance (MR) safe]. If the design will be used inside an MRI scanner the used material should be MR safe. MR safe means that the material poses no known hazards resulting from exposure to any MR environment, which is the case for materials that are electrically nonconductive, nonmetallic and nonmagnetic. This is determined by the ASTM F2503-20 standard [29].

21. Material [Biocompatible with human tissue]. The part of the needle device that is in contact with the human tissue should have an appropriate host response during the TPLA procedure. No harm can occur to the health of both the user (urologist) and the patient. The material should be biocompatible according the ISO 10993 standard [30].

22. The actuation system is reusable. The sustainability of the product is improved, when only the needle rods have to be replaced each procedure. It is important that the reusable part is cleanable according to the ASTM F3208 standard [31].

23. All parts should be accessible and replaceable. If a single component experiences a malfunction, it is not necessary to replace the entire system, which enhances the product's sustainability. The needle rods need to be changed after every procedure for sterility.

To summarise a full list of the requirements is given in Table 2.1.

Table 2.1: List of requirements ordered by the must-haves coming from the needle or actuation systems and nice-to-haves coming from the overall system. The following information presented: the requirement number (#), a description of the requirement, the requirement value and the reasoning behind the requirement.

Must-haves needle system			
#	**Description**	**Value**	**Rational**
1	The self-propelling motion is used	-	See [21]
2	Rod sequence	1 advancing and 5 retracting needle rods	See [20]
3	Stroke distance (S)	4 mm	See [20]
4	Number of needle rods	6	See [20, 21]
5	Total outer needle diameter	<0.9 mm	Compatible with hypodermic needles [5]
6	Needle rod length	>100 mm	Prostate depth [27, 28]
Must-haves actuation system			
#	**Description**	**Value**	**Rational**
7	Translation of needle rods	Positive and negative y-direction	Self-propelling motion [15]
8	Travel in the y-direction	>100 mm	Prostate depth [27, 28]
9	Transfer input motion	-	Get desired output motion
10	Actuation	Manually	Focus on urologist interaction
11	No interference of the input motion with the self-propelling motion	-	Advance through the tissue with zero net external force.
12	Feedback of the needle position	TRUS probe	Used in TPLA [5]
13	Needle actuation	Direct	Minimise mental load
14	Needle actuation	Intuitive	Minimise mental load
15	Needle actuation	One hand	Other hand free for main task
116	Dimensions	< 10x10x15 cm	Stay within the operating space (Appendix A)
Nice-to-haves overall system			
#	**Description**	**Value**	**Rational**
17	Steering by urologist	Desired position	Reach the target area
18	TPLA fibre could be inserted	-	Killing cancerous cells [5]
19	Material energy resistance	1800 J	Resist the energy of the laser fibre [5]
20	Material	MR safe [29]	To use in an MRI scanner
21	Material	Biocompatible with human tissue [30]	Prevent infections
22	Reusability of the needle device	-	Sustainability, cleaned according [31]
23	All parts should be accessible and replaceable	-	Sustainability and sterility

3. Design

3.1. Design direction

As starting point of this design we used Bloemberg *et al.* [21]'s needle as described in Section 1.2. The design of needle system consists of six needle rods that are held together and can slide with translate to each other. The initial requirement is that the needle device uses the self-propelling principle by pushing and pulling the needle rods in a repetitive motion (Figure 6). Each step, one needle rod is advanced in the positive y-direction over a stroke distance (S), while the other five needle rods are retracted in the negative y-direction over a fifth of the stroke distance. The sequence ends when all the needle rods have advanced once.

We chose to design a human-powered actuation system to lay the focus of the design on the mechanism instead of the control. We chose a hand-powered actuation over other human-powered actuation (e.g., using the legs or feet) to shorten the control loop of the device. The actuation is one-handed to leave the other hand free for executing remaining tasks. The level of automation cannot be fully manual, where the urologist actuates each individual needle rod, since this would require high skills and precision of the urologist and would take a lot of mental load [32]. Fully automation is also not suitable, as maintaining the urologist in the loop contributes to the patient's perception of the procedure [33, 34]. Therefore, we chose to design a semi-automated control wherein a single input of the urologist actuates all six needle rods simultaneously. This single input should be direct i.e., when the input is given the needle rod sequence starts and if the input stops, the needle rod sequence stops. The input needs to be intuitive to place minimal mental load on the urologist, whose primary focus is the medical procedure.

3.2. Overall system design

We followed a systematic approach from the Delft Design Guide to fulfil the design direction and meet all the requirements [35]. Firstly, a list of required functions of the actuation system was formed. Secondly, sub-solutions per function were conducted via brainstorming and arranged into a morphological chart (Appendix B, Table B.1). Lastly, the sub-solutions were combined to form concepts. The full design process with corresponding choices and solutions can be found in Appendix B. This section focuses on the two most promising concepts from which the final design was derived.

3.2.1. Actuation

The base structure of the design consist of a rotational input, cam mechanism, transfer cylinders and needle rod holders. This cylindrical mechanism is simplified and visualised in a 2D schematic illustration to show the motion and working principle of the system (Figure 7).

Input motion. To achieve a high level of precision, the urologist needs to employ a small force loop, therefore, we chose to implement a rotational input motion by hand. A manual rotation is actuated from the wrist, creating a force loop from the wrist to the fingers through the rotary knob. This loop is considerably smaller compared to translating a slider, where the force loop goes via the elbow [32]. The input rotation is applied to a drive cylinder (purple) that rotates clockwise. Figure 7(i) illustrates this clockwise rotation around the y-axis as a translation in positive z-direction (white arrow).

Transfer input motion. The core of the design is a mechanism that transfers this rotational input motion around the y-axis, while allowing a translation along this y-axis. This was achieved by placing a follower cylinder (yellow) concentrically over the drive cylinder. Both cylinder have grooves along their lengths in which balls can roll freely, allowing a low-friction translation along the y-axis. Simultaneously, these grooves constrain the translations along the x- and z-axis, transferring the torque from the drive cylinder to the follower cylinder (Figure 7(ii)).

Cam and followers. We chose a cam mechanism to convert the rotational input motion into the required needle rod sequence. The cam is a cylinder (orange) with a cutout V-shaped path (dark orange) along its circumference, in which six followers (pink) roll. Figure 7(iii) shows that the cam is fixed to the follower cylinder and translates in z-direction synchronously.

Needle rods. Six needle rod holders (green) connect the six needle rods to the six followers. When the cam translates in positive z-direction one follower is pushed while the other five are pulled, due to the design of the V-shaped path (Figure 7(iv)). The needle rod holders to which the proximal ends of the needle rods are connected restrict the followers to only translate in the y-direction. This causes one needle rod to move in the positive y-direction and five needle rods in the negative y-direction, executing the needle rod sequence. The distal tips of the needle rods are in contact with the tissue, allowing for the self-propelling motion. The friction forces between the rods and the tissue causes the rod holders, the cam and the follower cylinder to move in the positive y-direction with low friction, due to the ball grooves (Figure 7(v)).

3.2.2. Design considerations

The actuation design with its motion as illustrated in Figure 7 can be configured two ways: (1) with the drive cylinder as the outer cylinder and (2) with the drive cylinder as the inner cylinder, leading to two promising concepts. Concept 1 is built from the outside to the inside (Figure 8a). The drive cylinder (purple) is an outer cylinder in which a follower cylinder (yellow) is placed concentrically. The drive cylinder and follower cylinder have grooves along their lengths in which balls can roll freely, to transfer the rotation of the drive cylinder and allow a translation of the follower cylinder. The cam (orange) is fastened inside the yellow cylinder. Followers (pink) roll in the V-shaped cam path and move back and forth by the rotation of the cam. The followers are connected to rod holders (green) and an inner support (blue) restricts the rod holders to solely a translation in the y-direction. This support also decreases the distance between the needle rods, allowing them to enter the tissue as one needle bundle. To support the whole system two supports are placed at the ends of the drive cylinder in which the drive cylinder can roll freely (transparent).

Concept 2 is build from the inside to the outside (Figure 8b). Here the drive cylinder (purple) is an inner axis over which the follower cylinder is placed concentrically. The drive cylinder and the follower cylinder have grooves along their lengths in which balls roll. A cylindrical cam (orange) is fixed on the outer surface of the follower cylinder, to transfer the torque. Followers (pink) roll in the V-shaped cam path (dark orange) and are connected to the rod holders (green). The rod holders are constrained to only translate in the y-direction by the outer support (blue). This

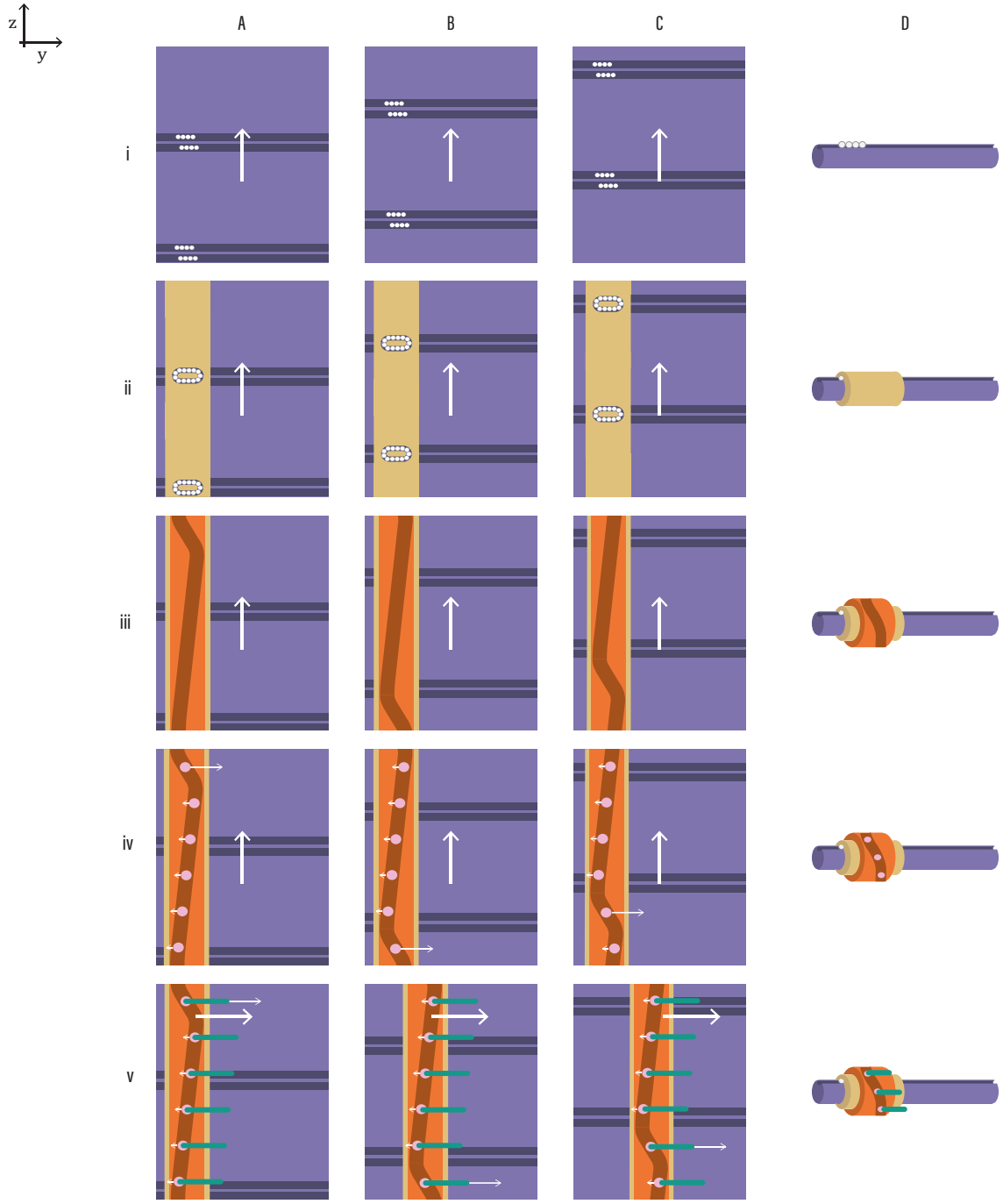

Figure 7: Schematic illustration of the motion of the actuation unit. A-C indicate the two-dimensional (2D) motion at different moments in time. The roman numbers each add a different component of the actuation unit, of which their three-dimensional (3D) representation is presented in column D. The rotations around the y-axis in 3D are represented as translations in the z-direction in 2D. (i) A rotational input in the positive z-direction (white upward arrow) is given to the drive cylinder (purple) that has grooves along its length in which balls roll. (ii) A follower cylinder is attached to the drive cylinder and has the same translation in the positive z-direction. (iii) A cam (orange) is attached to the follower cylinder and also follows this translation. (iv) Six followers (pink) roll in the V-shaped cam path (dark orange) and are pushed in the positive or negative y-direction by the cam path. (v) Six rod holders (green) are attached to the followers to only allow a translation in the y-direction. Due to the friction forces between the needle rods and the tissue the cam (orange) and follower cylinder move in the positive y-direction (white large arrow).

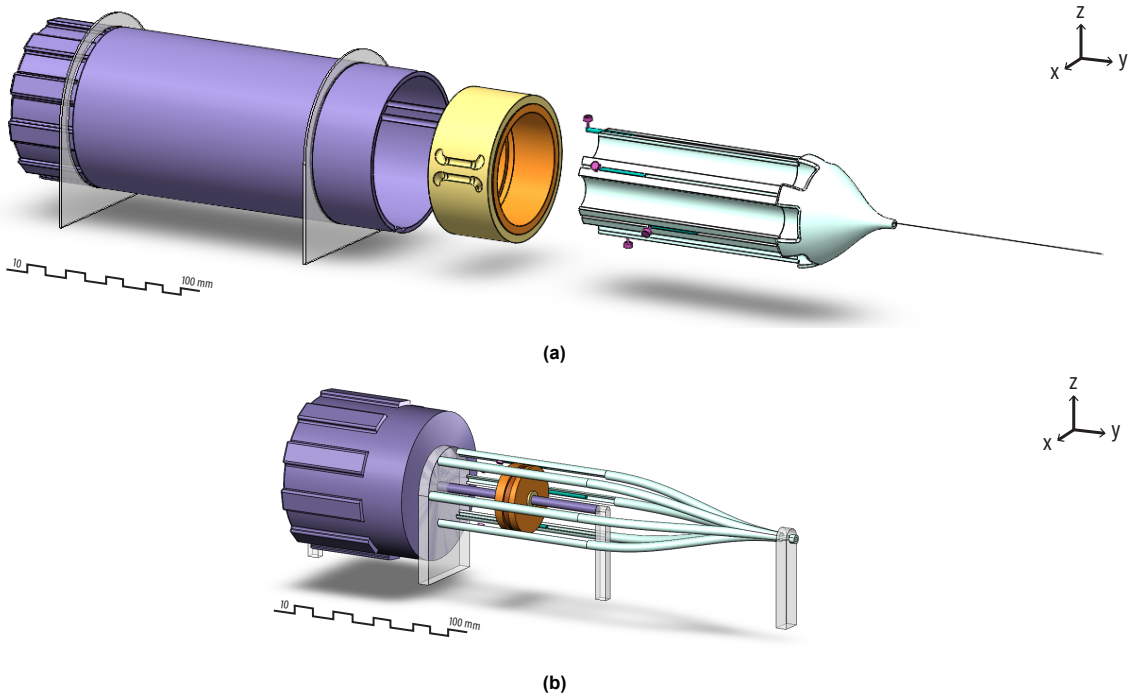

Figure 8: Two design concepts. (a) Concept 1: An outer drive cylinder (purple) and inner follower cylinder (yellow) are connected concentrically with grooves along their lengths in which balls can roll freely. A cam (orange) with a V-shaped cam path is fixed inside the follower cylinder. Six followers (pink) connected to six needle rod holders (green) roll in the V-shaped cam path. An inner rod support (blue) restricts the rod holders to solely a translation in the y-direction and decreases the distance between the needle rods. Two supports (transparent) are placed at the ends of the drive cylinder in which the drive cylinder can rotate freely. (b) Concept 2: An inner drive cylinder (purple) and outer follower cylinder (yellow) are connected concentrically with grooves along their lengths in which balls roll. A cylindrical cam (orange), with a V-shaped cam path (dark orange) is fixed on the outer surface of the follower cylinder. Six followers (pink) connected to six rod holders (green) roll in the V-shaped cam. An outer rod support (blue) constrains the followers to only translate in the y-direction and directs the needle rods towards each other. Two supports (transparent) are placed at the ends of the drive cylinder and one support (transparent) is placed at the end of the needle rod support.

outer support also directs the needle rods towards each other. To support the whole system two supports (transparent) are placed at the ends of the inner axis and one support (transparent) is placed at the end of the needle rod support.

We compared the two concepts to select the most suitable design. A small design is preferred, to minimise the utilised space in the operation room. The dimensions of both concepts are determined by the size of the cam and will be roughly the same. The same applies to the weight of the linear moving components, which should stay low to overcome the friction forces generated in the tissue. Concept 1 appears less complex since the support for guiding the needle rod holders is placed inside the cam, providing a more integrated design compared to placement outside of the cam. Furthermore, the components are protected by the drive cylinder and no extra components are needed as shield. However, manufacturing of the cam is easier when the cam is placed on the outside, as in Concept 2. Another important aspect for the manufacturing is the availability of off-the-shelf parts. For Concept 1 almost all parts require custom fabrication, while for Concept 2 the inner drive and corresponding outer cylinder can be bought off-the-shelf, in the form of a ball spline. We preferred to use this off-the-shelf ball spline, since it is more accurate and available faster than a custom fabricated part, therefore, we chose to prototype Concept 2.

3.2.3. Linear guidance

Figure 9 illustrates the three-dimensional (3D) motion of the final design. The inner drive cylinder (purple) and follower cylinder (yellow) form the ball spline to which the cam (orange) is connected. All three parts rotate due to actuation of the urologist. The cam path pushes the followers (pink) back and forth in the desired needle rod sequence. Linear guidance is needed to constrain the movement of the needle rods such that they can only translate in the y-direction. We connected the needle rod holders to linear guides (green) that are placed concentrically over an

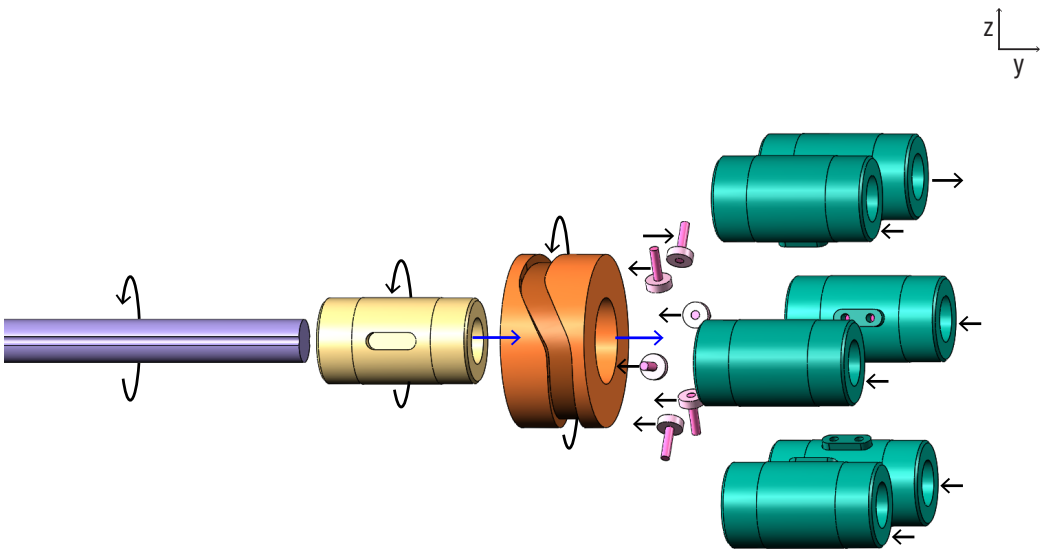

Figure 9: 3D motion of the actuation unit. The urologist gives a rotational input (black arrow) to the drive cylinder (purple). A follower cylinder (yellow) is concentrically attached to the drive cylinder and follows the same rotation. A cam (orange) is fixed to the follower cylinder and also follows the rotation. Six followers (pink) roll in the V-shaped cam path (dark orange) and are pushed in the positive or negative y-direction by the cam path. Six needle rod holders (green) are attached to the followers and six linear guides to only allow a translation in the y-direction. Due to the friction forces between the needle rods and the tissue the cam and follower cylinder travel in the positive y-direction (blue arrows).

axis with grooves in which balls roll with low friction. The needle rods are connected to these linear guides on the proximal end and interact with the tissue on the distal end. The friction forces between the tissue and needle rods should be greater than the friction forces in the actuation system for the system to self-propel through the tissue. Therefore, it is important to keep the friction forces and mass of the parts that translate in the positive y-direction low. This includes the follower cylinder, the cam, the six followers, the six needle rod holders and six moving parts of the linear guides.

3.2.4. Support

For the needle rods, we chose to use six 0.3-mm diameter spring steel rods. Supplementary tests showed that the maximum unsupported rod length for spring steel rods of 0.3-mm diameter is 20 mm (Appendix C). Support of the needle rods is needed in two places: within the actuation unit and between the actuation unit and the tissue. The support within the actuation unit should be able to move along with the translating cam, since the unsupported rod length decreases when the rods are travelling inside the tissue. We chose to implement an origami structure for this support: a tube derived from the Miura-ori folding (Figure 16), that is stiff in z-direction while being flexible in the y-direction

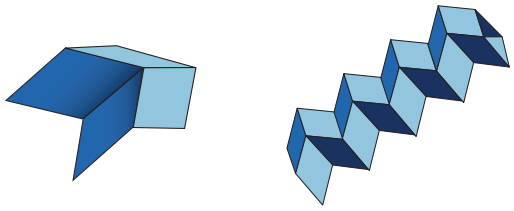

Figure 10: (a) Miura-fold. (b) Miura tube.

[36]. The Miura-ori tube contracts as it is pushed by the cam moving in the positive y-direction. Holes in the Miura-ori tube guide and support the needle rods every 20 mm. The support between the actuation unit and the tissue, should guide the needle rods towards each other. At the actuation side, the needle rods are initially set in a larger diameter than desired when entering the tissue, where the rods should act as a single bundle. To guide the needle rods smoothly from the actuation system to the distal needle tip, an outer support consisting of six S-shaped tubes was designed. These tubes are secured by two supports, one located at the middle and one at the end of the tubes. To hold the entire system, two supports are placed at the ends of the inner drive, in which the inner drive can rotate freely.

4. Prototype

4.1. Manufacturing

A prototype was build for a proof of concept of the design. We chose to not work with MRI compatible components yet, because friction forces in the system are significant and should stay close to zero. Components from MRI compatible materials are often larger in size and have higher friction coefficients. Figure 11a shows an overview of all manufactured parts, which are briefly explained below. A more elaborated overview about the choices made during the production process can be found in Appendix B.

4.1.1. Actuation

Knob (Figure 11a (1)). The surgeon can actuate the needle by turning a knob (blue) and thereby the inner drive cylinder. The knob has a diameter of 66 mm and width of 20 mm, which is an optimal size for grip force execution by both male and female [32]. Knob serrations were added for extra grip [37]. The knob was 3D-printed using the Stereolithography (SLA) printer Formlabs 3+, with the resin Durable V2 (Formlabs). After printing the knob was washed in an alcohol bath and cured under a UV light. A hole was drilled in the centre to attach the knob to the inner drive cylinder of the ball spline.

Ball spline (Figure 11a (4)(6)). We chose to use a ball spline as core mechanism, since it can transfer a torque while allowing a translation with low friction. The ball spline was bought off-the-shelf and is the IKO Nippon Thompson LSAG10C1R200, made of stainless steel. It consist of an inner drive cylinder (purple) and an external follower cylinder (yellow) that are aligned concentrically. The follower cylinder has a 10-mm diameter and a 18-mm length (Figure 11a (7)) and the drive cylinder a diameter of 5 mm (Figure 11a (4)) and length of 100 mm, allowing the needle to travel 100 mm inside the body. The follower cylinder has a mass of 4.9 g. The inner axis has grooves along its length that align with grooves in the follower cylinder, in which 1-mm balls roll. The ball spline was lubricated with penetrating oil (WD40).

Ball bearings (Figure 11a (3)). The drive cylinder of the ball spline was placed between two stainless steel ball bearings to allow a low-friction rotation actuated via the knob. The ball bearings are the NMB DDL-850ZZMTHA1P13LY121 Deep Groove Ball Bearing. They have an outer diameter of 8 mm, an inner diameter of 5 mm and a width of 2.5 mm. These ball bearings were pressed into two support blocks (Figure 11a (2)).

Cam (Figure 11a (7)). A cam was fixed to the follower cylinder of the ball spline by the attached key of the ball spline. A slot with the dimensions of the key was made inside the cam and slid over the follower cylinder. Thereby, the cam follows the rotation of the follower cylinder, which creates a rotation of the V-shaped cam path.

The cam radius ($r_{\mathbf{c}}$) was determined by the available space and the follower radius ($r_{\mathbf{f}}$). A small cam is preferable to reduce the mass and decrease the distance of the needle rods to the centre, resulting in less friction in the overall system. However, a cam radius that is too small can lead to high surface stresses and undercutting, causing the followers to lose contact with the cam path [38]. While cone-shaped followers would be ideal due to the smaller circumference inside than outside the cam path, manufacturing such shapes in small scale is challenging. Therefore, we chose to use off-the-shelf ball bearings as followers (Figure 11a (9)). To prevent undercutting of the followers along the circumference of the cam, an approximately flat surface of the cam path is desired. We sketched the follower and cam path with the corresponding radii r_{c} and r_{f} and the line between the centre of the cam to the corner of the follower, l (Figure 12). We aimed to find the case where $l/r_{\mathrm{c}} \approx 1$, while keeping the cam diameter as small as possible. This was achieved by identifying the l and the r_{c} for $l/r_{\mathrm{c}} = 1 + t$, with t a small threshold that is greater than zero. The smallest bearings found have an r_{f} of 1.5 mm, for this r_{f} we observed that a threshold of t = 0.015 is sufficient to prevent undercutting along the cam circumference. This resulted in an outer cam radius of 9.76 mm, which was rounded to a cam radius of 10 mm. The detailed calculation can be found in Appendix D.2.

The V-shaped cam path design was determined by composing a displacement diagram [38]. One revolution of the cam (i.e., 360°) is equal to one needle rod sequence. Each individual rod is advanced over a stroke distance in one step of 60° and retracted in five steps over the same stroke distance, resulting in the V-shaped path. We chose to design a uniform motion cam, to ensure a uniform velocity throughout the stroke. However, a major disadvantage is that this velocity profile has infinite accelerations at the beginning and end of the stroke, which causes a shock. As prevention, we integrated parabolic curves at the ends of the stroke that reduce the accelerations from infinite to a finite constant. The outcome of the cam path and the corresponding velocities and accelerations are shown in Figure 13, the calculations can be found

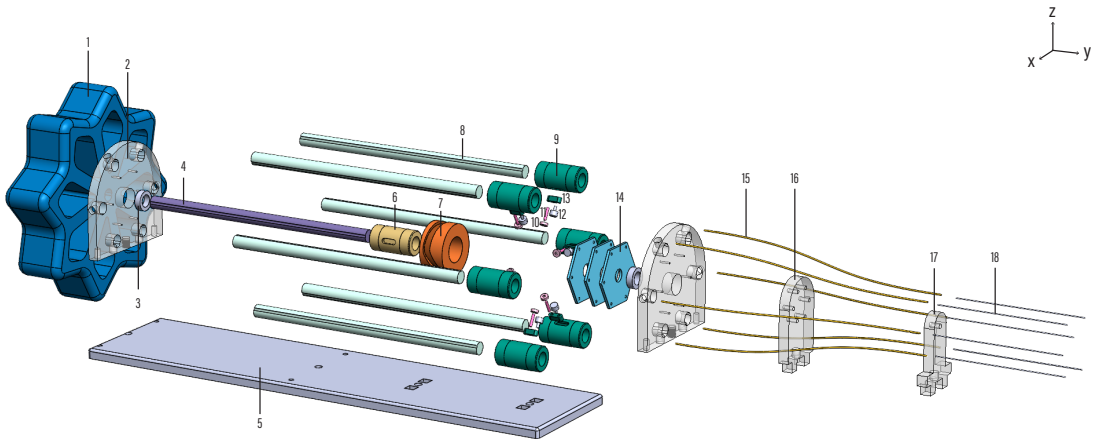

(a)

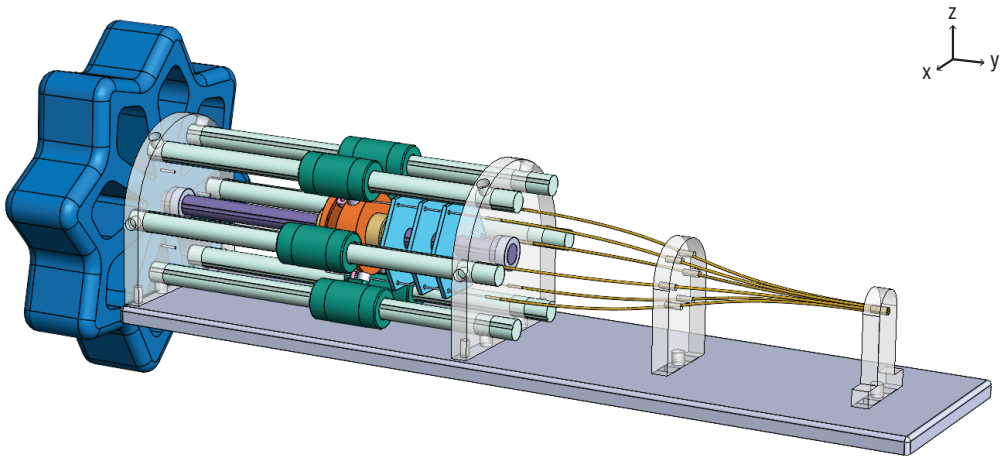

(b)

Figure 11: Computer model of the prototype (SolidWorks). (a) Exploded view of the prototype. Knob (1), support block (2), ball bearing (3), inner drive cylinder of the ball spline (4), base plate (5), follower cylinder of the ball spline (6), cam (7), linear guide axis (8), linear guide follower cylinder (9), cam follower (10), follower axis (11), rod holder (12), key (13), origami structure (14), brass tube (15), tube support middle (16), tube support end (17), needle rod (18). (b) The assembled prototype.

in Appendix B.1.2. To prevent undercutting along the V-shaped cam path, the minimum radius of curvature (ρ_{min}) of the V-shaped cam path cannot be smaller than the radius of the follower (Figure 14). The minimum radius of curvature is located at the parabola top. For a cam radius of 10 mm, the corresponding ρ_{min} 5.14 mm, which is greater than the r_{f} of 1.5 mm. The final dimension of the cam are a diameter of 20 mm, a width of 10 mm and a mass of 16.01 g. The cam is made of aluminium and milled into the desired shape by the Dienst Elektronische en Mechanische Ontwikkeling (DEMO) of the TU Delft.

Followers (Figure 11a (10)(11)). The six followers in the cam are the (stainless) steel NMB DDL-310HA1P25LO1 Deep Groove Ball Bearing. They have an inner diameter of 1 mm, an outer diameter of 3 mm, a width of 1 mm and a mass of 0.03 g. These are the smallest ball bearings found and the outer diameter determines the diameter of the cam and the width of the V-shaped cam path. The followers are fitted into the fixed ball spline follower cylinder key (Figure 11a (11)) with a steel cylindrical pen with 1-mm diameter, 5-mm length and mass of 0.08 g (Jeveka 125-245 HV30 cylindrical pen 1h8 X 5, 2338H8100010005).

4.1.2. Linear guidance

Fixed ball splines (Figure 11a (5)(13)). The axes of six ball splines are fixed between the support blocks to function as linear guides of

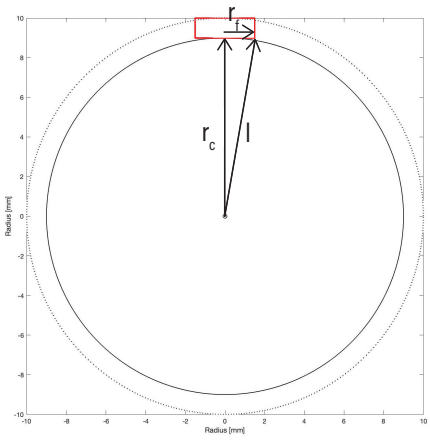

Figure 12: Front view of the cam (black) and follower (red), with the cam radius r_c, follower radius r_f and the line l indicated that are used to determine the minimum cam radius, where undercutting along the cam circumference is prevented.

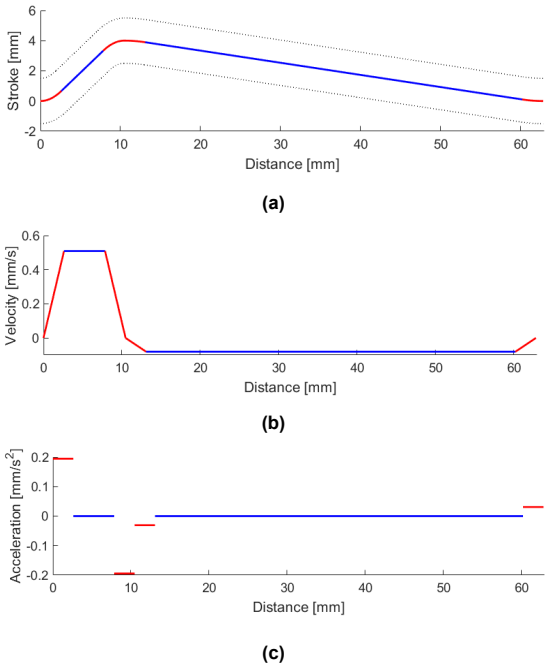

Figure 13: (a) Displacement profile, (b) velocity profile and (c) acceleration profile of the cam. The parabolic functions are indicated in red and the linear functions in blue.

the followers and needle rods (Figure 11a (5)). The follower cylinders (Figure 11a (13)) of these ball splines cannot rotate anymore and only slide along the axis. They are the same IKO Nippon Thompson LSAG10C1R200, with a follower cylinder diameter of 10 mm, an inner axis diameter of 5 mm, a length of 100 mm and a follower cylinder mass of 4.91 g. The ball splines were lubricated with penetrating oil (WD40).

Rod holders (Figure 11a (12)). Six rod holders were attached to the keys and the needle rods to follow the movement of the linear guides, when actuated by the cam. The shape starts with a 1-mm diameter axis with a 1-mm height that fits the key hole. This axis broadens to a 3-mm diameter and a height of 1.9 mm in which a 1-mm hole perpendicular to the axis was made to attach the needle rod. The holders are manufactured out of aluminium by the DEMO with wire EDM, to be light weight and have a mass of 0.14 g.

Key (Figure 11a (13)). Six aluminium keys of 5.8x2x2 mm^3 that fit the dimensions as the key hole of the six fixed ball spline follower cylinders, were produced by the DEMO using wire electrical discharge machining (EDM). Each key has two holes of 1-mm diameter to fix the follower axis and rod holder and has a mass of 0.11 g.

Needle rods (Figure 11a (18)). Six needle rods are connected to the rod holders via a hole and a fitting screw. The needle rods were made of spring steel and have a 0.3-mm diameter. The rods were cut to a length of 230 mm and sharpened at an angle of 20° at the tip using wire EDM by the DEMO, to decrease the cutting force in the tissue. The rods were converted at the distal tips via brass tubes (Figure 11a (14)) and held together by a shrinking tube (Figure 15).

4.1.3. Support

Support blocks (Figure 11a (2)). Two aluminium support blocks were made with wire EDM by the DEMO to support and align the ball spline axes and brass tubes. A hole was made in the centre of the blocks to press the 8-mm ball bearings in. Six holes in the shape of the fixed ball spline axes were made in a circle with a radius of 17.8 mm to the centre hole. These holes constrain the rotation of the axes, which are fixed in the holes with a fitting screw. Six holes with a 0.6-mm diameter and 11.05-mm radius to the centre hole were made to hold the brass tubes. After all the holes were made, the support block was cut in half along its length to create two perfectly aligned blocks. Two holes for fitting pens and one threaded hole were made at the bottom of each support block to connect the support blocks to the base plate.

Origami structure (Figure 11a (14)). A Miura-tube template [40] was adjusted so that the tube has a stretched length of 100 mm and height of 25 mm to fit in between the linear guides (Figure 16). The template is printed onto a transparent drawing paper sheet (O.Harris No.560.), cut-out, folded into the desired shape and glued together with a glue stick (HEMA) to form a tube. Holes for the needle rods were made by folding

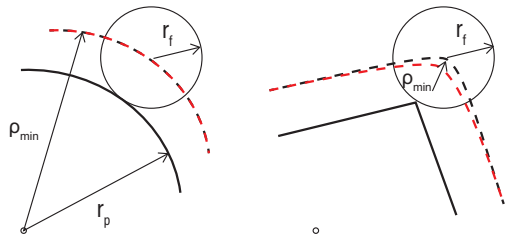

(a) (b)

Figure 14: Parameters to prevent undercutting of the cam path. r_f is the cam radius, r_p is the path radius and ρ_{min} is the minimum radius of curvature of the desired follower path. The cam path is indicated in black, the desired follower path in striped black and the real follower path in striped red. (a) Ideal situation, where $r_{c=\rho_{min}-r_f}$. (b) Undercutting, the follower cannot follow the desired path anymore.

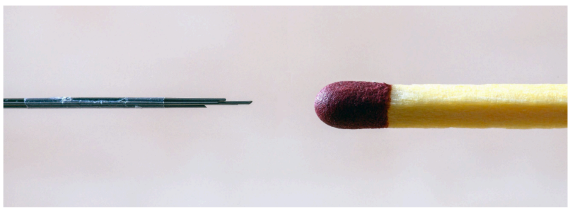

Figure 15: Close-up of the sharpened needle rod tips held together by the shrinking tube [39].

the Muira-tube to a hexagon (maximal contraction) and puncturing a 1-mm diameter pushpin into each side of the hexagon at a distance of 11.05 mm from the centre. A centre hole of 5-mm diameter was perforated, to attach the Muira-tube to the ball spline axis. The edges of all the holes were smoothed by placing the same pushpin in each individual hole and twisting it around.

Brass tubes (Figure 11a (15)). Six brass tubes were clamped into the support block holes and curved in an S-shape towards each other. The tubes support the needle rods and lead them towards each other. Brass is chosen because of its low friction coefficient with steel of μ =.0.51 The tubes have an inner diameter of 0.4 mm and an outer diameter of 0.6 mm, they were shortened to a length of 111 mm by the DEMO, using wire EDM.

Tube support middle (Figure 11a (16)). A support in the middle of the brass tubes was made to guide the brass tubes into the desired S-shaped curve. It has six holes with a diameter of 1.45 mm and radius of 6.30 mm to the centre. The support is made of a 4-mm thick aluminium plate and laser cut by the DEMO. Three holes are drilled at the bottom, two holes to align the support with pens to the base plate and one threaded hole to screw the support to the base plate.

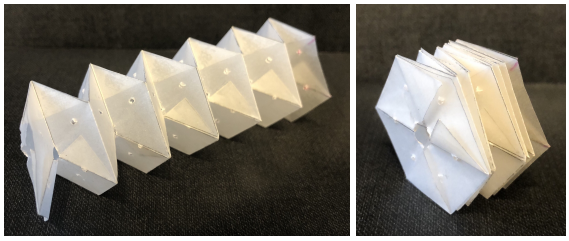

(a) (b)

Figure 16: Miura-tube needle rod support. (a) Extracted state. (b) Contracted state.

Tube support end (Figure 11a (17)). A support at the end of the brass tubes was made to bring the brass tubes together. It has a hole of 1.8 mm at its centre, where all the six brass tubes go through to form a flower-shaped profile. The part is made of a 4-mm thick aluminium plate and laser cut by the DEMO. Three holes are drilled at the bottom, two holes to align the support with pens to the base plate and one threaded hole to screw the support to the base plate.

Shrinking tube (Figure 15). A shrinking tube is attached to the needle rods distal tips to prevent the needle rods from diverging, however, the shrinking tube increases the total diameter of the needle bundle with 0.096 mm. We used the Clear Medical Heat Shrink Tubing 103-0352 (Nordson medical) with an inside diameter of 0.97 mm and a wall thickness of 0.013 mm. The shrinking tube was glued (Pattex instant glue, Gold original) to one of the needle rods by making two cuts in the shrinking tube and weave the needle rod between the cuts. The other five needle rods were shoved into the shrinking tube, allowing them to translate freely with respect to each other.

Base plate (Figure 11a (5)). The support blocks, tube support middle and end are attached to the base plate with two pens and a screw. The base plate is made of aluminium and laser cut by the DEMO.

4.1.4. Protection

Polymethyl Methacrylate (PMMA) shield. To protect the critical parts from dust, a PMMA box was laser-cut in the shape of the support blocks and glued together with two component glue.

4.1.5. Assembly

The prototype was assembled conducting the following steps:

1. The cam was pressed over the follower cylinder of one of the ball splines, align-

ing the key of the follower cylinder with the sloth in the cam.
2. A 1-mm cylindrical pen was placed in each follower, using precision tweezers.
3. The cylindrical pen and attached follower were placed in the proximal keyhole.
4. In the distal keyhole the rod holder was placed. This was done for all six keys, followers, cylindrical pens and rod holders.
5. The six keys with the attached followers and rod holders were placed into the keyholes of the six remaining follower cylinders by hand.
6. The ball bearings were pressed into the support blocks.
7. One of the support blocks was placed on its side on a table to place all the seven ball spline axes upright in each determined hole.
8. The follower cylinder with the fixed cam was shoved over the centre ball spline axis.
9. The six follower cylinders with the attached keys were shoved over the remaining axes one by one. Each time the centre axis and surrounding axis were pulled a bit from each other to let the follower fall into the V-shaped cam path.
10. After all seven follower cylinders were placed onto the ball spline axes, the second support block was placed on top of the axes, with each axis into its determined hole.
11. The two support blocks with the ball splines in between were placed on the base plate on the determined pens.
12. The middle and end rod supports were placed on the base plate on the determined pens.
13. The six brass tubes were shoved into the centre hole of the tube support end at the same time and were guided from the end support through the middle support to be fixed to the distal support block.
14. The origami structure was placed in between the ball splines.
15. Each individual needle rod was guided through the brass tubes starting from the opening at the distal end through each determined hole in the origami structure, while the distal ends of the needle rods were still connected by the shrinking tube.
16. Each proximal end of the needle rods was put into the designated hole of the rod holders with precision tweezers.
17. A fitting screw was screwed in the hole of the needle rod holder perpendicular to the needle rod hole, to fix the needle rods.
18. The actuation knob was pressed onto the proximal end of the centre axis.

4.2. Preliminary testing

The parts described above assemble our prototype, the WASP (Figure 17), which was examined on its desired functionality. A preliminary test in open air showed a correct working of the actuation mechanism. The needle rods moved in the correct sequence order and the ball spline and cam rotated smoothly. When the drive cylinder of the ball spline is rotated counterclockwise the follower cylinder and cam travel in the positive y-direction. When we turned the drive cylinder clockwise the system travelled in the negative y-direction. A possible explanation for this observation is that the friction forces in the ball splines exert a push force on the parts that can move in the y-direction. If the system was frictionless the needle bundle and cam would stay in place.

A second test demonstrated the desired functionality of the WASP in a gelatin sample and determined the required needle insertion depth before actuation. The self-propelling principle relies on the friction forces between the needle rods and the gelatin. Consequently, puncturing of the needle is not possible, as it involves only cutting forces and not the essential friction forces. Therefore, the needle rods must be initially inserted into the tissue to ensure sufficient surface contact between the needle and the gelatin to generate the friction forces. The test showed a correct working of the principle when the needle bundle was inserted 40 mm into the tissue before actuation. Additionally, we measured the performance of the needle in different concentrations of gelatin by calculating the slip ratio (s_r) with the following equation:

$$s_\mathrm{r} = 1 - \frac{d_\mathrm{m}}{d_\mathrm{t}} \tag{4.1}$$

Where d_t is the theoretical distance the needle would travel if no slip occurs and d_m is the measured distance the needle has travelled. A slip ratio of 1 indicates that the needle moves in its place and does not travel with respect to the tissue. Therefore, the optimal slip ratio would be zero, which indicates that the needle travelled the maximum possible distance through the tissue.

We executed the test in two situations, one without the origami structure integrated into the

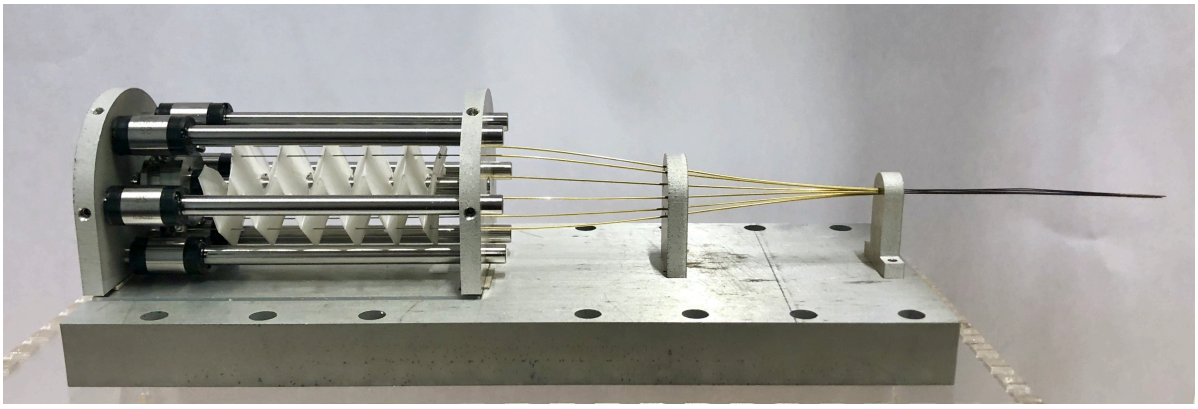

Figure 17: Photo of the WASP.

Table 4.1: Part list of the prototype of which the following information is presented: the part number corresponding to Figure11a, part name, manufacturing method, brand, dimensions, materials, amount of similar parts and the function.

#	Part name	Manufacturing	Brand	Size [mm]	Material	Amount	Function
1	Turning knob	SLA 3D printing	-	20x80	UV Resin	1	Actuate inner axis
2	Support block	Wire EDM	-	4x45x42.91	Aluminium	2	Support axes and tubes
3	Ball bearing	Off-the-shelf	NMB	2.5x8	Stainless steel	2	Allow free rotation of the centre axis
4/8	Ball spline axis	Off-the-shelf	IKO	5x100	Stainless steel	7	Centre drive, linear guide
5	Base plate	Lasercut	-	205x50x20	Aluminium	1	Attach all support
6/9	Ball spline follower cylinder	Off-the-shelf	IKO	10	Stainless steel	7	Transfer torque, linear guide
7	Cam	Milling	-	10x20	Aluminium	1	Advancing and retracting of the rods
10	Follower	Off-the-shelf	NMB	1x3	Stainless steel	6	Follow the cam path
11	Cylinder pen	Off-the-shelf	Jeveka	1x5	Stainless steel	6	Connect follower to key
12	Rod holder	Wire EDM	-	3x4	Aluminium	6	Connect rods to key
13	Key	Wire EDM	IKO	2x2x6	Stainless steel	6	Attach follower and rod holder to follower cylinder
14	Origami structure	Folding	-	25x80	Paper	1	Support rods
15	Tube	Wire EDM	-	0.6x100	Brass	6	Support rods and guide curve
16	Tube support middle	Lasercutting	-	4x20x30.22	Aluminium	1	Guide tube curve
17	Tube support end	Lasercutting	-	4x25.22x20	Aluminium	1	Guide tubes together
18	Needle rod	Wire EDM	-	0.3x230	Spring steel	6	Cut tissue

WASP and a second with the origami structure integrated into the WASP, to evaluate whether or not the origami structure is needed. The WASP performed 15 cycles, with a constant insertion velocity of 2 mm/s in gelatin samples of 5, 10 and 15 weight percentage (wt%). The position of the furthest needle rod was measured before and after actuation and from this the travelled distance was measured. Each test was conducted three times, the measurements without the origami structure were conducted on a different day than the measurements with the origami structure. The results are shown in Table 4.2. Figure 18 illustrates that the slip ratio increases when the gelatin concentration is increased. The slip ratio is lower when the origami structure is integrated in the WASP. The largest difference in slip ratio can be seen in a concentration of 15 wt%, where the mean slip ratio of the WASP without support is 0.76 and the mean slip ratio of the WASP with support is 0.09. This large difference could be explained by the observed buckling of the unsupported advancing needle rod.

5. Evaluation

5.1. Experiment 1: force measurement

5.1.1. Goal

We conducted two experiments to determine the performance of the design and compare our needle design to previous prototypes [21, 24]. In the first experiment (i.e., force measurement) multiple force measurements on the WASP were conducted. In the second experiment (i.e., velocity evaluation) the effect of the insertion velocity on the performance during needle insertion in gelatin was measured.

The force measurements were executed in four different set-ups. In set-up 1A, the insertion force (F_i) of pushing the needle bundle (i.e., the six needle rods connected by the shrinking tube) into different concentrations of gelatin was measured. In set-up 1B, we measured the force needed to advance all moving parts of the WASP in the positive y-direction (F_{proto}). Set-up 1C measured the force needed to move a gelatin block on a low-friction cart (F_{cart}). In the last set-up

Table 4.2: Test results of the preliminary experiment to determine the need of the origami structure. The insertion velocity was 2 mm/s, the number of actuation rotations was 15 and $d_{t=60}$ mm. For each measurement the following information is reported: the measurement number (#), the integration of the origami structure, the gelatin concentration (wt%), the mass of the gelatin sample and the mean and standard deviation (SD) of the slip ratio (s_r).

#	Origami structure	Gelatin concentration (wt%)	Mass gelatin sample (g)	s_r (-) Mean	SD
NS.5	no	5	94.0	0.12	0.010
NS.10	no	10	72.2	0.22	0.042
NS.15	no	15	105.1	0.76	0.025
S.5	yes	5	92.2	0.02	0.017
S.10	yes	10	71.6	0.03	0.010
S.15	yes	15	101.1	0.09	0.035

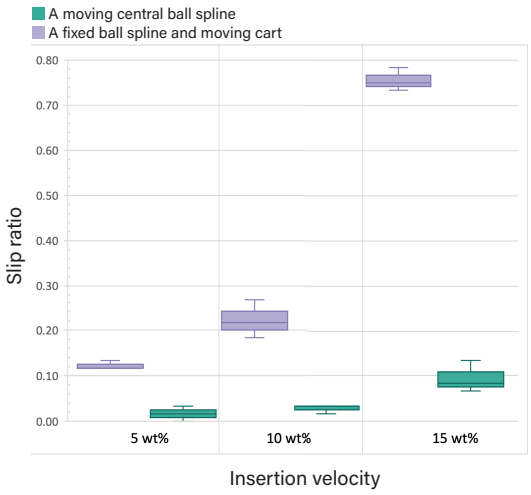

Figure 18: Slip ratio of the WASP in different concentrations of gelatin. In purple (left) the results of the WASP without the origami structure included and in green (right) the results of the WASP with the origami structure included.

1D, the net push force (F_{push}) generated by the friction forces and inertia of the WASP was measured. The goal of the experiments is to determine if the magnitude of the net push force exerted by the WASP is close to zero and compare this force to the push force needed for needle insertion by hand. To determine which elements of the WASP are contributing to this net push force, the magnitude of the friction and inertia forces of the WASP were measured. These forces were also compared to the friction and inertia forces of a gelatin sample on the low-friction cart to determine to which extend the mechanism permits a self-propelling motion through the gelatin.

5.1.2. Variables

Set-up 1A. The independent variable was the concentration of the gelatin samples of 5, 10 and 15 wt%. The dependent value was the measured peak force from pushing the needle bundle into the gelatin (F_i). The control variables were the room temperature of 22.1° C, humidity of 51.3 %RH and and the distance that the force gauge was pushed in the negative y-direction.

Set-up 1B. The independent variable was the implementation of the origami structure. The dependent value was the measured peak force from pulling the parts of the WASP that are allowed to translate in the y-direction (F_{proto}). The control variables were the room temperature of 20.2° C, humidity of 44.6 %RH and the distance that the force gauge was pulled in the positive y-direction.

Set-up 1C. Experiment 1C is a descriptive measurement that does not have an independent variable. The measured variable was the measured peak force from pulling the gelatin sample on a low-friction cart (F_{cart}). The control variables were the room temperature of 20.5° C, the humidity of 55.6 %RH and the distance that the force gauge was pulled in the positive y-direction.

Set-up 1D. The independent variable was implementation of the origami structure. The dependent value is the measured peak force from pulling the gelatin sample on a low-friction cart (F_{push}). The control variables were the room temperature of 20.2° C, humidity of 57.6 %RH and the number of rotations when actuating the WASP.

5.1.3. Set-up

A day before the experiment three gelatin samples were made by dissolving gelatin powder (Dr. Oetker) into boiling tap water (Rotterdam, the Netherlands). The 5 wt% solution was made with 10 g gelatin powder and 190 ml tap water, the 10 wt% solution with 20 g gelatin powder and 180 ml tap water and the 15 wt% solution with 30 g gelatin powder and 170 ml tap water. After stirring, the fully dissolved solutions were poured into moulds of 110x50x20 mm^3 and placed into a fridge to solidify overnight. The solidified gelatin blocks were cut into samples of roughly 100x40x20 mm^3. All set-ups

were executed on an aluminium breadboard of 600x150x12.7 mm^3 (Thorlabs, MB1560/M) that was levelled horizontally with a plumb rule, so that gravity does not influence the experiment. A phone camera (iPhone 8) held by a mini tripod (Benro, BK15) was placed right above the gelatin sample to capture the movements of the WASP and the measured forces. The experiment room temperature and humidity were measured with the Thermo-Hygrometer 625 (BK Precision). The gelatin samples were weighted on a school balance (KERN, EMB 200-1SS05). A schematic illustration of the four set-ups is shown in Figure 19, corresponding photos can be found in Appendix E.

Set-up 1A. A laser cut box (i.e., the gelatin holder) of 40x100x30 mm^3 was fixed to the breadboard with four bolts. The proximal end of the needle bundle was clamped with a bolt and screw between two washers to a slider (Festo) that could slide in an aluminium beam (Festo) with a length of 282 mm and a height and width of 30 mm. A push and pull Mechanical Force Gauge (Chatillon, LG Series) was fixed with tie-wraps to two cross-shaped sliders (Festo) that could slide into an aluminium beam (Festo) with a length of 180 mm and height and width of 30 mm (Festo). The aluminium beam with the needle bundle acting as a slider lays on the breadboard. A PMMA plate of 1-mm thickness was placed under the gelatin holder to horizontally level the gelatin sample and the needle bundle. The force gauge acting as a slider on the aluminium beam was placed in front of the breadboard in order for the push sensor to push the needle bundle from the proximal end (Figure 19a).

Set-up 1B. A deformed paper clip at the distal end of the needle bundle was hooked into the hook at the pull sensor of the force gauge. The WASP laid on the breadboard and the force gauge tie-wrapped to the slider and beam were placed in front of the breadboard (Figure 19b).

Set-up 1C. A gelatin sample of 40x100x20 mm^3 and a weight of 94.0 g was placed on a low-friction aluminium cart of 220x91x20 mm^3. The cart was placed on two PMMA plates of 250x100x5 mm^3 that laid on the breadboard. The force gauge, acting as a slider on the aluminium beam, was placed in front of the breadboard and the hook at the pull sensor of the force gauge was fixed to a hole at the front of the cart (Figure 19c).

Set-up 1D. The WASP and the force gauge laid on the breadboard facing each other. The force gauge was taped onto PMMA plates to level the height of the WASP. The tips of the needle bundle touched the force gauge's pressure sensor (Figure 19d).

5.1.4. Procedure

Procedure 1A.

1. A gelatin sample was weighted.
2. The gelatin sample was placed in the gelatin holder.
3. The needle bundle was inserted 20 mm into the gelatin by hand.
4. The force gauge was placed behind the needle bundle such that the push sensor of the force gauge touches the slider to which the proximal end of the needle bundle was attached.
5. The peak force button of the force gauge was pushed to reset the meter to zero.
6. The force gauge display was calibrated by turning the pointer to zero.
7. The force gauge was pushed for 80 mm by hand over the slider beam.
8. The peak force was read from the display of the force gauge and noted.
9. The needle bundle was removed out of the gelatin by hand.

The procedure was executed three times on a different insertion location in the same gelatin sample. Between each measurement the needle bundle was cleaned from remaining gelatin with tap water and paper towels. All measurements were executed on the same day.

Procedure 1B.

1. The gauge meter was pulled until the paper clip hook and needle bundle were under tension.
2. The peak force button of the force gauge was pushed to set the meter at zero.
3. The force gauge display was calibrated by turning the pointer to zero.
4. The force gauge was pulled for 80 mm by hand over the slider beam.
5. The peak force was read from the display of the force gauge and noted.
6. The ball splines were pulled back to their initial position by hand.

The procedure was executed five times in two different configurations of the WASP. One with the origami structure included and one without the origami structure. The measurements were executed on two different days.

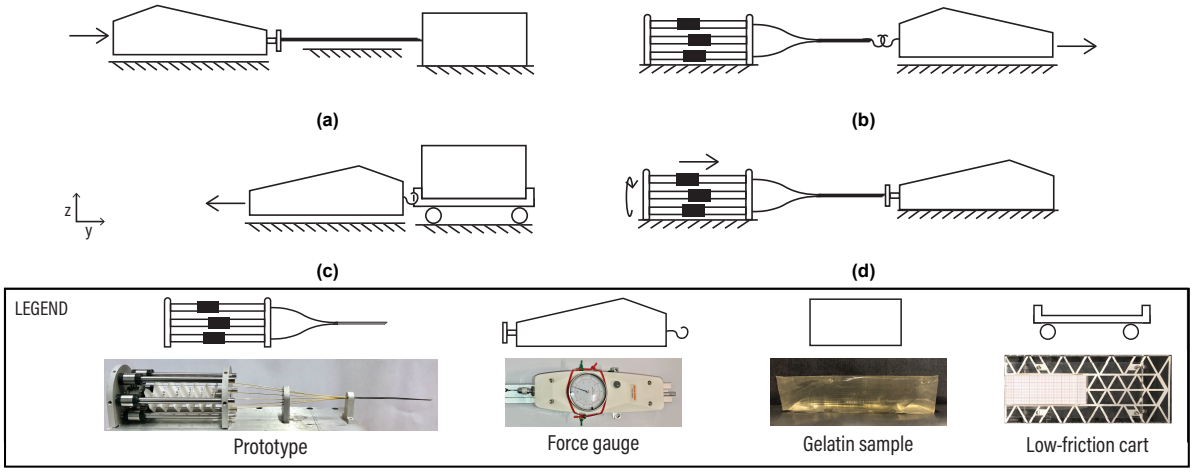

Figure 19: Schematic illustrations of the set-ups of Experiment 1. (a) Set-up 1A: A force gauge is placed on a linear guide and pushed against the needle bundle to measure the push force needed to insert the needle bundle into gelatin (F_{i}). (b) Set-up 1B: The force gauge is attached to the needle bundle with a hook and pulled backwards to measure the pull force needed to move the parts of the WASP that translate in the y-direction (F_{proto}). (c) Set-up 1C: The force gauge is attached to a gelatin sample on a low-friction cart and pulled backwards to measure the pull force needed to move the gelatin sample on the cart (F_{cart}). (d) Set-up 1D: Both the force gauge and WASP are fixed. The WASP is actuated and the net push force exerted on the needle bundle by the WASP is measured (F_{push}).

Procedure 1C.

1. The gauge meter was pulled until the paper clip pull sensor hook was under tension.
2. The peak force button of the force gauge was pushed to reset the meter to zero.
3. The force gauge display was calibrated by turning the pointer to zero.
4. The force gauge was pulled for 80 mm by hand over the slider beam.
5. The peak force was read from the display of the force gauge and noted.
6. The low-friction cart was moved back to initial position by hand.

The procedure was executed three times and all measurements were conducted on the same day.

Procedure 1D.

1. The force gauge was placed in front of the needle bundle such that distal end of the needle bundle touched the push sensor of the force gauge.
2. The peak force button of the force gauge was pushed to reset the meter to zero.
3. The force gauge display was calibrated by turning the pointer to zero.
4. The WASP was actuated by rotating the actuation handle 15 times counter clockwise.
5. The peak force was read from the display of the force gauge and noted.

The procedure was executed five times in two different configurations of the WASP. One with the origami structure included and one without the origami structure. The measurements were executed on two different days.

5.1.5. Test results

Result 1A. Table 5.1 shows the insertion force of the needle bundle insertion in gelatin by hand. It can been seen from the table that the stiffer the gelatin sample, the higher the insertion force. The insertion force of pushing the needle bundle into 15 wt% of gelatin was not measurable due to buckling of the needle bundle.

Result 1B. Table 5.2 shows the force to pull the parts that can move in the y-direction when pulling the WASP from the distal tips of the needle bundle. The mean pulling force of the WASP without the origami structure is 0.44 N and with the origami structure is 1.27 N.

Result 1C. Table 5.3 shows the force needed to pull a gelatin sample that lays on the low-friction cart, the mean force is 0.13 N.

Result 1D. Table 5.4 shows the push force generated by the WASP. The mean push force of the WASP without the origami structure is 0.16 N and with the origami structure is 0.18 N.

5.2. Experiment 2: speed evaluation

5.2.1. Goal

Experiment 2 analyses the WASP travelling through gelatin mimicking human tissue. To de-

Table 5.1: Test results of Experiment 1A. The following information is reported: the measurement number (#), the gelatin concentration (wt%) and the mean and standard deviation (SD) of the insertion force of the needle F_{i}.

#	wt%	F_{i}(N) Mean	SD
A.5	5	0.15	0.10
A.10	10	0.80	0.18
A.15	15	-	-

Table 5.2: Test results of Experiment 1B. The following information is reported: measurement number (#), integration of the origami structure, the mean and standard deviation (SD) of the pull force of the moving parts of the WASP (F_{proto}).

#	Support	F_{proto}(N) Mean	SD
B.NS	no	0.44	0.12
B.S	yes	1.27	0.19

Table 5.3: Test results of Experiment 1C. The following information is reported: the measurement number (#), the mass of the gelatin sample and the mean and standard deviation (SD) of force required for moving a gelatin sample on the low-friction cart in the y-direction (F_{cart}).

#	Mass (g)	F_{cart}(N) Mean	SD
C	94.0	0.15	0.10

Table 5.4: Test results of Experiment 1D. The following information is reported: the measurement number (#), the integration of the origami structure and the mean and standard deviation (SD) of measured net push force exerted by the WASP (F_{push}).

#	Support	F_{push}(N) Mean	SD
D.NS	no	0.16	0.17
D.S	yes	0.18	0.14

termine the influence of the inertia forces on the system, the experiment is executed under different insertion velocities. Inertia is proportional to the mass of a system moving with a constant velocity, doubling the velocity will double the momentum of the moving parts. We conducted the experiment with the origami structure integrated into the prototype, since a better performance was shown in the preliminary experiment (Section 4.2). Two set-ups were conducted, in set-up 2A, the actuation system moved as intended and the gelatin sample was fixed. In set-up 2B, the actuation system was fixed and the gelatin sample was placed on the low-friction cart to analyse whether the WASP is self-propelling.

5.2.2. Variables

The dependent variable in the experiment was the measured travelled distance of the needle bundle, d_{m}. The independent variable was the insertion velocity of the needle of 2, 4 and 6 mm/s, corresponding to an actuation tempo of respectively 30, 60 and 90 beats per minute (bpm). The control variables were, the room temperature of 20.5° C, the humidity of 48.7%RH and the gelatin concentration of 15 wt% . During perineal insertion the needle travels through muscle and tendon tissue to the prostate (Figure 1). Muscle tissue has a Young's modulus of 12-32 kPa, tendons a Young's modulus of 69-134 kPa, and prostate gland with lesions has a Young's modulus between 20-98 kPa (benign) and 26-175 kPa (malignant) [41, 42]. Hence, it is desired that the needle can operate in tissue with a Young's modulus between 12 and 175 kPa. The preliminary test in different concentrations of gelatin (Section 4.2) showed that the needle can operate in a concentration of 5, 10 and 15 wt%, corresponding to a Young's modulus of 5.3, 17 and 31 kPa respectively [20], while needle insertion by hand was only possible in concentration of 5 and 10 wt%. Hence, we chose to conduct the experiment in gelatin of 15 wt% to show the performance of the WASP in stiff tissue.

The theoretical travelled distance (d_{t}), as if there is no slip, is calculated by:

$$d_{\mathrm{t}} = S \cdot \#_{\mathrm{cycles}} \tag{5.1}$$

In each measurement, the needle underwent 15 cycles with S = 4 mm, resulting in $d_{\mathrm{t}} = 60$ mm. As a performance metric the ratio between the measured distance (d_{m}) and the theoretical distance (d_{t}) was calculated as the slip ratio (s_{r}) (Equation 4.1).

5.2.3. Set-up

A day before the experiment, the gelatin samples were made as described in Section 5.1.3. The experiment room temperature and humidity were measured with the Thermo-Hygrometer 625 (BK Precision). Both set-ups were executed on the breadboard and a phone camera (iPhone 8) held by a mini tripod (Benro, BK15) was placed right above the gelatin sample to capture the displacement of the needle inside of the gelatin. The table and breadboard were levelled horizontally with a plumb rule, so that gravity could not influence the experiment. Metric paper was placed below the gelatin sample to determine the travelled distance of the needle bundle. A digital metronome was used to determine the actuation tempo.

Set-up 2A: The WASP was placed onto the

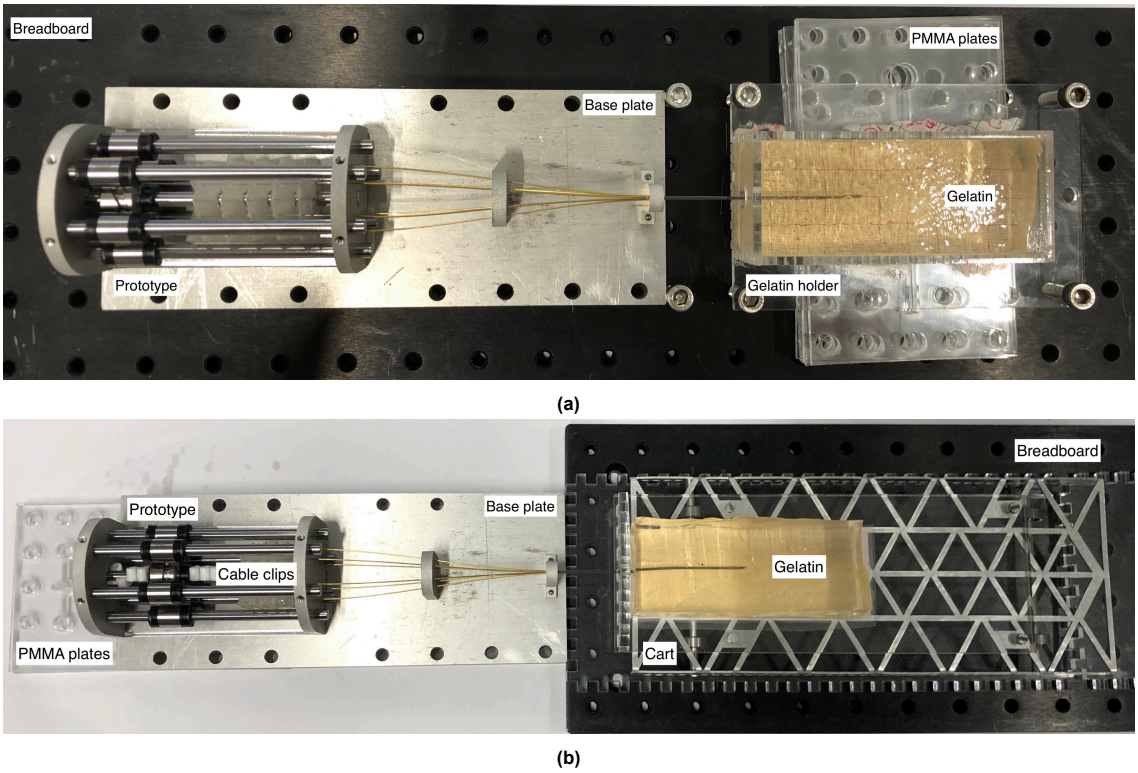

Figure 20: Set-ups of Experiment 2. (a) Set-up 2A: Fixed base plate and fixed gelatin sample, moving ball spline. Set-up 2B: Fixed base plate and fixed ball spline, moving gelatin sample on the low-friction cart.

breadboard and secured by two bolts in front of the base plate. The gelatin holder was fixed to the breadboard with four bolts, placed under four PMMA plates of 1-mm thickness to level with the WASP. A gelatin sample was placed into the gelatin holder and the distal ends of the needle bundle were directed at the gelatin sample (Figure 20a).

Set-up 2B: The centre ball spline of the WASP was fixed with cable clips of 4-mm diameter (Praxis) to constrain the translation in the y-direction, while allowing the rotation along its axis. A gelatin sample was placed on the low-friction aluminium cart of 220x91x20 mm^3 that was placed on two PMMA plates of 250x100x5 mm^3 aligned along their length. The WASP was placed in front of the breadboard to level the needle bundle with the gelatin sample (Figure 20b).

5.2.4. Procedure

The procedure for both set-up A and set-up B was the same. During each measurement, the needle was actuated for 15 cycles, where each cycle is equal to one revolution of the cam, thus the actuation handle was turned 15 times. The needle was inserted with a velocity of 2, 4 or 6 mm/s. For each velocity the needle was inserted three times in a new gelatin sample of ca. 40x100x20 mm^3 and a mass between 99 and 101 g. After 15 cycles the position of the furthest needle rod was measured and noted. These were subtracted from the initial rod position of 40 mm to calculated the travelled distance d_{m}. The following steps were executed each measurement:

1. A gelatin sample was weighted.
2. The gelatin sample was placed into the gelatin holder or on the low-friction cart.
3. The needle bundle was inserted into the gelatin by hand until the furthest needle rod was 40 mm deep.
4. The needle bundle and low-friction cart were aligned.
5. The metronome was turned on in a tempo of 30, 60 or 90 bpm.
6. The actuation handle was rotated 15 times counter clockwise in the tempo of the metronome.
7. The metronome was turned off.
8. The end position of the furthest needle rod was determined from the metric paper and noted.
9. The needle was removed by sliding the follower cylinder of the middle ball spline backwards or turning the rotary knob clockwise.

Table 5.5: Test results of Experiment 2. The following information reported: the measurement number (#), the set-up, the insertion velocity, the mean and standard deviation (SD) of the gelatin sample mass and the mean and SD of the slip ratio (s_r).

#	Set-up	Velocity (mm/s)	Mass gelatin sample (g) Mean	SD	s_r (-) Mean	SD
2A.2	A	2	99.6	0.55	0.22	0.069
2A.4	A	4	99.5	0.70	0.17	0.088
2A.6	A	6	99.6	0.64	0.15	0.076
2B.2	B	2	99.8	0.92	0.45	0.076
2B.4	B	4	100.0	0.31	0.57	0.093
2B.6	B	6	99.7	0.95	0.59	0.025

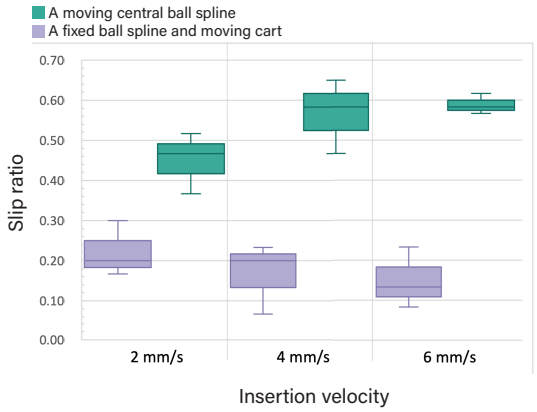

Figure 21: Slip ratio of the WASP entering gelatin with different insertion velocities. In purple (left) set-up 2A: a moving centre ball spline of the WASP and in green (right) a fixed centre ball spline and moving gelatin on a low-friction cart.

Firstly, these steps were executed for experiment set-up 2A and secondly for experiment set-up 2B. All the measurements were executed on the same day.

5.2.5. Test results

Figure 21 shows that the slip ratio for set-up 2A (i.e., where the centre ball spline is free to translate in the y-direction) lays higher than for set-up 2B (i.e., where the centre ball spline is fixed and the gelatin moves on a low-friction cart) under all conditions. Interestingly, increasing the insertion velocity led to an increase of the slip ratio for set-up A, while it led to a reduction of the slip ratio for set-up B.

6. Discussion

6.1. Main findings

In this study, we presented the design of the WASP, a manually actuated low-friction needle that uses the self-propelling principle of the parasitoid wasp to travel through tissue. Our goal was to come closer to clinical practice compared to previous design, where the needle and actuation system were stationary while the tissue on a low-friction cart was pulled over the needle [21]. The aim of the WASP is that the patient lays stationary and that only the necessary parts of the needle device move in positive y-direction to travel through the tissue. This required a mechanism that could transfer a torque while allowing a translation with minimal friction.

Evaluation of the WASP showed the promising result that needle insertion in 15 wt% gelatin is possible for the WASP, while it was not possible for manually insertion. This is likely due to needle buckling outside the gelatin during manually insertion (Figure 22), while the WASP could easily travel through the 15 wt% gelatin in a straight line (Figure 23). A possible explanation for this outcome may be the reduction of the net push force of the WASP compared to manual insertion. The net push force exerted by the WASP is 0.18 N (Table 5.4), while the manual insertion force is 0.8 N in 10 wt% gelatin (Table 5.1) and expected to be even higher in substrate with a higher stiffness. It seems likely that due to the reduction of the net push force, although not being zero, needle insertion in higher gelatin concentrations could be achieved.

The measured net push force might be generated by the friction forces generated in the WASP. The ball splines, that function as linear guides of the needle rods, have roll friction between the follower cylinder and corresponding axis cylinder. The cam pushes five followers and their corresponding follower cylinders in the negative y-direction (backward), while pushing one follower cylinder in the positive y-direction (forward). Consequently, the friction forces of the backward moving follower cylinders overcome the friction force of the forward moving follower cylinder, resulting in a net force in the positive y-direction. This explanation is supported by our observations during the preliminary tests that showed the cam moving forward with counterclockwise actuation and backwards with clockwise actuation, where the input motion of the cam and gener-

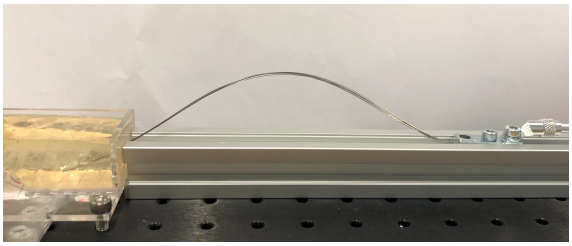

Figure 22: Observation during Experiment 1A: Insertion of the needle bundle by hand into a 15 wt% gelatin sample was unsuccessful, due to buckling of the needle bundle.

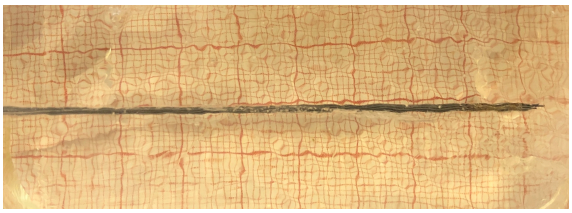

Figure 23: The needle bundle of the WASP travelling through 15 wt% gelatin in a straight line.

ated friction forces were reversed. This follows the same self-propelling principle as occurring between the needle rods and the gelatin. However, the problem is that the net force generated by the follower cylinders and their axes is located at the proximal end of the needle rods and thereby pushing the needle rods. Whereas, the net force generated by the friction force of the needle rods and the tissue is located at the distal tips of the needle bundle and thereby pulling the needle rod bundle. The mean force to pull the moving parts of the WASP is 1.27 N (Table 5.2), which is greater than the net push force of 0.18 N by a factor 10, suggesting that not all the measured forces are applied in the same direction.

The aim of a zero external push force as established by previous research on self-propelling needles, was to prevent buckling of a slender needle [25]. Buckling is the lateral deformation of a beam due to an axial load. It is desired to prevent buckling, because lateral deflection can cause damage to healthy tissue and can lead to inaccurate needle positioning [12, 43]. Furthermore, the structural stability decreases when in buckled state compared to unbuckled state, which decreases the maximum compressive load the needle can endure and can lead to failure of the needle [43]. However, a disadvantage of a zero net push force is that a smaller net push force results in a higher slip ratio. The slip ratio is the ratio between the measured distance travelled in the gelatin and the theoretically travelled distance. A slip ratio of 0 means that the theoretically travelled distance and measured distance are the same and thus that the needle travelled through the tissue with zero slip. A slip ratio of 1 indicates that there is 100% slip and thus that the measured distance after one cycle of the cam results in zero forward movement of the needle relative to the gelatin (i.e., the needle moves in its place). This can occur if the cam is pushed back and forth relatively to the gelatin on the same spot or if the needle buckles and deforms in its place.

Experiment 2 supports the idea that a smaller net push force results in a higher slip ratio. The net push force of the gelatin sample on the low-friction cart is expected to be lower than that of the WASP, considering the measured force of 0.15 N to move the gelatin on low-friction cart versus the 0.44 N to move the parts of the WASP that translate in the y-direction. The value of the measurement of the WASP without origami structure is used because the friction forces generated by the origami structure do not influence the net push force, as demonstrated by Experiment 1D. The mean slip ratios of the gelatin sample on the low-friction cart and a fixed inner ball spline of the WASP are 0.45, 0.57 and 0.59, for velocities of respectively 2, 4 and 6 mm/s. Whereas, the slip ratio of the WASP moving as intended is reduced to 0.22, 0.17 and 0.15 for velocities of respectively 2, 4 and 6 mm/s (Table 5.5). Figure 21 shows the significant difference between the slip ratio of the gelatin on the low-friction cart and the WASP moving as intended. However, a significant difference between the insertion velocities, indicating a significant contributing of the inertia was not found. Previous study of Scali *et al.* [20] also support this observation that a lower net push force results in a higher slip ratio. Their self-propelling needle prototype with six 0.25-diameter needle rods, has zero net push force and a slip ratio of 0.45-0.8 when being inserted with a velocity of 2 mm/s in 15 wt% gelatin. This is a factor of 2-4 higher than for the WASP.

The observations from Experiment 2 and the comparison with the prototype of Scali *et al.* [20] may suggest that a small net push force could be beneficial to reduce the slip ratio. In such scenario, the upper limit of the net push force should be identified. An approach of quantifying the upper limit could be the requirement of zero buckling of the needle rods, implying that the net push force should stay under the critical buckling load of the needle rods. The critical buckling load determines the point where a beam deforms to buckled state under a compressive load. It depends on the length, end state and material of the needle and is defined by the Euler's load equa-

tion:

$$P = \frac{\pi^2 EI}{(kL)^2} \tag{6.1}$$

Where E is the Young's Modulus of the needle, I the area moment of inertia of the needle, k is a coefficient corresponding to the end states of the needle and L the effective buckling length of the needle. For one needle rod of the WASP the critical buckling load is 0.09 N, which means that the push force exerted by the cam to advance one needle rod should be below 0.09 N. For the whole needle bundle the critical buckling load is 7.47 N, which is higher than the net push force of 0.18 N, hence it is likely that the WASP could be considered safe. The full calculation can be found in Appendix G.

The WASP has only been tested in homogeneous gelatin solutions and not yet in *ex vivo* or *in vivo* tissue with inhomogeneous properties. Bloemberg *et al.* [21] evaluated the performance of a manually actuated self-propelling needle in *ex vivo* prostate tissue and indicated a slip ratio of 0.86-0.96. The slip ratio of Bloemberg [39]'s needle is 0.44 in 10 wt% gelatin (only one measurement) and the slip ratio the WASP in 10 wt% gelatin is 0.03 (Table 4.2). Considering the lower slip ratio under approximately the same circumstances, we expect the slip ratio of the WASP in prostate tissue to be lower than the result of Bloemberg *et al.* [21]. This prediction is based on assumptions and its accuracy should be examined through future evaluation.

6.2. Limitations & Recommendations

6.2.1. Design

Firstly, the experimental design process was limited by a constrained time frame for the design choices and the necessity to choose a focus in the early design phase. We initially opted for a manual actuation system to narrow the scope of the research. A drawback of a manual actuation system may be a high mental load on the urologist [32]. Further studies could explore alternative human actuation methods, such as using a foot pedal similar to those in sewing machines. Another direction to explore is a motor-driven actuation system, where the urologist simply presses a button to initiate the needle motion. It is important to consider the additional weight and space a motor-driven mechanism may entail. Additionally, we made the choice in the early design stage for a human control system. Automation of the procedure has the potential to reduce the mental load of the urologist and minimise targeting errors. However, due to ethical considerations regarding the responsibility for errors during the procedure, the urologist must remain in the loop safeguarding the patient [44]. It is predicted that in the future this will be in the form of supervisory control [44]. Despite this expectation, humans have proven to be unsuitable for supervisory tasks, as the inactivity of the response part in the brain can result in response delays [45]. These response delays could be minimised by haptic feedback during cooperative control, were the robot and human work together [46]. An optimal task division could be developed where the human workload is relieved and human abilities are extended [45]. The needle devise could be integrated with the TRUS probe images and automatically navigate to the desired location. Several studies have explored the advantages of robotic assistance in brachytherapy and show its potential to improve needle placement accuracy [47, 48]. However, the cost-effectiveness of robot assisted procedures versus non-robotic procedures have not been proved yet [49].

Another limitation is that the requirements for the needle system (i.e., the needle rods and shrinking tube) were derived from previous research and have not been further iterated [20, 21, 25, 26]. Further investigation could be conducted on the design of the needle rods. In the current design, the needle rods were sharpened on one side, forming an asymmetrical tip that can lead to asymmetrical forces on the needle tip [50]. A symmetrical tip that is sharpened on both sides will equally divide the cutting forces. Additionally, a study could be conducted on increasing the friction force between the needle rods and the tissue, potentially by integrating barbs on the needle rods. A disadvantaged of adding barbs is that they also increase the resistance during needle retracting. A potential solution might draw inspiration from Khodaei *et al.* [51]'s smart barbs, which can adjust the barb angle to have barbs during insertion and no barbs during retraction of the needle. A last limitation is that the final concept selection has been made on the availability of parts. Concept 2 would be potentially more favourably, due to the integration of a support that guides the needle rods towards each other and prevents buckling of the needle rods in the centre of the prototype. However, this concept was not chosen due to the unavailability of an inverted ball spline. The concept would require a custom fabrication process, which was beyond our reach in terms of precision and availability. In future development of the prototype, an assessment may be conducted to determine whether custom fabrication and the associated costs would add value to the concept.

6.2.2. Prototype

The first limitation of the production of the prototype is the availability of parts. The dimensions of the prototype were determined by the available off-the shelf parts. Smaller parts than those implemented in the prototype were found, such as a ball spline with an axis diameter of 2 mm and follower cylinder of 6 mm diameter (IKO, LSAG2). However, we used parts that were available in the Netherlands, as the alternative options had production and delivery times of over six weeks. The distance travelled within the tissue is limited by the length of the ball spline axis of 100 mm. To overcome this limitation a custom made axis with a longer length, could be produced. To connect the needle rods we used an available shrinking tube with an inner diameter of 0.97 mm. The outer diameter of the needle bundle, of approximately 0.9 mm, is smaller than that of the shrinking tube, leaving a gap in between. It was observed that the gelatin tends to accumulate in this gap, causing the needle rods to stick together. Using a smaller shrinking tube or investigating alternative methods for connecting the needle rods could be considered as potential solutions.

The production of the origami structure was limited, as it was handcrafted using paper. Each fold has a slight off-set, resulting in an imperfectly fitted shape. Another limitation is that the holes were punctured instead of removed, resulting in a rough surface and increased friction with the needle rods. Although this friction affects only the actuation force and not the net push-force, reducing it will be beneficial to limit the actuation force and the energy input of the urologist. The origami structure shows opportunities for further research, a material study into 3D-printed thin foldable structures and a design iteration on the origami pattern, could be conducted.

The most important limitation of the prototype is that we were unsuccessful in creating a zero push force mechanism. It is likely that the net push force is due to the friction forces in the system, specifically in the ball splines. We chose to use six ball splines (IKO, LSAG5) as linear guides for the needle rods. In future investigations, it might be possible to directly slide the needle rods in a hollow axis as linear guide (Figure 24). Due to the low forces and mass, the difference between rolling and sliding may be minimal, while the difference in mass of a rolling or sliding linear guide has a greater influence. Furthermore, spring alternatives or compliant mechanisms could be explored, this has not been taken into account yet because it requires a comprehensive research and exploration.

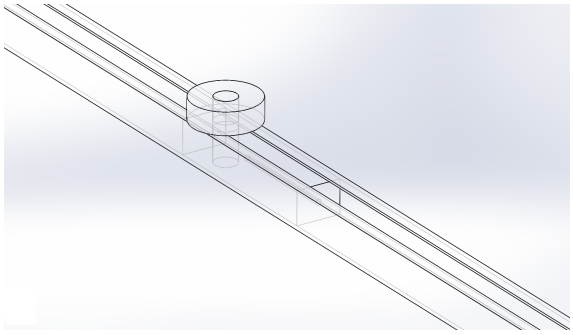

Figure 24: Artist impression of a hollow axis as linear guide for a future version of the WASP.

6.2.3. Experiments

One limitation of the experiments is that the gelatin samples were inconsistent. It was observed that the gelatin samples were stiffer at the bottom of the containers. This inconsistency may be due to the fact that gelatin powder is heavier than water and sinks to the bottom when curing in the fridge. Another inconsistency was found among the different containers the gelatin solution was poured into, two out of five container had a clearly lower stiffness and were therefore unusable for the experiments. Furthermore, during the experiments the gelatin samples were compressed into the gelatin holder, influencing both the fluid mechanics and the stiffness of the sample. These inconsistencies may have led to a true stiffness different from the estimated stiffness derived from previous research. In future experiments strength tests could be conducted on the gelatin to determine the true Young's modulus.

A second limitation is that the experiments and measurements were not conducted on the same day, which led to varying circumstances. The same needle rods were used for all measurements, leading to three observed inconsistencies during the experiments. The first limitation arises from the fact that after each insertion, the needle tips become blunter, due to the cutting forces exerted by the gelatin. The second limitation is that gelatin remains on the needle rods, making them stickier. Although efforts were made to clean the needle rods in between measurements, some residue remained especially between the shrinking tube. The last limitation observed is that the needle rods started diverging more at the distal tip after each insertion. The effect of these three limitations can be seen in the difference between the slip ratios of the preliminary test and Experiment 2 that were conducted two days apart from each other. The tests were performed under the same conditions (velocity and

insertion depth), but the slip ratios in the preliminary test were lower than in Experiment 2. In future experiments, the needle rods could be replaced with a new sharpened set about every ten measurements, because no irregularities were observed until that point. In medical practise new needle rods should be used every procedure, not only for maintaining sharpness, but also to ensure sterility.

Another limitation is that during the experiments the WASP was manually actuated. Although the tempo was determined by a metronome, the velocity cannot be considered constant throughout the measurement. An electromotor could be used in future experiments to actuate the WASP with a constant velocity. A disadvantage of using an electromotor is that the resistance of the gelatin varies, requiring an adaptive input torque to the motor to keep a constant velocity. The last limitation of the experiments is the utilised equipment, which all contain inaccuracies. The mechanical force gauge influenced the results the most, with its accuracy of 0.05 N and not being able to save the measured force over time, only the maximum force. In future experiments an electrical force gauge with higher precision could be used that can measure forces in the mN range and can record the force over the whole trajectory. This would enable observations of the consistency of the force over time and identification of location of the peak force.

6.3. Future work

6.3.1. Medical application

To be suitable for medical application, the WASP needs to fulfil the nice-to-have requirements as determined in Section 2.3. Firstly, the use of MRI-compatible materials was not taken into account in the WASP that was built to validate a new mechanism. Future iterations could focus on an MRI-compatible prototype for testing in an MRI scanner and for the use in subsequent TPLA procedures. Plastic and ceramic bearings were found as MRI-compatible substitutes, however, these bearings have the disadvantage of being larger in diameter. The smallest ceramic ball bearing found has an outer diameter of 5 mm (Ortech, MR52), while the followers used in the WASP have an outer diameter of 3 mm. Using 5-mm ball bearings as followers would result in an undesired larger cam path and a larger cam diameter to prevent undercutting of the cam path. A substitute for the ball spline in MRI-compatible materials has not been found yet and producing a custom made ball spline requires specialised expertise. Potential adjustments in the other parts of the WASP may include replacing the support parts with 3D-printed components and using Nitinol rods, which are also biocompatible with human tissue, instead of spring steel needle rods [52].

Additionally, a crucial aspect in clinical application is equipment sterility, as unsterilised needles can pose serious consequences [53]. In the current prototype, the needle rods are replaceable, however, this demands high concentration and is time-consuming. Future research could explore a clickable system allowing urologists to easily attach the needle rod bundle to the actuation mechanism before each procedure. Only the needle bundle should be single-use and the remaining system could be reusable for environmental reasons and cost efficiency. Future design decisions could prioritise durable materials and the individual parts of the WASP could be replaceable to avoid replacing the entire unit if one part breaks. The reusable parts should be sterilised and comply with the ISO 11737-2 standard [54]. Thorough testing will be needed for the medical application of the WASP. To ensure the applicability of the design for every human, experiments should be conducted in both *in vivo* and *ex vivo* prostate tissue. The collection of additional data from these experiments is essential to draw general conclusions about the design's performance. Ultimately, clinical trials will be needed to evaluate the design's safety and meeting the medical device regulations of the European Union (EU) [55]. If the needle is brought to clinical use, its pricing should be compatible with other needles on the market, such as the ProMag™ Ultra Automatic Biopsy Instrument that has a market price of €2500 [56].

6.3.2. Next steps

User research is an important next step in the development of wasp-inspired needles. Firstly, research into the direct user of the needle device, the urologist, is required. Research questions may include identifying the desired actuation input that is easy in use and feels intuitive. Additionally, investigation of the effective control of the WASP and determining the optimal dimensions alongside other instruments is necessary. The second user research could be focused at the indirect user, the patient. Since this needle is aiming to be used in a procedure where full anaesthesia is no longer needed, the perceived safety and pain of the patient play an important role. Fear of needles is common among patients and a threatening device could lead to reduced trust in the procedure, resulting in a less posi-

tive experience and potentially even avoidance of needle procedures [57–60]. It is important to integrate these human design factors into the design phase as soon as possible to prevent design locks, where the technical aspects are already too far developed and cannot be adapted to the user's needs anymore.

Alongside the user research, a technical next step in the continuation of the project is to implement steering into the design. The design presented in this paper focused on creating a working low-friction mechanism capable of travelling through stationary tissue. With the successful validation of the concept, different steering strategies could be addressed in further research. Several strategies for steering in solid organs during brachytherapy exist by creating a deflection angle [61]. This deflection angle can be created on demand through the use of a shape memory material that deflects through heating [62]. Alternatives are the use of a pre-curved needle guided by a cannula [63], incorporating a deflectable bevel tip [64] or by a discrete bevel tip [25]. Lastly, the inclusion of a laser fibre is essential to make the design suitable for TPLA procedures. Scali *et al.* [20] showed that one of the six needle rods could be replaced with an optical fibre. The friction coefficient of the laser fibre should align with that of the material used for the other needle rods. Another possibility is to implement the laser fibre in the centre of the six needle rods. If a laser fibre is implemented the materials used in the WASP should be resistant to the 1800 J that is released by the laser fibre [14]. Implementing user research, a steering mechanism, and the TPLA laser fibre can result in the creation of new prototypes, allowing for evaluation and iterations until a final WASP design is developed.

7. Conclusion

A manual actuation mechanism for an ovipositor-inspired needle was methodically designed and a prototype, the WASP, has been made to prove the concept. The project aimed to design an actuation mechanism for a self-propelling needle that can travel trough stationary tissue by manual actuation, with a focus on minimising the friction in the mechanism close to zero. The WASP could successfully travel in a straight line without buckling through gelatin concentrations up to 15 wt%. Due to the friction in the mechanism (F_{proto} = 1.27 N), the WASP generates a small external push force (F_{push} = 0.18 N) and cannot be considered fully self-propelling. However, the net push force is significantly reduced compared to needle insertion by hand (F_{i} = 0.8 N) and insertion by the WASP is possible without buckling. A performance experiment showed that the mean slip ratio in 15 wt% gelatin (s_{r} = 0.22, 0.17 and 0.15 for insertion velocities of respectively 2, 4 and 6 mm/s) is lower than found in previous research (s_{r} = 0.45-0.8 in 15% gelatin [20] and s_{r} = 0.86-0.96 in *ex vivo* human prostate [21]). These observations may suggest that a small net push force could be beneficial to reduce the slip ratio, if buckling is prevented. A challenge remains in reducing friction in the mechanism, which could be further explored by replacing the linear guides with alternative mechanisms like compliant systems or low mass sliders. Future steps involve integrating a steering element, a TPLA fiber and user-focused elements, leading to a new prototype that can undergo evaluation for medical regulations and potential implementation in health care. The presented design and prototype contribute to the research of wasp-inspired self-propelling needles by providing a low-friction needle that the urologist can move through stationary tissue during TPLA procedures, holding promise for future innovations in minimally invasive surgery for prostate cancer.

Acknowledgements

We would like to express our gratitude to several individuals who played crucial roles in this project. Remi van Starkenburg, from the DEMO, for his insights into the manufacturing process and producing the majority of parts of the prototype. Mario van der Ven, also from the DEMO, for addressing last-minute inquiries and adjustments, ensuring a working prototype. Katelijne de Bie for explaining the medical aspects of this project and allowing us to observe one of her procedures. Jan Frankenhuizen for its technical expertise and insights. The employees of the IWS and IWM for their quick tips and assistance in the production process and Jacques Brenkman from the Meetshop for the test set-up and materials.

References

1. Verze, P., Cai, T. & Lorenzetti, S. The role of the prostate in male fertility, health and disease. en. *Nature Reviews Urology* **13,** 379–386. ISSN: 1759-4812, 1759-4820. `https://www.nature.com/articles/nrurol.2016.89` (2023) (July 2016).
2. Sung, H. *et al.* Global Cancer Statistics 2020: GLOBOCAN Estimates of Incidence and Mortality Worldwide for 36 Cancers in 185 Countries. en. *CA: A Cancer Journal for Clinicians* **71,** 209–249. ISSN: 0007-9235,

1542-4863. https://onlinelibrary.wiley.com/doi/10.3322/caac.21660 (2023) (May 2021).

3. Schatten, H. en. in *Cell & Molecular Biology of Prostate Cancer* (ed Schatten, H.) Series Title: Advances in Experimental Medicine and Biology, 1–14 (Springer International Publishing, Cham, 2018). ISBN: 978-3-319-95692-3 978-3-319-95693-0. http://link.springer.com/10.1007/978-3-319-95693-0_1 (2023).
4. Ahdoot, M., Lebastchi, A. H., Turkbey, B., Wood, B. & Pinto, P. A. Contemporary treatments in prostate cancer focal therapy. en. *Current Opinion in Oncology* **31,** 200–206. ISSN: 1040-8746, 1531-703X. https://journals.lww.com/00001622-201905000-00014 (2023) (May 2019).
5. Van Riel, L. A. *et al.* Safety and Feasibility of Soractelite Transperineal Focal Laser Ablation for Prostate Cancer and Short-term Quality of Life Analysis from a Multicenter Pilot Study. en. *European Urology Open Science* **39,** 48–54. ISSN: 26661683. https://linkinghub.elsevier.com/retrieve/pii/S2666168322000593 (2023) (May 2022).
6. Van Kollenburg, R. A. A. *et al.* Transperineal Laser Ablation Treatment for Lower Urinary Tract Symptoms Due to Benign Prostatic Obstruction: Protocol for a Prospective In Vivo Pilot Study. en. *JMIR Research Protocols* **9,** e15687. ISSN: 1929-0748. https://www.researchprotocols.org/2020/1/e15687 (2023) (Jan. 2020).
7. Manenti, G. *et al.* 3-T MRI and clinical validation of ultrasound-guided transperineal laser ablation of benign prostatic hyperplasia. en. *European Radiology Experimental* **5,** 41. ISSN: 2509-9280. https://eurradiolexp.springeropen.com/articles/10.1186/s41747-021-00239-9 (2023) (Dec. 2021).
8. Pacella, C. M. *et al.* Transperineal laser ablation for percutaneous treatment of benign prostatic hyperplasia: a feasibility study. Results at 6 and 12 months from a retrospective multi-centric study. en. *Prostate Cancer and Prostatic Diseases* **23,** 356–363. ISSN: 1365-7852, 1476-5608. https://www.nature.com/articles/s41391-019-0196-4 (2023) (June 2020).
9. De Jong, T. L. Needle placement errors: do we need steerable needles in interventional radiology? en. *Medical Devices,* 7.
10. Taschereau, R., Pouliot, J., Roy, J. & Tremblay, D. Seed misplacement and stabilizing needles in transperineal permanent prostate implants. en. *Radiotherapy and Oncology* **55,** 59–63. ISSN: 01678140. https://linkinghub.elsevier.com/retrieve/pii/S0167814000001626 (2023) (Apr. 2000).
11. Roberson, P. L., Narayana, V., McShan, D. L., Winfield, R. J. & McLaughlin, P. W. Source placement error for permanent implant of the prostate. en. *Medical Physics* **24,** 251–257. ISSN: 0094-2405, 2473-4209. https://aapm.onlinelibrary.wiley.com/doi/10.1118/1.598058 (2023) (Feb. 1997).
12. Abolhassani, N., Patel, R. & Moallem, M. Needle insertion into soft tissue: A survey. en. *Medical Engineering & Physics* **29,** 413–431. ISSN: 13504533. https://linkinghub.elsevier.com/retrieve/pii/S1350453306001457 (2022) (May 2007).
13. Abolhassani, N., Patel, R. V. & Ayazi, F. Minimization of needle deflection in robot-assisted percutaneous therapy. en. *The International Journal of Medical Robotics and Computer Assisted Surgery* **3,** 140–148. ISSN: 14785951, 1478596X. https://onlinelibrary.wiley.com/doi/10.1002/rcs.136 (2023) (June 2007).
14. *EchoLaser®: First, Unique, Micro-invasive, Integrated System Offering Diagnostic Ultrasound and Laser Thermal Ablation Therapy*
15. Cerkvenik, U., van de Straat, B., Gussekloo, S. W. S. & van Leeuwen, J. L. Mechanisms of ovipositor insertion and steering of a parasitic wasp. en. *Proceedings of the National Academy of Sciences* **114.** ISSN: 0027-8424, 1091-6490. https://pnas.org/doi/full/10.1073/pnas.1706162114 (2022) (Sept. 2017).
16. PBS. *Wasp Deposits Parasitic Larvae Deep Inside Tree Trunk* https://www.pbs.org/wnet/nature/forest-lynx-wasp-deposits-parasitic-larvae-deep-inside-tree-trunk/15266/.

17. Polidori, C., García, A. J. & Nieves-Aldrey, J. L. Breaking up the Wall: Metal-Enrichment in Ovipositors, but Not in Mandibles, Co-Varies with Substrate Hardness in Gall-Wasps and Their Associates. en. *PLoS ONE* **8** (ed Fontaneto, D.) e70529. ISSN: 1932-6203. https://dx.plos.org/10.1371/journal.pone.0070529 (2023) (July 2013).

18. Cerkvenik, U., Dodou, D., van Leeuwen, J. L. & Gussekloo, S. W. S. Functional principles of steerable multi-element probes in insects: Functional principles of insect probes. en. *Biological Reviews* **94,** 555–574. ISSN: 14647931. https://onlinelibrary.wiley.com/doi/10.1111/brv.12467 (2022) (Apr. 2019).

19. Matheson, E. & Rodriguez y Baena, F. Biologically Inspired Surgical Needle Steering: Technology and Application of the Programmable Bevel-Tip Needle. en. *Biomimetics* **5,** 68. ISSN: 2313-7673. https://www.mdpi.com/2313-7673/5/4/68 (2022) (Dec. 2020).

20. Scali, M., Breedveld, P. & Dodou, D. Experimental evaluation of a self-propelling bio-inspired needle in single- and multi-layered phantoms. en. *Scientific Reports* **9,** 19988. ISSN: 2045-2322. https://www.nature.com/articles/s41598-019-56403-0 (2023) (Dec. 2019).

21. Bloemberg, J., Trauzettel, F., Coolen, B., Dodou, D. & Breedveld, P. Design and evaluation of an MRI-ready, self-propelled needle for prostate interventions. en. *PLOS ONE* **17** (ed Ranzani, T.) e0274063. ISSN: 1932-6203. https://dx.plos.org/10.1371/journal.pone.0274063 (2022) (Sept. 2022).

22. Pusch, T. P. From the Wasp Ovipositor to a 3D Steerable Needle for Solid-Tissue Interventions. en.

23. Frasson, L. *et al.* STING: a soft-tissue intervention and neurosurgical guide to access deep brain lesions through curved trajectories. en. *Proceedings of the Institution of Mechanical Engineers, Part H: Journal of Engineering in Medicine* **224,** 775–788. ISSN: 0954-4119, 2041-3033. http://journals.sagepub.com/doi/10.1243/09544119JEIM663 (2022) (June 2010).

24. Sprang, T., Breedveld, P. & Dodou, D. en. in *Biomimetic and Biohybrid Systems* (eds Lepora, N. F. *et al.*) Series Title: Lecture Notes in Computer Science, 307–318 (Springer International Publishing, Cham, 2016). ISBN: 978-3-319-42416-3 978-3-319-42417-0. http://link.springer.com/10.1007/978-3-319-42417-0_28 (2023).

25. Scali, M., Pusch, T. P., Breedveld, P. & Dodou, D. Ovipositor-inspired steerable needle: design and preliminary experimental evaluation. en. *Bioinspiration & Biomimetics* **13,** 016006. ISSN: 1748-3190. https://iopscience.iop.org/article/10.1088/1748-3190/aa92b9 (2022) (Dec. 2017).

26. Scali, M. *Self-propelling needles: From biological inspiration to percutaneous interventions* en. PhD thesis (Delft University of Technology, 2020). http://resolver.tudelft.nl/uuid:523e3e5f-08f0-4acb-ab45-abaa7ace3967 (2023).

27. Hall, T. L., Hempel, C. R., Sabb, B. J. & Roberts, W. W. Acoustic Access to the Prostate for Extracorporeal Ultrasound Ablation. en. *Journal of Endourology* **24,** 1875–1881. ISSN: 0892-7790, 1557-900X. http://www.liebertpub.com/doi/10.1089/end.2009.0567 (2023) (Nov. 2010).

28. Horuz, R. *et al.* Simple preoperative parameters to assess technical difficulty during a radical perineal prostatectomy. en. *International Urology and Nephrology* **45,** 129–133. ISSN: 0301-1623, 1573-2584. http://link.springer.com/10.1007/s11255-012-0310-1 (2023) (Feb. 2013).

29. *ASTM F2503-23, Standard Practice for Marking Medical Devices and Other Items for Safety in the Magnetic Resonance Environment.* West Conshohocken, PA., May 2023. https://compass.astm.org/document/?contentCode=ASTM%7CF2503-23%7Cen-US (2023).

30. *ISO 10993-1:2018(en) Biological evaluation of medical devices.* 2018. https://www.iso.org/obp/ui/en/#iso:std:iso:10993:-1:ed-5:v2:en.

31. *ASTM F3208-20, Selecting Test Soils for Validation of Cleaning Methods for Reusable Medical Devices* West Conshohocken, PA., 2020. https://www.astm.org/f3208-19.html.

32. Wiley, J. HANDBOOK OF HUMAN FACTORS AND ERGONOMICS. en.
33. Schroeck, F. R. *et al.* Satisfaction and Regret after Open Retropubic or Robot-Assisted Laparoscopic Radical Prostatectomy. en. *European Urology* **54,** 785–793. ISSN: 03022838. https://linkinghub.elsevier.com/retrieve/pii/S0302283808007641 (2023) (Oct. 2008).
34. McDermott, H., Choudhury, N., Lewin-Runacres, M., Aemn, I. & Moss, E. Gender differences in understanding and acceptance of robot-assisted surgery. en. *Journal of Robotic Surgery* **14,** 227–232. ISSN: 1863-2483, 1863-2491. http://link.springer.com/10.1007/s11701-019-00960-z (2023) (Feb. 2020).
35. Boeijen van, A., Daalhuizen, J., Zijlstra, J. & Schoor van der, R. *Delft Design Guide* 2nd ed. English. ISBN: 978-90-6369-327-5 (BIS Publishers, Amsterdam, 2014).
36. Filipov, E. T., Tachi, T. & Paulino, G. H. Origami tubes assembled into stiff, yet reconfigurable structures and metamaterials. en. *Proceedings of the National Academy of Sciences* **112,** 12321–12326. ISSN: 0027-8424, 1091-6490. https://pnas.org/doi/full/10.1073/pnas.1509465112 (2023) (Oct. 2015).
37. Van Oosterhout, A. & Hoggan, E. *Reshaping Interaction with Rotary Knobs: Combining Form, Feel and Function* en. in *Proceedings of the 2020 ACM Designing Interactive Systems Conference* (ACM, Eindhoven Netherlands, July 2020), 1973–1982. ISBN: 978-1-4503-6974-9. https://dl.acm.org/doi/10.1145/3357236.3395536 (2023).
38. Oberg, E., Jones, F. D., Horton, H. L. & Ryffel, H. H. *Machinery's Handbook (30th Edition) - 95. Cams and Cam Design* https://app.knovel.com/hotlink/pdf/id:kt010ZW6F1/machinerys-handbook-30th/cams-and-cam-design (Industrial Press, 2016).
39. Bloemberg, J. *MRI-Ready Actuation System for a SelfPropelling Needle - A Design and Experimental Approach* PhD thesis (Delft University of Technology, 2021). http://repository.tudelft.nl/.
40. TommyGami. *Miura Tube Digital Folding Template (8.5"x11")* English. https://tommygami.com/products/miura-tube-digital-folding-template-8-5x11 (2023).
41. Kot, B. C. W., Zhang, Z. J., Lee, A. W. C., Leung, V. Y. F. & Fu, S. N. Elastic Modulus of Muscle and Tendon with Shear Wave Ultrasound Elastography: Variations with Different Technical Settings. en. *PLoS ONE* **7** (ed Kellermayer, M. S.) e44348. ISSN: 1932-6203. https://dx.plos.org/10.1371/journal.pone.0044348 (2023) (Aug. 2012).
42. Ji, Y. *et al.* Stiffness of prostate gland measured by transrectal real-time shear wave elastography for detection of prostate cancer: a feasibility study. en. *The British Journal of Radiology* **92,** 20180970. ISSN: 0007-1285, 1748-880X. https://www.birpublications.org/doi/10.1259/bjr.20180970 (2023) (May 2019).
43. Sakes, A., Dodou, D. & Breedveld, P. Buckling prevention strategies in nature as inspiration for improving percutaneous instruments: a review. en. *Bioinspiration & Biomimetics* **11,** 021001. ISSN: 1748-3190. https://iopscience.iop.org/article/10.1088/1748-3190/11/2/021001 (2023) (Feb. 2016).
44. O'Sullivan, S. *et al.* Legal, regulatory, and ethical frameworks for development of standards in artificial intelligence (AI) and autonomous robotic surgery. en. *The International Journal of Medical Robotics and Computer Assisted Surgery* **15,** e1968. ISSN: 1478-5951, 1478-596X. https://onlinelibrary.wiley.com/doi/10.1002/rcs.1968 (2023) (Feb. 2019).
45. Flemisch, F., Abbink, D. A., Itoh, M., Pacaux-Lemoine, M.-P. & Weßel, G. Joining the blunt and the pointy end of the spear: towards a common framework of joint action, human–machine cooperation, cooperative guidance and control, shared, traded and supervisory control. en. *Cognition, Technology & Work* **21,** 555–568. ISSN: 1435-5558, 1435-5566. http://link.springer.com/10.1007/s10111-019-00576-1 (2023) (Nov. 2019).
46. Abbink, D. A., Mulder, M. & Boer, E. R. Haptic shared control: smoothly shifting control authority? en. *Cognition, Technology & Work* **14,** 19–28. ISSN: 1435-5558, 1435-5566. http://link.springer.com/10.

1007/s10111-011-0192-5 (2023) (Mar. 2012).

47. Lin, X. *et al.* A novel multi-DoF surgical robotic system for brachytherapy on liver tumor: Design and control. en. *International Journal of Computer Assisted Radiology and Surgery* **16,** 1003–1014. ISSN: 1861-6410, 1861-6429. https://link.springer.com/10.1007/s11548-021-02380-7 (2023) (June 2021).

48. Fichtinger, G. *et al.* Robotic assistance for ultrasound-guided prostate brachytherapy. en. *Medical Image Analysis* **12,** 535–545. ISSN: 13618415. https://linkinghub.elsevier.com/retrieve/pii/S1361841508000613 (2023) (Oct. 2008).

49. Becerra, V. *et al.* Economic evaluation of treatments for patients with localized prostate cancer in Europe: a systematic review. en. *BMC Health Services Research* **16,** 541. ISSN: 1472-6963. http://bmchealthservres.biomedcentral.com/articles/10.1186/s12913-016-1781-z (2023) (Dec. 2016).

50. Roesthuis, R. Mechanics of Needle-Tissue Interaction. English. *IEEE International Conference on Intelligent Robots and Systems,* 2557–2563. https://ieeexplore.ieee.org/stamp/stamp.jsp?arnumber=6094969 (2011).

51. Khodaei, S., Sahlabadi, M. & Hutapea, P. *Design of Smart Barb of Honeybee-Inspired Surgery Needle* en. in *Volume 1: Development and Characterization of Multifunctional Materials; Mechanics and Behavior of Active Materials; Bioinspired Smart Materials and Systems; Energy Harvesting; Emerging Technologies* (American Society of Mechanical Engineers, Snowbird, Utah, USA, Sept. 2017), V001T06A012. ISBN: 978-0-7918-5825-7. https://asmedigitalcollection.asme.org/SMASIS/proceedings/SMASIS2017/58257/Snowbird,%20Utah,%20USA/281868 (2022).

52. Shabalovskaya, S. & Van Humbeeck, J. en. in *Shape Memory Alloys for Biomedical Applications* 194–233 (Elsevier, 2009). ISBN: 978-1-84569-344-2. https://linkinghub.elsevier.com/retrieve/pii/B9781845693442500092 (2023).

53. Kane, M. Unsafe injections. *Bulletin of the World Health Organization,* **76,** 99–100 (1998).

54. *ISO 11737-2:2019(en) Sterilization of health care products — Microbiological methods — Part 2: Tests of sterility performed in the definition, validation and maintenance of a sterilization process* 2019. https://www.iso.org/obp/ui/#iso:std:iso:11737:-2:ed-3:v1:en.

55. *REGULATION (EU) 2017/745 OF THE EUROPEAN PARLIAMENT AND OF THE COUNCIL of 5 April 2017 on medical devices, amending Directive 2001/83/EC, Regulation (EC) No 178/2002 and Regulation (EC) No 1223/2009 and repealing Council Directives 90/385/EEC and 93/42/EEC* 2023. http://data.europa.eu/eli/reg/2017/745/2023-03-20.

56. Devices, A. M. *Pro-Mag™ Ultra Automatic Biopsy Instrument*

57. Deacon, B. & Abramowitz, J. Fear of needles and vasovagal reactions among phlebotomy patients. en. *Journal of Anxiety Disorders* **20,** 946–960. ISSN: 08876185. https://linkinghub.elsevier.com/retrieve/pii/S0887618506000041 (2023) (Jan. 2006).

58. McLenon, J. & Rogers, M. A. The fear of needles: A systematic review and meta□analysis. en. *Journal of Advanced Nursing* **75,** 30–42. ISSN: 0309-2402, 1365-2648. https://onlinelibrary.wiley.com/doi/10.1111/jan.13818 (2023) (Jan. 2019).

59. Rudnick, A. On the Notion of (Medical) Invasiveness. en. *Health Care Analysis* **19,** 99–106. ISSN: 1065-3058, 1573-3394. http://link.springer.com/10.1007/s10728-010-0149-5 (2023) (June 2011).

60. De Marco, G., Simons, J., Forsberg, L. & Douglas, T. What makes a medical intervention invasive? en. *Journal of Medical Ethics,* jme–2023–109301. ISSN: 0306-6800, 1473-4257. https://jme.bmj.com/lookup/doi/10.1136/jme-2023-109301 (2023) (Sept. 2023).

61. Scali, M., Pusch, T. P., Breedveld, P. & Dodou, D. Needle-like instruments for steering through solid organs: A review of the scientific and patent literature. en. *Proceedings of the Institution of Mechanical Engineers, Part H: Journal of Engineering in Medicine* **231,** 250–265. ISSN: 0954-4119, 2041-3033. http://journals.sagepub.com/doi/10.1177/0954411916672149 (2023) (Mar. 2017).

62. Ryu, S. C. *et al.* Design of an Optically Controlled MR-Compatible Active Needle. en. *IEEE Transactions on Robotics* **31,** 1–11. ISSN: 1552-3098, 1941-0468. http://ieeexplore.ieee.org/document/6963388/ (2023) (Feb. 2015).

63. Torabi, M., Gupta, R. & Walsh, C. J. Compact Robotically Steerable Image-Guided Instrument for Multi-Adjacent-Point (MAP) Targeting. en. *IEEE Transactions on Robotics* **30,** 802–815. ISSN: 1552-3098, 1941-0468. http://ieeexplore.ieee.org/document/6776478/ (2023) (Aug. 2014).

64. Swaney, P. J., Burgner, J., Gilbert, H. B. & Webster, R. J. A Flexure-Based Steerable Needle: High Curvature With Reduced Tissue Damage. en. *IEEE Transactions on Biomedical Engineering* **60,** 906–909. ISSN: 0018-9294, 1558-2531. http://ieeexplore.ieee.org/document/6362190/ (2023) (Apr. 2013).

65. Ng, P. K. & Saptari, A. A review of shape and size considerations in pinch grips. en. *Theoretical Issues in Ergonomics Science* **15,** 305–317. ISSN: 1463-922X, 1464-536X. http://www.tandfonline.com/doi/abs/10.1080/1463922X.2012.729619 (2023) (May 2014).

66. *Formuleboekje* ISBN: 978-90-810406-2-4 (Microcentrum, Eindhoven Netherlands).

67. Hulburt, T., Booth, J., Pan, P. & Brown, P. Characterization of Spinal Needle Buckling Behavior. en. *Journal of Medical Devices* **13,** 041003. ISSN: 1932-6181, 1932-619X. https://asmedigitalcollection.asme.org/medicaldevices/article/13/4/041003/727244/Characterization-of-Spinal-Needle-Buckling (2023) (Dec. 2019).

A. Observations prostate MRI fusion biopsy

We attended a prostate MRI fusion biopsy in the Amsterdam university medical centre (AUMC) to get a better view of the context during TPLA procedures. It was not possible to attend a TPLA procedure because this procedure is currently not executed in the Netherlands. Currently, the AUMC researchers are waiting for funding in order to proceed the research on TPLA procedures.

Date: April 3, 2023
Duration: 1 hour
Location: VUmc polikliniek
Attendees: Katelijne de Bie (Resident not in training, department of Urology, AUMC), nurse, nurse student, patient, Jette Bloemberg (PhD, TU Delft), Zola Fung-A-Jou (student, TU Delft)
Procedure: MRI images of the prostate and suspected lesion within the prostate are projected over the live echoscopic image of the prostate. A biopt is taken for further investigation of the abnormal cells.
Biopt: Piece of tissue that is extracted from the body with a thickness of 1 mm and length of 20 mm.
Instruments:

- BK 5000 Echo (ultrasound): live visualisation of the prostate with abnormal cells and the needle position in the transversal and saggital plane.
- Biopsy instrument: extracts the biopt. Needle gun (Pro-Mag Ultra Automatic Biopsy Instrument, catalogue number: 7675, throw length: 25 mm) and disposable needle (Pro-Mag Biopsy Needle, 18 gauge x 20 cm, catalogue number: 765018200)
- Micro-Touch Stabilizer Stand: positions and stabilises the Stepper. Urologist can use two handles to move the stepper in all directions. Fastened in position with a rotary knob.
- EX3 Stepper: Positioning and clamping of the echo probe and the grit. The cranial-caudal position is adjusted with a rotary knob. The probe can be tilted to receive the echo image from a different angle. A grit is attached to a slider for positioning.
- AccuCARE System Drape: sterile protection shield of the Stabilizer and Stepper.
- AccuCARE Disposable Template Grit: corresponds with the layover on the echo-MRI images and guides the needle insertion.

Setting (Figure 25): The patient lays on an operating chair on its back with its upwards legs in clamps (i.e., lithotomy position). The urologist sits in front of the patient on a adjustable rolling chair with the perineum of the patient on eye height. The Stabilizer stand with the Stepper on top of it is located on the right of the urologist. On the left of the urologist the Echomonitor is located on a rolling cart. The nurses are standing behind a rolling cart that functions as table for the containers that preserve the collected biopts.
Procedure:

1. Urologist explains the procedure to the patient.
2. Urologist puts condom and lubricant around the Echo Transducer.
3. Patient removes its bottom clothing and lays in the operation chair. Its legs are put upwards in the leg clamps that support the knee and calves.
4. Urologist sticks the scrotum of the patient to its abdomen to free up the space around the perineum.
5. Urologist executes a rectal touche to feel the hardness of the prostate (malignant prostate cells have a harder consistency compared to benign prostate cells).
6. Urologist disinfects the perineal skin using chlorhexidine.
7. Urologist anaesthetises the perineum with two injections, using 10cc lidocaïne 2%.
8. Urologist brings the Echo Transducer in the rectum with a curved movement. The Stabilizer and Stepper are moved to position the echo, there should be enough contact between the echo and prostate, but not too much to prevent a deformed shape op the prostate. The saggital and transversal images appear on the monitor and are combined with the MRI image. The angle of the Echo Transducer is indicated with a red line on the monitor.
9. The urologist corrects the images overlay on the monitor that the prostate circumference (in blue) and the suspected lesion for prostate cancer (in pink) of the MRI images correspond the the live echo images.

10. Urologist measures the prostate volume.
11. Urologist covers the Stabilizer and Stepper with the Drape.
12. Urologist connects the Grit on the Stepper.
13. Urologist anaesthetises the prostate and surrounding tissue with three injections. The main focus is to anaesthetise the nerves and muscles.
14. Urologist looks at the echo images to retrieve the insertion position of the biopsy needle. The biopsy needle is then inserted with use of the Grit. The position of the needle is viewed on the monitor. The urologist can adjust the needle's position by gently retracting it out of the prostate (but the needle stays in the patient), subsequently orienting the needle downward, and then advancing it to achieve the desired placement.
15. The biopt is taken by activating the biopsy pistol. The needle position after shooting is predicted and indicated by a green rectangle on the monitor. The pistol shoots the needle 25 mm forward after which the end position can differ from the predicted position.
16. Urologist names the position of the biopt. The biopt positions are taken systematically from the peripheral zone of the prostate: from the apex, mid and base of the prostate. Both on the left and right side. Additionally biopsies are taken from the anterior fibromuscular stroma bilaterally. Also, targeted biopsies are taken from the previously deliniated suspected lesion in the prostate, as determined on MRI.
17. The nurse removes the tissue from the biopsy needle and puts it in the container. The position of the biopt is written on the lit of the container.
18. Urologist repeats steps 13-16. In total three target biopts are taken in the from the previously deliniated suspected intraprostatic lesion in the left prostate lobe (6c, 6b, 6d), four non-target biopts are taken in the left prostate (5c, 5d, 5b, 6b) for comparison and two non-target biopts in the right prostate lobe (3a, 2d).
19. Urogolist removes the Echo Transduces from the rectum and puts it to the right.
20. Urologist cleans the perineum from the gel and blood that occurred during the injections.
21. The patients puts a pad in its underwear to stop the bleeding and put back on its clothes.

Notes

- The software allows for the urologist to indicate in the echoscope images where the MRI deliniated suspected intraprostatic lesion is situated, the contours of the prostate and to mark the locations where biopts have been taken.
- Differences with the TPLA procedure: (1) an Echo Transducer with multi fibre guiding system is used instead of the Stabilizer, Stepper, Grit, (2) a 21-Gauge (0.8 mm) needle instead of 18-Gauge (1.3 mm) needle is used.

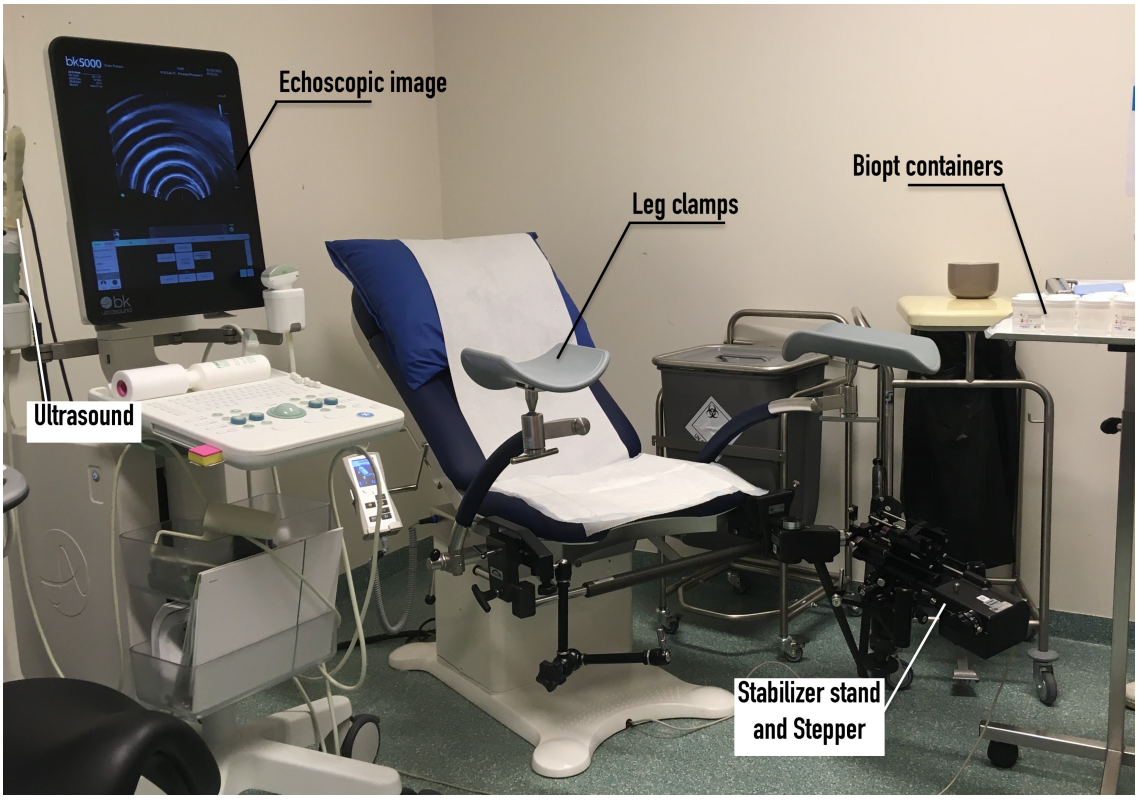

Figure 25: Set-up of the biopsy

B. Design process

The first step for the design for of the actuation system was creating a list of the required functions to make the system work. We conducted a brainstorm session was conducted for each function to find a number of sub-solutions. These functions and corresponding sub-solutions are listed in a morphological chart (Table B.1) [35]. The sub-solutions were combined to form concepts and from these concepts the most promising design concept that turned out to be best suited for this study was chosen.

Table B.1: Morphological chart, with on the y-axis the functions and on the x-axis the design sub-solutions per function. Each sub-solution is illustrated with the thick arrow indicating the input motion and the small arrow indicating the output motion. The final choices are highlighted in green.

# / *Function*	A	B	C	D	E	F	G	H
1. Generate a hand powered repetitive (continuous or step-wise) input motion	Linear input				Rotational input			Arbitrary input
	Push 	Shove 	Squeeze 	Pull 	Wheel 	Handle 	Ball joint 	Shake 
2. Convert rotational input to linear output	Rack-pinion 	Crank-shaft 	Screw-nut 	Archimede-an drive 	Belt-pulley 	Cam-follower 		
3. Actuate needle rods individually	Gears 	Cam 	Actuation per rod 					
4. Transfer rotation	Gears 	Interlocking 						
5. Allow needle bundle to travel 100 mm	Rolling 	Sliding 	Levitating 	Floating 	Air pressure 	Extending 		
6. Constrain 2 rotations and 3 translations	Slider 	Tape spring 	Leaf springs 					
7. Support needle rods	Telescopic 	Rail 	Inner 					

B.1. Actuation

B.1.1. Continuous input motion (1)

The first function the design need to fulfil is generating a continuous input motion that is actuated by hand power of the urologist. This can be done by a linear, rotational or any other arbitrary input. If the input is linear (e.g. joystick) the input range should be at least 100 mm or a repetitive back-and-forth motion, possibly with a spring. For the first option (i.e. 100 mm pushing) it would be hard for the urologist to control the input, because shoving something forward a precise distance is hard and it would take up lots of space. In the second option (i.e. repetitive motion) the backward motion is a counter-intuitive control for a forward motion [32]. For both, the linear motion probably has to be converted to a rotational motion in that case it is easier to directly give a rotational input. An arbitrary input may be hard to use and convert to an input into the desired direction.

That is why a rotation was chosen as input motion. A rotation allows for a continuous sequence of the needle rods. This rotation could be given by a wheel, handle or ball joint. A handle could be handy for a continuous rotation and not being limited by the wrist rotation range. The ball joint would give confusion of which motion is indicating a forward and which a backward movement of the needle. A wheel has intuitive input of clock-wise being a forward motion and counterclockwise being a backward motion [32]. A rotary knob was chosen because of the short force loop through the wrist of instead of the whole arm of the urologist.

Rotary knob design

The placement of the rotary knob can be on top, bottom, right, left or front of the system, and it position can influence the motion transmission (Figure 26). An input force the full system could easily result in errors, as accidental touches of the device might accidentally advance the needle rods. The choice between left or right placement may depend on the urologist's handedness, and although the majority of people is right handed, left-handed individuals should not be excluded. Top and bottom would require an extra part to transmit the direction of rotation, hence for simplicity it was chosen for a rotation in front and in line with the system.

There are numerous options for the knob shape (Figure 26). An organic shape with varying circumferences throughout and optimal hand grip could be designed. Alternatively, a cone-shaped knob with the diameter based on the largest male hand length and smallest female hand length. However, for this research cylinder shape with one diameter was selected. Exploring other shape options would require a separate form study and user testing, which is not the primary focus of this research.

The knob size is determined by the urologist's grip force. In the Netherlands one-third of the urologist is female, and with a growing trend in female doctor degrees, this percentage is likely to increase, thus female and male hand size should be taken into account. A larger knob provides a greater grip force, however, it if the size of the knob is too large it can cause tendon injuries, especially in repetitive movement [65]. A too small size of a knob reduces the contact area and can result in-workable for larger hand size urologists.

Therefore a minimum of the knob was set at the largest grip circumference of 181 mm of the human hand, based on measurements of Dutch adults aged 20-30 (>99.99, DINED), which translates to a minimum diameter of 58 mm. A maximum was set where the pinch is not overstretched, where twice the hand length is considered as a circumference. For the smallest hand length (Dutch adults mixed 20-60 DINED) of 135 mm this leads to a diameter of 86 mm. It was found that an optimum grip force opening between thumb and fingers is 76 for females and 83 for males [32]. Therefore an optimal circumference was chosen to be the average mixed grip circumference (135 mm) and the average grip force opening (79.5 mm), resulting in a diameter of 66 mm, which falls between the minimum and maximum criteria.

To minimise space usage the knob thickness should be minimum. The thickness of the knob was determined by one-third of the pointing finger length, thus the knob is gripped primarily by the upper finger joint. The minimum size corresponds to the largest pointing finger length, as a thicker knob can be gripped closer to the ends when individuals have smaller fingers. For Dutch adults aged 20-60 the maximum finger index has a length of 98 mm (>99.99% 1982, DINED), divided by three yields a minimum knob thickness of 33 mm (Figure 27). Other design features that can be integrated are knob serration for more grip [37], material choice and a ratchet mechanism for haptic feedback. However, this is out of the scope of this research and should be addressed in further studies.

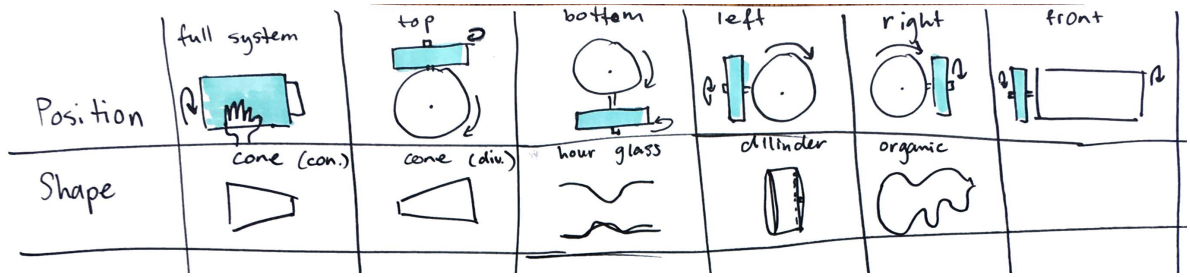

Figure 26: Options for knob features

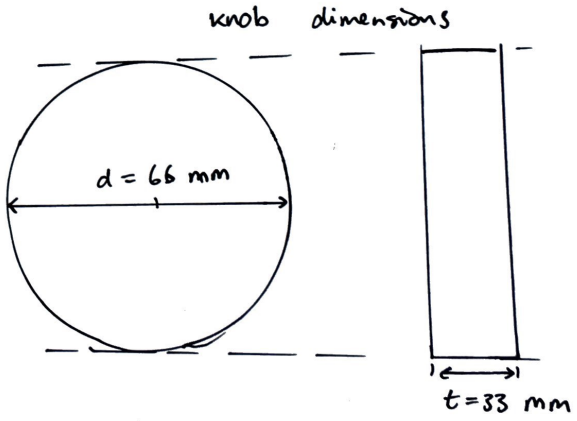

Figure 27: Final dimensions knob

B.1.2. Input conversion and individual rod actuation (2)(3)

The chosen rotational input needed to be transferred to the translation sequence of the needle rods, where the needle rods need to be actuated individually. Options to convert a rotational input to a linear output are a rack-pinion, crack-shaft, screw nut, Archimedes drive, belt-pulley of cam-follower mechanism. Actuation of the needle rods can be done by a actuation per rod or via a cam or gear system. Actuation per rod has be done by Sprang *et al.* with linear stepper motors, but would be hard to be executed by the urologist by hand (Function 1). The cam and gear mechanism both correspond to different rotation conversion mechanisms. From this a few sub-solutions follow. Sub-solution A consist of a drive with a gear in the middle that has teeth at 5/6 of the circumference and is smooth at 1/6 of its circumference and an outer ring that is the inverse, 1/6 with teeth and 5/6 smooth (Figure 28). In the drive lay six gears with fixed axes. When the drive is actuated clock-wise one gear turns also clockwise while the others turn counterclockwise. Rack-pinion or belt-pulley can be connected to these gears, resulting in one forward translation and five backward translations as needed. We did not choose this mechanism because of the high number of parts needed, increasing its complexity. Sub-solution B is the use of a cam mechanism. We chose for a cam, because of its low friction and energy waste. Also only one component is needed and it takes in little physical space.

Cam and followers design

The placement of the cam follower could be inside or outside of the cylinder depending on the placement of the other parts of the total system (Figure 29). For the determination of the cam path it does not matter yet, except the outer cylinder surface has a greater radius and circumference than the inner cylinder surface. Both design options are taken into the concepts.

The cam design path was made following the steps from the Machinery's handbook [38]. First the displacement diagram is sketched, where one cycle is one revolution of the cam i.e. 360° (Figure 30a). To determine the cam path the cycle is divided into six equal parts, each 60°. In the first 60° (a) the needle rod needs to travel a distance of stroke S in the y-direction (Figure 30a). In the remaining 300° (b-f) the needle rod need to travel back this stroke distance. It is preferred to have a uniform velocity during the stroke. However, this velocity profile has an infinite acceleration the beginning and end of the

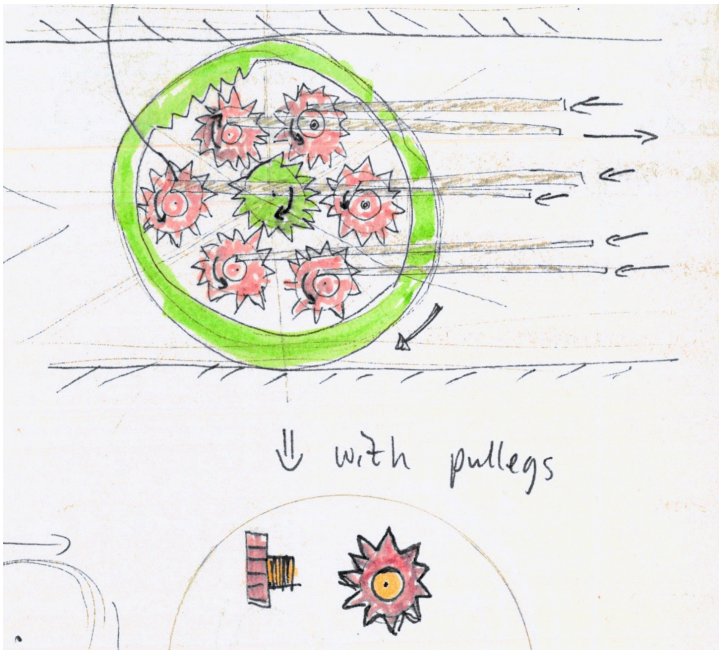

Figure 28: Sub-solution A: a drive (green) with a gear in the middle that has teeth at 5/6 of the circumference and is smooth at 1/6 of its circumference and an outer ring that is the inverse, 1/6 with teeth and 5/6 smooth. In the drive lay six gears with fixed axes (pink). When the drive is actuate clock-wise, one gear turns also clockwise while the others turn counterclockwise. Rack-pinion or belt-pulley (grey) can be connect to these gears, resulting in one forward translation and five backward translations.

stroke which causes a shock. To prevent this shock at the end while maintaining a constant velocity, the first 15° ($T1$) and last 15° ($T3$) are a parabolic function, reducing the accelerations at the ends from infinite to a finite constant. $T2$ covers the displacement stroke S with constant velocity. The next five steps (b-f) the rod travels back over a stroke distance, each step with a fifth of S and again with parabolic functions at the ends ($T4, T6$).

$y1 - y6$ can now be determined from T1-T6 with geometry as shown in Figure 30b, resulting in the following equations:

$$\frac{\frac{1}{2}T1}{T2} = \frac{y1}{y2} \tag{B.1}$$

$$\frac{T2}{\frac{1}{2}T3} = \frac{y2}{y3} \tag{B.2}$$

$$h = y1 + y2 + y3 \tag{B.3}$$

From these equations $y1$ can be solved the following:

$$y2 = 2y1\frac{T2}{T1} \tag{B.4}$$

$$y2 = h - y1 - y3 \tag{B.5}$$

$$y3 = \frac{1}{2}y2\frac{T3}{T2} \tag{B.6}$$

Substitution of equation B.6 in B.5 gives:

$$y2 = h - y1 - \frac{1}{2}y2\frac{T3}{T2} \tag{B.7}$$

$$y2 = \frac{h - y1}{1 + \frac{T3}{2T2}} \tag{B.8}$$

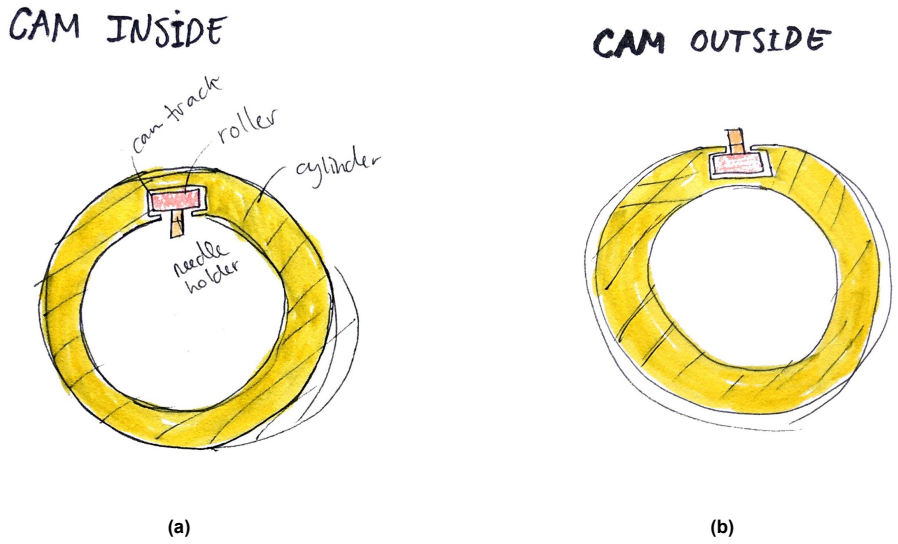

(a) (b)

Figure 29: Cam and follower placement. (a) Cam path and follower placement on the outer cylinder surface of the cam. (b) Cam path and follower placement on the inner cylinder surface of the cam

Equating equation B.4 and B.8 gives:

$$2y1\frac{T2}{T1} = \frac{h - y1}{1 + \frac{T3}{2T2}} \tag{B.9}$$

$$y1 = \frac{h/(1 + \frac{T3}{2T2})}{\frac{2T2}{T1} + 1/1 + \frac{T3}{2T2}} \tag{B.10}$$

The same calculations has been executed to calculate $y2 - y6$. The cam path was calculated from the points $y1 - y6$ and $T1 - T6$, where $Y1, Y3, Y4$ and $Y6$ follow a parabolic function (Equation B.11) and $Y2$ and $Y5$ follow a linear function (Equation B.12).

$$Y_i = 4y_i(\frac{t}{2T_i})^2 \tag{B.11}$$

$$Y_i = y_i\frac{t}{T_i} \tag{B.12}$$

The velocities and accelerations are calculated by taking the derivative of the functions $Y1 - Y6$.

$$V_i = \frac{dY_i}{dt} \tag{B.13}$$

$$A_i = \frac{dV_i}{dt} \tag{B.14}$$

The full calculations and corresponding MATLAB code can be found in Appendix D.1.

This cam path can now be adjusted according to the radius and following circumference of the cam. A radius as large as possible is desired to prevent undercutting and high surface stresses. However, this size is limited by the space that is permitted in the given space. The radius of the cam is determined by the diameter of the roller follower. Ideal would be the use of conical rollers, since the cam path is larger ate the top than at the bottom of the roller, this allows the rollers to rotate freely and limit friction. However, these are difficult to manufacture and bad manufacturing may result in a worse working mechanism. It is chosen to use cylindrical rollers, since these could be bought off-the-shelve. For MRI-compatible off-the-shelve bearings the material could be engineering thermoplastics, such as Polyoxymethylene (POM) or ceramics.

The smallest POM bearing found have a radius of 5 mm. In order to prevent undercutting and excessive surface stresses, the radius of the follower (r_f) should be smaller than the radius of the cam

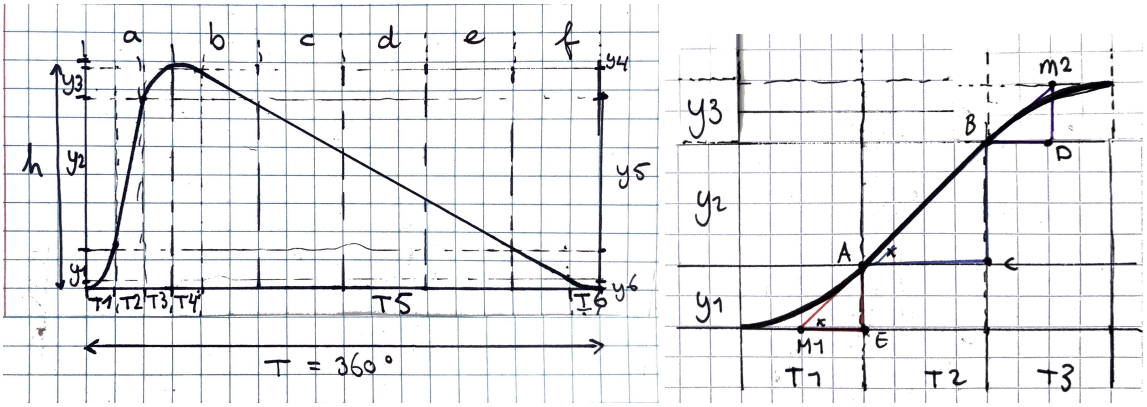

(a) Cam displacement annotations

(b) Construction lines for calculating y1-y6.

Figure 30: Sketches of the cam displacement and annotations

r_c. The cam radius surface should have a larger radius than 5 mm over the whole curve. Another thing is that the roller should be laying on an approximately flat surface. For a follower 5 mm in diameter this would result in a cam radius of 30mm, which is very large. Smaller ball bearings were found made from ceramics, with a diameter of 4 mm, however, these are very expensive. That is why it is chosen to work with metals where the smallest ball bearing found has an outer diameter of 3 mm and inner diameter of 1 mm. Which results in a cam radius smaller than 10 mm.

B.1.3. Transfer rotation and allowing translation (4)(5)

The rotational input needs to be transferred in order to actuate the cam and move the needle rods in a sequence. The needle rod sequence allows for the self-propelling motion and due to the friction forces between the tissue and needle rods, the needle bundle travels forward. It is important to note that this rotational transfer and forward travelling of the needle bundle occur at the same time. That is why function 4 and 5 are combined into one function: The system needs to transfer a rotation while allowing a translation of 100 mm.

Transferring a rotation can be done by connecting gears or a interlocking system, such as a spline. Interlocking is chosen as most promising option because less parts are needed, which results in a more compact mechanism. The two interlocking parts can move with respect to each other through rolling, sliding, levitating, floating, air pressure or extending. Sliding causes too much friction between the parts. Levitating through magnets is not desired if the system is used in MRI scanner. Floating and air pressure will increase the difficulty of the system by adding extra elements (Figure 31b). An extending part limits the working range of the system (Figure 31c). Therefore, rolling was chosen as most promising solution. Because we chose a cylindrical cam, it follows that the interlocking system consist of two cylinders. There are various possibilities of how the two cylinders interlock, a shape has been chosen later in the design process depending on the available parts (Figure 32).

Three prototypes has been made by 3D-printing with the Ultimaker 3 in Ultimaker White PLA to test whether the rolling motion works better with wheels or balls (Figure 33). The first prototype, straight grooves with wheels, shows that the wheels clamp in the tracks. The mechanism can either transfer torque or translate with low friction, but not at the same time (Figure 33a). This problem is solved when having a twisted groove and wheels, however, this second prototype pushes the outer cylinder forward and therefore interferes with the friction forces from the needle (Figure 33b). The third prototype, straight grooves with balls seems most promising. It can transfer high torques while allowing translation with low friction at the same time (Figure 33c).

B.2. Linear guidance

B.2.1. Constrain 2 translations and 3 rotations (6)

It is important for the needle rod sequence that the rods translate in a straight line, only translation in y-direction is allowed. Leaf springs could be used as linear guidance, however, they have a limited working range. A tape spring has a larger working range, however, in order to have a work range of 100 mm, 100 mm of the tape spring should hang unsupported. A stiff material is needed for 100 mm

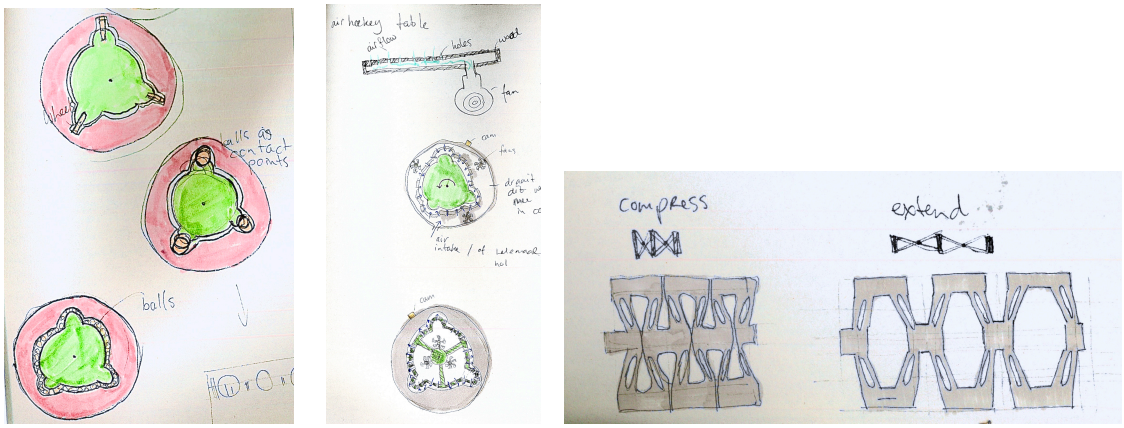

(a) (b) (c)

Figure 31: Sub-solutions of interlocking systems that transfer a rotation while allowing a translation. (a) Rolling with wheels or balls. (b) Air pressure through fans, like a air hockey system. (c) Extending with a compliant mechanism.

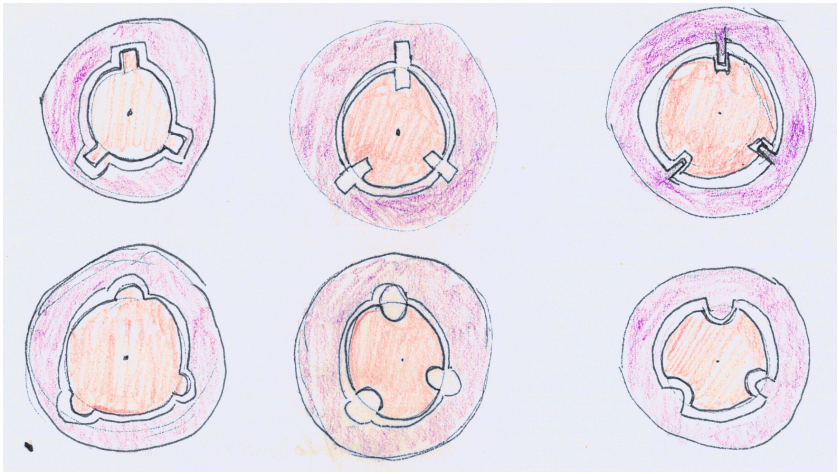

Figure 32: Shape iterations of interlocking cylinders.

unsupported length, but a stiff material will force out the spring function. We chose a slider with the same options as for function (5), as most promising solution. Figure 34 shows different options for the slider. The guide rail should be square to constrain rotation along the axis and a bearing could roll in the rail. Another solution is moving the rail between rollers instead, this solution will take up more space. We chose to use a rolling guide where balls roll through grooves in an axis.

B.3. System support

B.3.1. Support needle rods (7)

To prevent buckling of the needle rods outside the tissue, the unsupported rod length should be smaller than 2 cm (Appendix C). The support cannot be static because the needle bundle connected to the cam is moving, the support should follow this movement. A solution could be telescopic tubes, which are tubes with each a smaller diameter. When the cam (yellow) is translating the tubes can shove into each other (Figure 35a). Another solution is to let the support translate together with the cam in a rails (Figure 35b). Both options, however, have large friction over the supported length. Solution (c) seems more promising, where the support is placed between the needle rods. This support should be lightweight and only connected at a few point over the length of the needle rods. When the cam translates the connected point shove closer to each other.

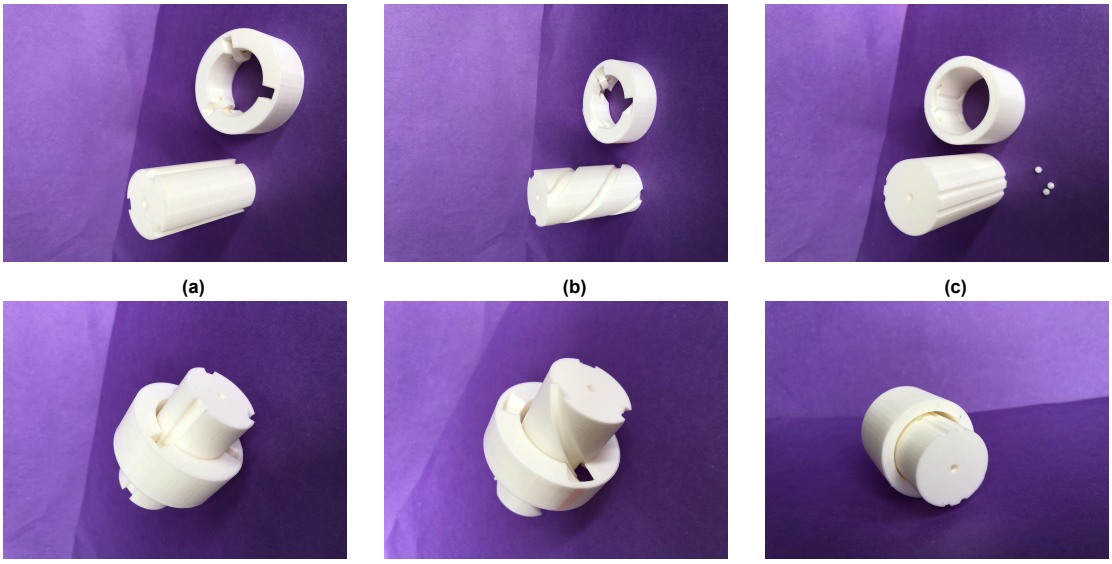

Figure 33: Prototypes of torque transfer options. (a)(d) Straight grooves and wheels. (b)(e) Twisted grooves and wheels. (c)(f) Straight grooves and balls.

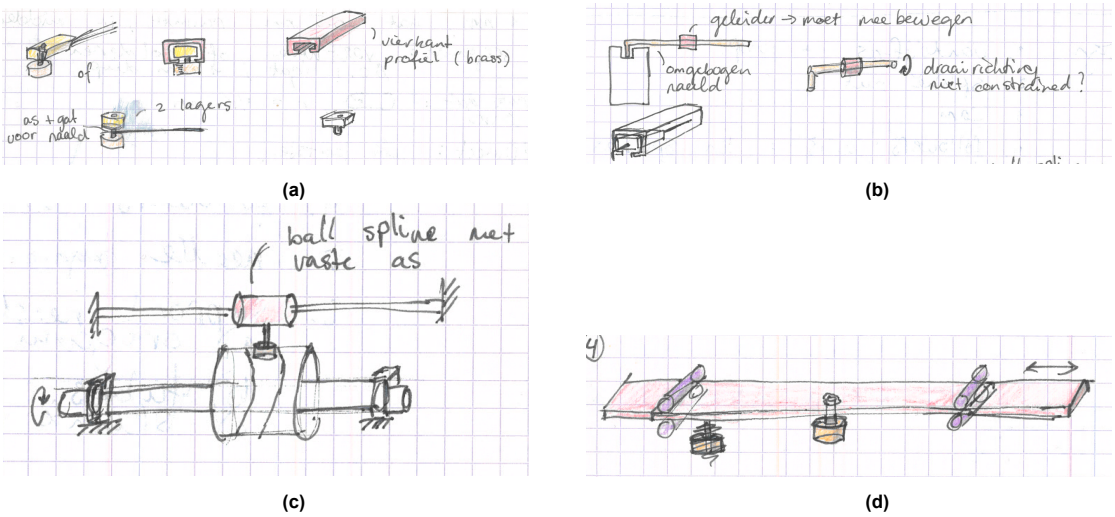

Figure 34: Sub-solutions for linear guidance. (a) Square profile with bearings. (b) Rod end in square profile. (c) Ball spline on fixed axis. (d) Plate between rollers.

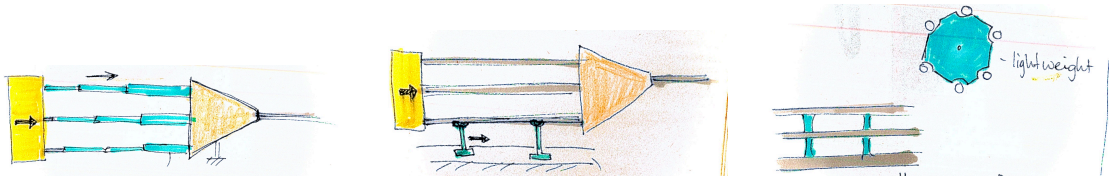

Figure 35: Sub-solutions for the support of the needle rods. (a) Between the rods. (b) Telescopic tubes. (c) Inside cylinder. (d) Rails.

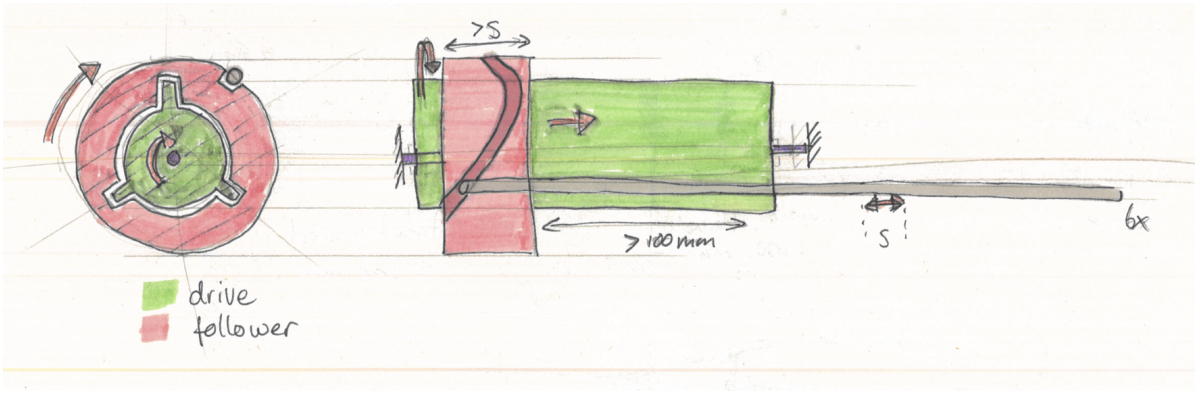

Figure 36: First concept sketch

B.4. Concepts

B.4.1. Configuration

The above sub-solutions determined the parts needed for the design. This resulted in a global image of the design that consists of two interlocking cylinders of which one is the drive (actuated by the hand of the urologist) and one is connected to a cam that is able to travel in y-direction (Figure 36). Needle rods are connected to the cam and are brought together to translate in the tissue as one needle bundle. To create concepts the configuration of all sub-solutions and corresponding parts was determined.

The actuation system needs to be connected to the ground. This can be done by given the actuation cylinder an inner axis or outer support (Figure 37). For both options the cam can be placed inside or outside the actuation cylinder, this results in four possible designs (Figure 37). Solution A1 and B2 are most promising, since the cam (green) is only in contact with the actuator and not with the support, which means less friction points. A second benefit for solution B2 is that the cam can travel freely to the right and is not limited by the support.

Figure 38 shows these two most promising design configurations worked out. Configuration B1 has an outer drive (pink) in which a cam (yellow) is placed inside that can rotate and translate because of grooves and balls between the parts. Needle rods (grey) are connected to the cam and brought together via a cones structure (orange). The system is supported outside the drive (blue) (Figure 38a). Configuration A1 has an inner drive (pink) over which a cam (yellow) is placed that can rotate and translate because of grooves and balls between the parts. Needle rods (grey) are connected to the cam and brought together via a cones structure (orange). The support (blue) is placed inside the drive in the form of an inner axis (Figure 38b).

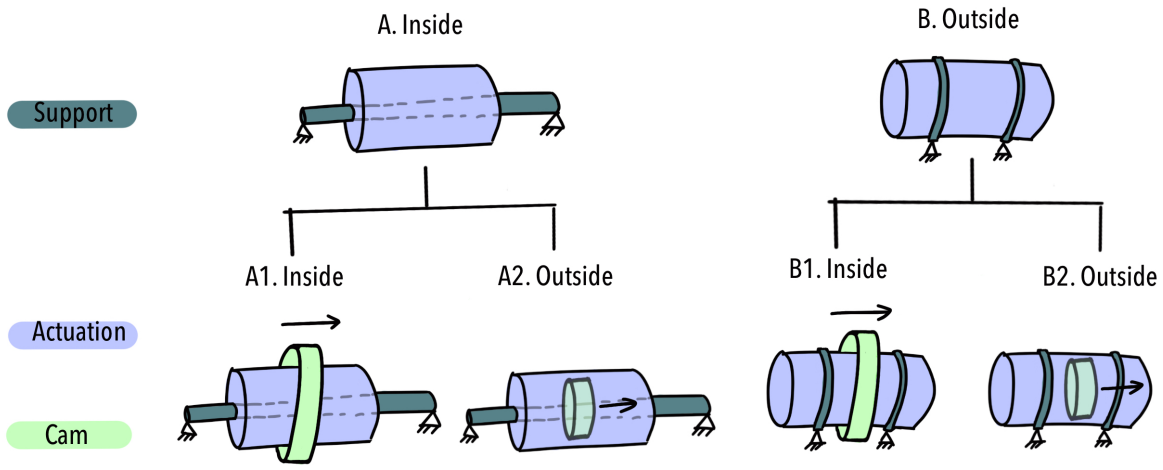

Figure 37: Options support location and cam placement. The actuation system (purple) can be supported inside or outside the cylinder. For both options the cam (green) can be placed inside or outside the cylinder, resulting in four possible designs.

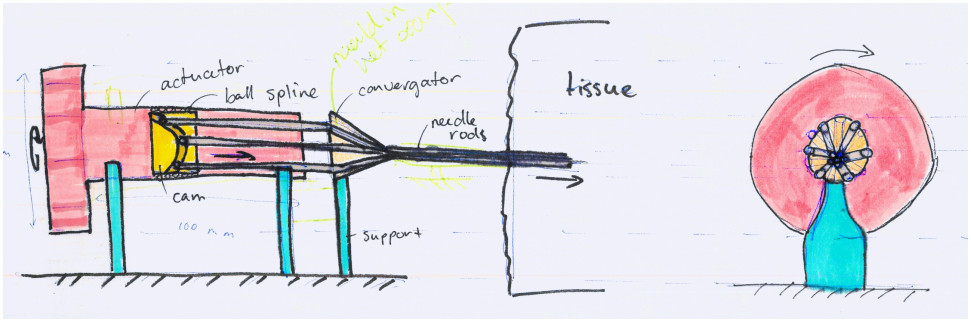

(a)

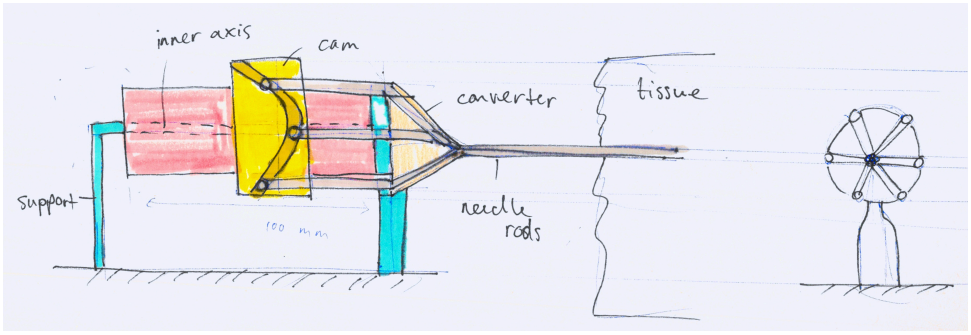

(b)

Figure 38: Two most promising design configurations. (a) Configuration B2: the drive (pink) is an outer cylinder, a cam (yellow) is placed inside the drive that can rotate and translate because of grooves and balls between the parts. Needle rods (grey) are connected to the cam and brought together via a cones structure (orange). Support (blue) is placed outside the drive. (b) Configuration A1: the drive (pink) is an inner cylinder, over which a cam (yellow) is placed that can rotate and translate because of grooves and balls between the parts. Needle rods (grey) are connected to the cam and brought together via a cones structure (orange). Support (blue) is placed inside the drive in the form of an inner axis.

C. Supplementary tests

C.1. Unsupported rod length

The maximum unsupported rod length is determined by the deflection of the unsupported rod. A block gelatin is placed on blocked paper at 1 cm distance the needle rod of diameter 0.3 mm inside a brass tube with an inner diameter of 0.4 mm and a length of 7.8 mm (Figure 39). The end of the rod is supported by a wooden block at different distances from 8 to 0 cm. From 8-5 cm buckling occurs and a clear deflection is seen in the rod. From 4-3 cm the deflection is minimal but buckling appears unpredictable. From 2-0 cm the deflection and buckling is not present. The gelatin should simulate the stiffness of human tissue. With perineal insertion the needle travels through muscle tissue and a tendon to the prostate (Figure 1). Muscle tissue has a Young's modulus of 12-32 kPa and tendons of 69-134 kPa [41]. Prostate gland with lesions has a Young's modulus between 20-98 kPa (benign) and 26-175 kPa (malignant) [42]. That is why it is chosen to work with a gelatin solution (Dr. Oetker) of 10% wt which has a Young's modulus of 26 kPa.

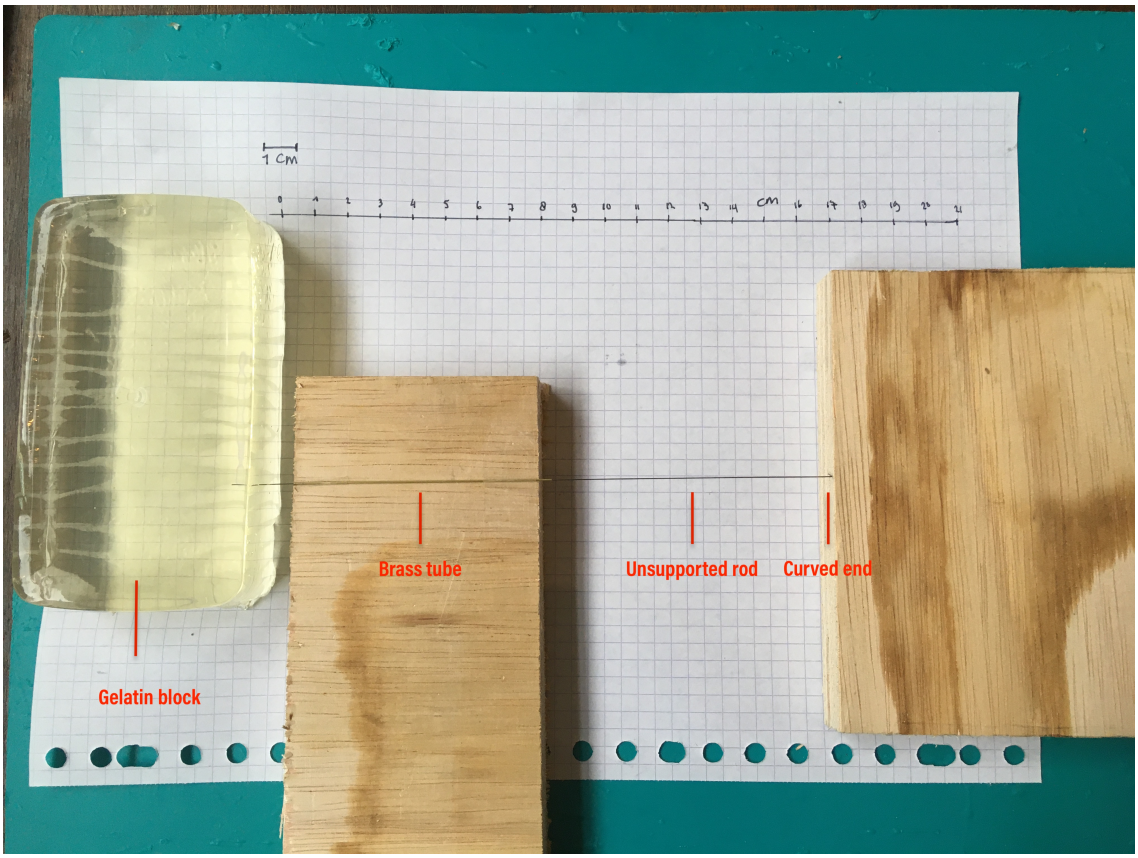

Figure 39: Test set up.

D. MATLAB codes cam design

D.1. Cam path

This appendix shows the MATLAB code for determining the cam path and its velocities and accelerations. The equations and parameters used in the code are elaborated on in appendix B.1.2.

```
%% Displacement, velocity and acceleration diagram cam
% MATLAB code for determining the cam path and its velocities
% Author: Zola Fung-A-Jou
% Last update: 7/9/2023

% Initialisation
close all; clear all; clc;

% Parameters
h = 4;                  % [mm] Total stroke S
Ta = 60;                % [deg] Time stroke a, forward stroke
Tb = 300;               % [deg] Time stroke b-f, backward stroke
rf = 1.5;               % [mm] Radius roller follower
rc = 10;                % [mm] Radius cylinder
o = 2*pi*rc;            % [mm] Circumference cylinder
syms t                  % [s]  Time step

% Steps in x-direction
k = o/360;              % [mm/deg]
T1 = 15 * k;            % [mm]
T3 = 15 * k;            % [mm]
T2 = Ta*k - T1 - T3;    % [mm]
T4 = 15 * k;            % [mm]
T6 = 15 * k;            % [mm]
T5 = Tb*k - T4 - T6;    % [mm]

% Steps in y-direction
y1 = ((2*T2/T3*h)/(1+2*T2/T3))/(2*T2/T1+(2*T2/T3)/(1+2*T2/T3));
y3 = ((2*T2/T1*h)/(1+2*T2/T1))/(2*T2/T3+(2*T2/T1)/(1+2*T2/T1));
y2 = h - y1 - y3;
y4 = ((2*T5/T6*h)/(1+2*T5/T6))/(2*T5/T4+(2*T5/T6)/(1+2*T5/T6));
y6 = ((2*T5/T4*h)/(1+2*T5/T4))/(2*T5/T6+(2*T5/T4)/(1+2*T5/T4));
y5 = h - y4 - y6;

% Displacement in x-direction
D1 = T1;                % [mm]
D2 = T1+T2;             % [mm]
D3 = T1+T2+T3;          % [mm]
D4 = T1+T2+T3+T4;       % [mm]
D5 = T1+T2+T3+T4+T5;    % [mm]
D6 = T1+T2+T3+T4+T5+T6; % [mm]

% Displacement in y-direction
Y1 = 4 * y1 * (t/(2*T1)).^2;
Y2 = y2 * t./T2 - y1;
Y3 = h-(4 * y3 * ((t-D3)/(2*T3)).^2);
Y4 = h-(4 * y4 * ((t-D3)/(2*T4)).^2);
C = h-(4*y4*(T4/(2*T4))^2) + y5/T5*D4;
Y5 = -y5 * t./T5 + C;
Y6 = 4 * y6 * ((t-360*k)/(2*T6)).^2;

```

```
% Velocities
V1 = diff(Y1, t);
V2 = diff(Y2, t);
V3 = diff(Y3, t);
V4 = diff(Y4, t);
V5 = diff(Y5, t);
V6 = diff(Y6, t);

% Accelerations
A1 = diff(V1, t);
A2 = diff(V2, t);
A3 = diff(V3, t);
A4 = diff(V4, t);
A5 = diff(V5, t);
A6 = diff(V6, t);

% Off-set lines displacement (cam diameter)
Y1_offset_up = Y1 + sind(90-atand(V1))*rf;
Y2_offset_up = Y2 + sind(90-atand(V2))*rf;
Y3_offset_up = Y3 + sind(90-atand(V3))*rf;
Y4_offset_up = Y4 + sind(90-atand(V4))*rf;
Y5_offset_up = Y5 + sind(90-atand(V5))*rf;
Y6_offset_up = Y6 + sind(90-atand(V6))*rf;

X1_offset_up = t - cosd(90-atand(V1))*rf;
X2_offset_up = t - cosd(90-atand(V2))*rf;
X3_offset_up = t - cosd(90-atand(V3))*rf;
X4_offset_up = t - cosd(90-atand(V4))*rf;
X5_offset_up = t - cosd(90-atand(V5))*rf;
X6_offset_up = t - cosd(90-atand(V6))*rf;

Y1_offset_down = Y1 - sind(90-atand(V1))*rf;
Y2_offset_down = Y2 - sind(90-atand(V2))*rf;
Y3_offset_down = Y3 - sind(90-atand(V3))*rf;
Y4_offset_down = Y4 - sind(90-atand(V4))*rf;
Y5_offset_down = Y5 - sind(90-atand(V5))*rf;
Y6_offset_down = Y6 - sind(90-atand(V6))*rf;

X1_offset_down = t + cosd(90-atand(V1))*rf;
X2_offset_down = t + cosd(90-atand(V2))*rf;
X3_offset_down = t + cosd(90-atand(V3))*rf;
X4_offset_down = t + cosd(90-atand(V4))*rf;
X5_offset_down = t + cosd(90-atand(V5))*rf;
X6_offset_down = t + cosd(90-atand(V6))*rf;

% Radius of curvature
rho1 = abs(((1+V1^2)^(3/2))/A1);        % Radius of curvature = (1+f'(x)
   ^2)^3/2 / f''(x)
rho1_min = double(subs(rho1, t, 0));    % Max curvature is min radius, min
    at the top of the parabola
rho2 = 0;                               % Straight line, no curvature
rho3 = abs(((1+V3^2)^(3/2))/A3);
rho3_min = double(subs(rho3, t, D3));
rho4 = abs(((1+V4^2)^(3/2))/A4);
rho4_min = double(subs(rho4, t, D3));
rho5 = 0;
```

```
rho6 = abs(((1+V6^2)^(3/2))/A6);
rho6_min = double(subs(rho6, t, D6));

% Figure displacement
subplot(3,1,1);
title("Displacement");
xlabel("Distance [mm]");
ylabel("Stroke [mm]");
hold on;
fplot(Y1,[0 D1],'color', 'r','LineWidth',2);
fplot(Y2,[D1 D2],'color', 'b','LineWidth',2);
fplot(Y3,[D2 D3],'color', 'r','LineWidth',2);
fplot(Y4,[D3 D4],'color', 'r','LineWidth',2);
fplot(Y5,[D4 D5],'color', 'b','LineWidth',2);
fplot(Y6,[D5 D6],'color', 'r','LineWidth',2);

fplot(X1_offset_up,Y1_offset_up,[0 D1],':','color', 'k','LineWidth',1);
fplot(X2_offset_up,Y2_offset_up,[D1 D2],':','color', 'k','LineWidth',1);
fplot(X3_offset_up,Y3_offset_up,[D2 D3],':','color', 'k','LineWidth',1);
fplot(X4_offset_up,Y4_offset_up,[D3 D4],':','color', 'k','LineWidth',1);
fplot(X5_offset_up,Y5_offset_up,[D4 D5],':','color', 'k','LineWidth',1);
fplot(X6_offset_up,Y6_offset_up,[D5 D6],':','color', 'k','LineWidth',1);

fplot(X1_offset_down, Y1_offset_down,[0 D1],':','color', 'k','LineWidth'
    ,1);
fplot(X2_offset_down,Y2_offset_down,[D1 D2],':','color', 'k','LineWidth'
    ,1);
fplot(X3_offset_down,Y3_offset_down,[D2 D3],':','color', 'k','LineWidth'
    ,1);
fplot(X4_offset_down,Y4_offset_down,[D3 D4],':','color', 'k','LineWidth'
    ,1);
fplot(X5_offset_down,Y5_offset_down,[D4 D5],':','color', 'k','LineWidth'
    ,1);
fplot(X6_offset_down,Y6_offset_down,[D5 D6],':','color', 'k','LineWidth'
    ,1);
axis([0 63 -2 6]);
hold off

% Figure velocity
subplot(3,1,2);
title("Velocity");
xlabel("Distance [mm]");
ylabel("Velocity [mm/s]");
hold on;
fplot(V1,[0 D1],'color', 'r','LineWidth',2);
fplot(V2,[T1 D2],'color', 'b','LineWidth',2);
fplot(V3,[D2 D3],'color', 'r','LineWidth',2);
fplot(V4,[D3 D4],'color', 'r','LineWidth',2);
fplot(V5,[D4 D5],'color', 'b','LineWidth',2);
fplot(V6,[D5 D6],'color', 'r','LineWidth',2);
axis([0 63 -0.1 0.6]);
hold off

% Figure acceleration
subplot(3,1,3);
title("Acceleration");
```

```
156 xlabel("Distance [mm]");
157 ylabel("Acceleration [mm/s^2]");
158 hold on;
159 fplot(A1,[0 D1],'color', 'r','LineWidth',2);
160 fplot(A2,[T1 D2],'color', 'b','LineWidth',2);
161 fplot(A3,[D2 D3],'color', 'r','LineWidth',2);
162 fplot(A4,[D3 D4],'color', 'r','LineWidth',2);
163 fplot(A5,[D4 D5],'color', 'b','LineWidth',2);
164 fplot(A6,[D5 D6],'color', 'r','LineWidth',2);
165 axis([0 63 -0.2 0.2]);
```

D.2. Cam radius

This appendix shows the MATLAB code for determining the cam's radius depending on the followers radius. The equations and parameters used in the code are elaborated on in appendix B.1.2.

```
%% Cylinder diameter
% MATLAB code for determining the minimum radius of the cam cylinder
% Author: Zola Fung-A-Jou
% Last update: 7/9/2023

% Initialisation
clc; clear all; close all;

% Parameters
syms rc l
rf = 1.5;           % [mm] Radius follower roller
hf = 1;             % [mm] Height follower roller
th = 0.015;          % [-]  Threshold
t = 6;              % [mm] Thickness cam

% Equations to determine minimum radius of the cam path
eq1 = rc == sqrt(l^2+rf^2);
eq2 = rc/l == 1 + th;
S = solve([eq1, eq2], [rc, l]);

rc = double(S.rc)   % [mm] Inner radius cam (cam path)
l = double(S.l)     % [mm] Comparison length

Ci = 2 * pi * rc    % [mm] Inner circumference cam

ro = rc + hf        % [mm] Outer radius cam
Co = 2 * pi * ro    % [mm] Outer circumference cam

% Plot of the follower and cam path radius
x = [-rf, rf, rf, -rf, -rf];
y = [rc, rc, hf+rc, hf+rc, rc];
plot(x, y,'Color', 'r','Linewidth',1.5);

y1 = [sqrt(rc^2-rf^2)-hf, sqrt(rc^2-rf^2)-hf, sqrt(rc^2-rf^2), sqrt(rc^2-
    rf^2), sqrt(rc^2-rf^2)-hf];

viscircles([0, 0],rc, 'Color', 'k','LineWidth',1);
viscircles([0, 0],ro,'Color', 'k','LineStyle',':','LineWidth',1);
viscircles([0, 0],0.1, 'Color', 'k','LineWidth',1);
pbaspect([1 1 1])

xlabel("Radius [mm]");
ylabel("Radius [mm]");
```

E. Experiment set-ups

This appendix shows the experimental set-up used to conduct the experiments discussed in Section 5.

E.1. Experiment 1A: Insertion force of the needle bundle

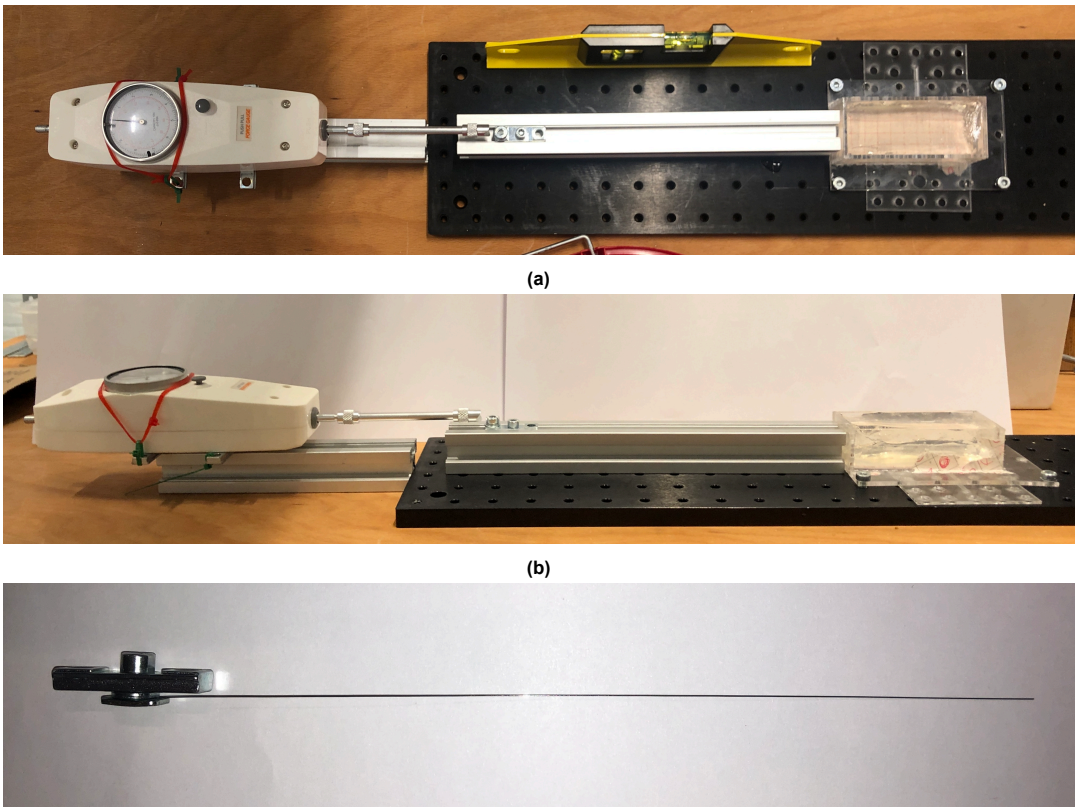

(a)

(b)

(c)

Figure 40: Set-up 1A: (a) Top view. (b) Side view. (c) Close-up needle bundle attachment to linear slide.

E.2. Experiment 1B: Force of the y-direction moving parts of the prototype

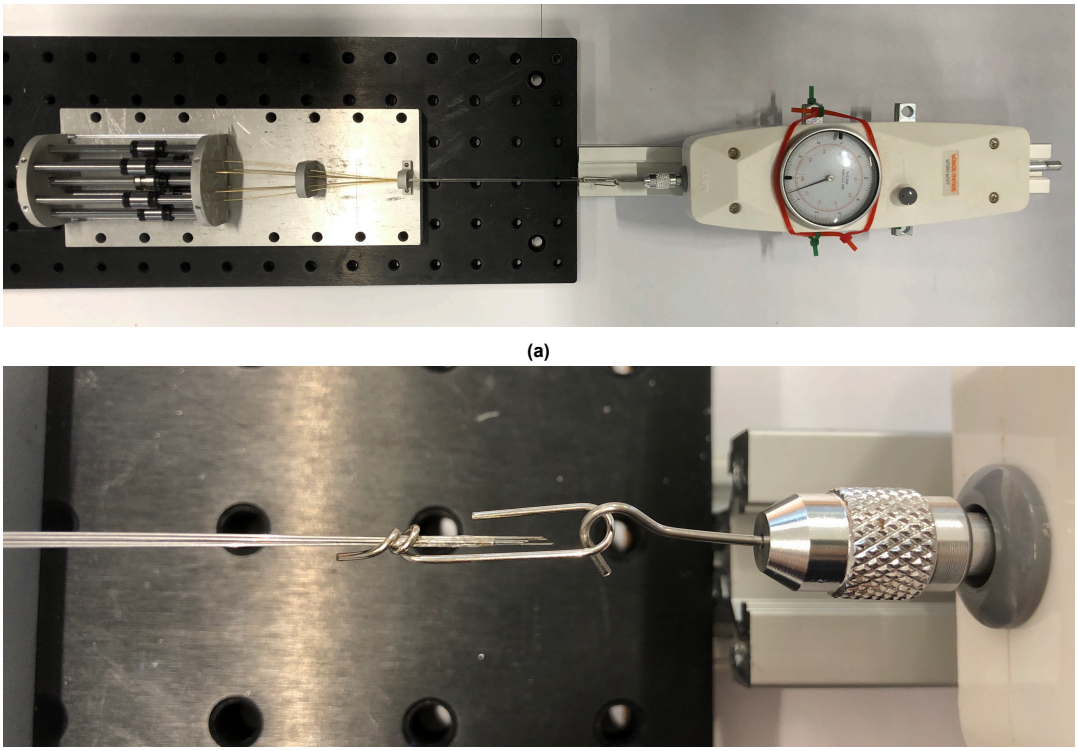

(a)

(b)

Figure 41: Set-up 1B: (a) Top view. (b) Close-up of paper clip hook to connect the needle bundle to the force gauge.

E.3. Experiment 1C: Force of the moving gelatin on a cart

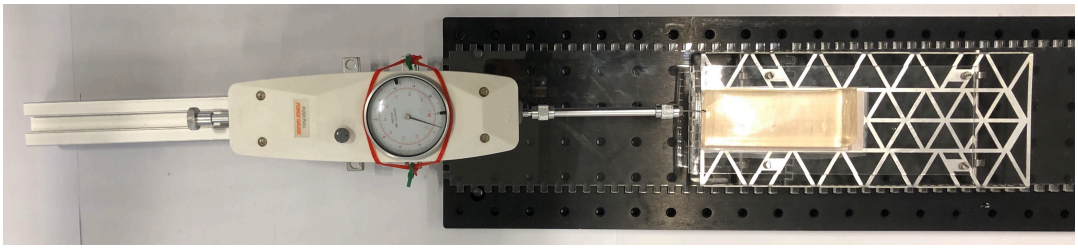

(a)

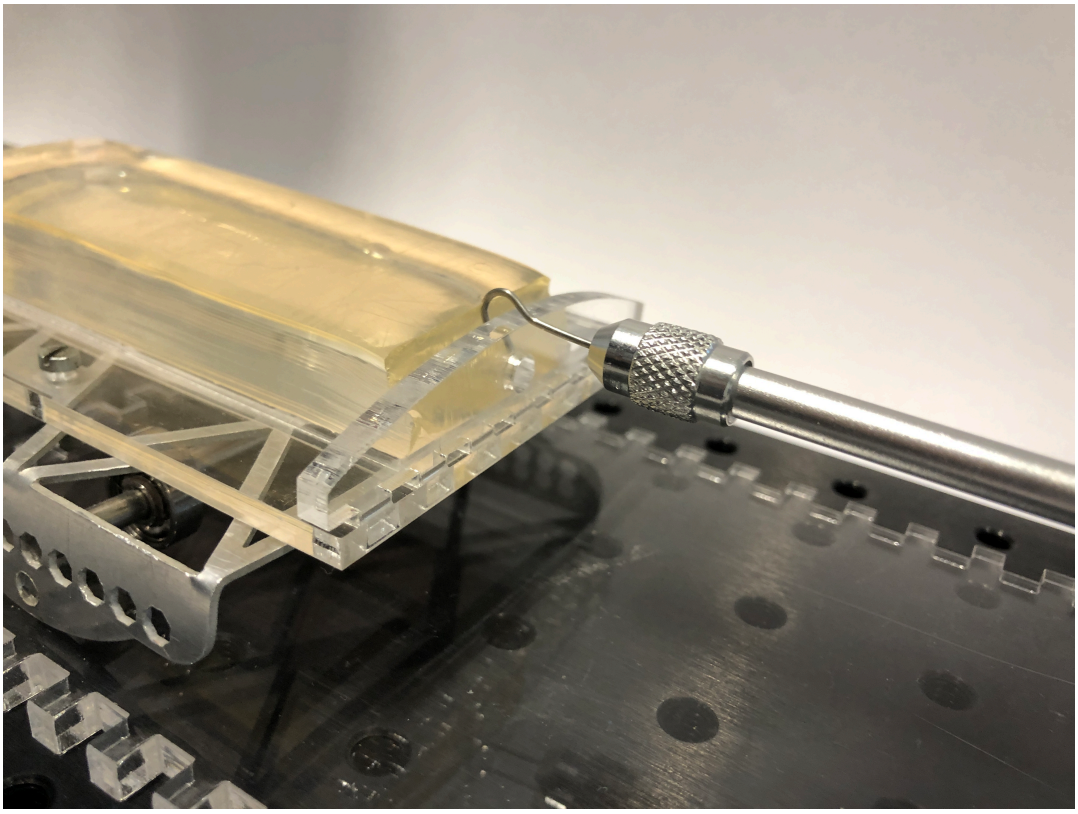

(b)

Figure 42: Set-up 1C: (a) Top view. (b) Close-up of paper the hook connect of the force gauge connected to the gelatin on a cart.

E.4. Experiment 1D: Net push force of the prototype

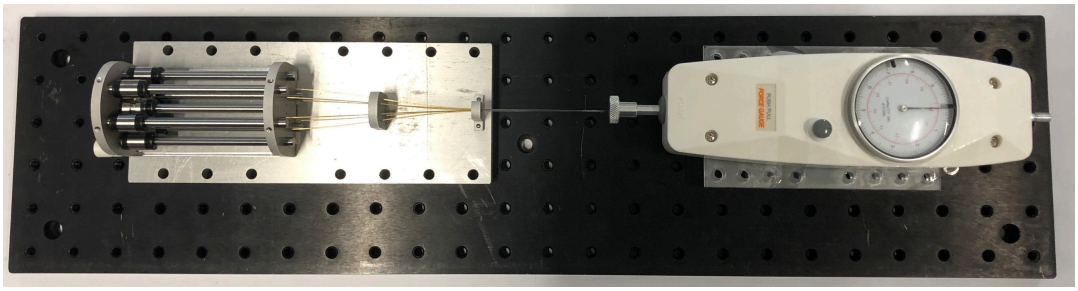

(a)

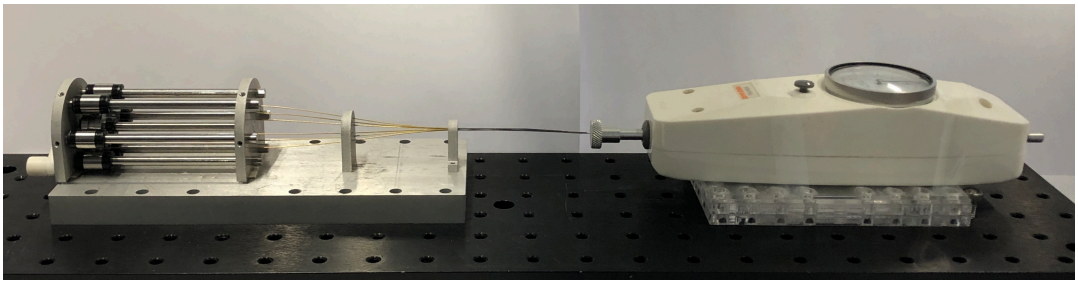

(b)

Figure 43: Set-up 1D: (a) Top view. (b) Side view.

E.5. Experiment 2A: Performance of the prototype in a gelatin sample of 15 wt%, with different insertion velocities

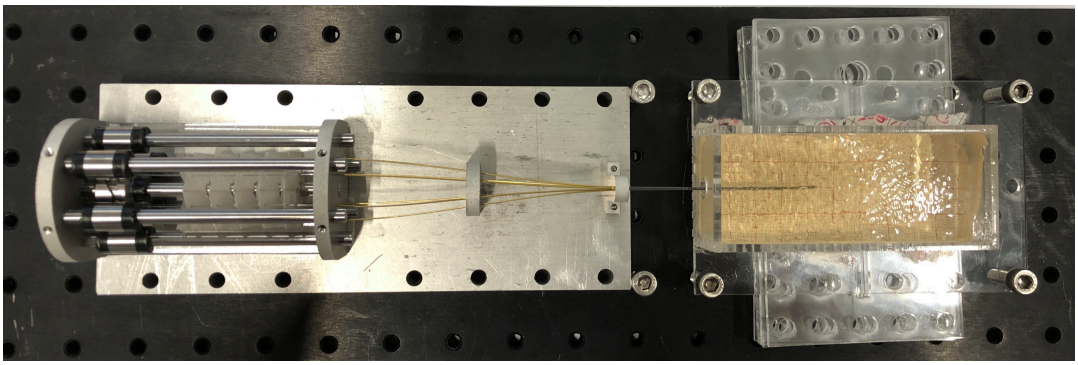

(a)

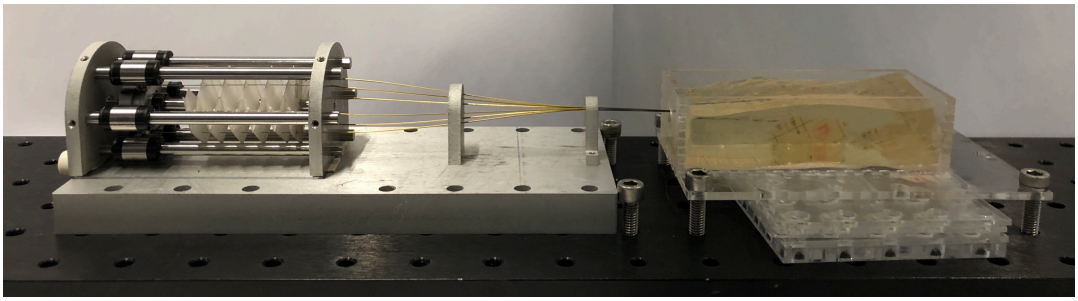

(b)

Figure 44: Set-up 1A: (a) Top view. (b) Side view.

E.6. Experiment 2B: Performance of the fixed prototype and a gelatin sample of 15 wt% on a moving cart, with different insertion velocities

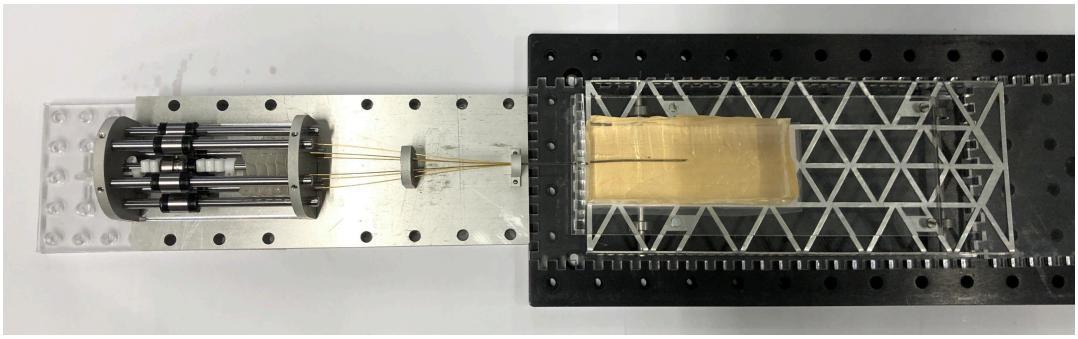

(a)

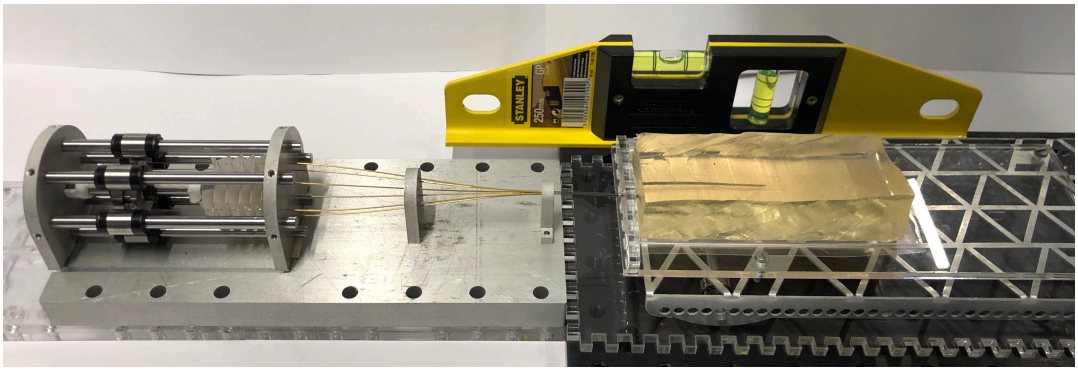

(b)

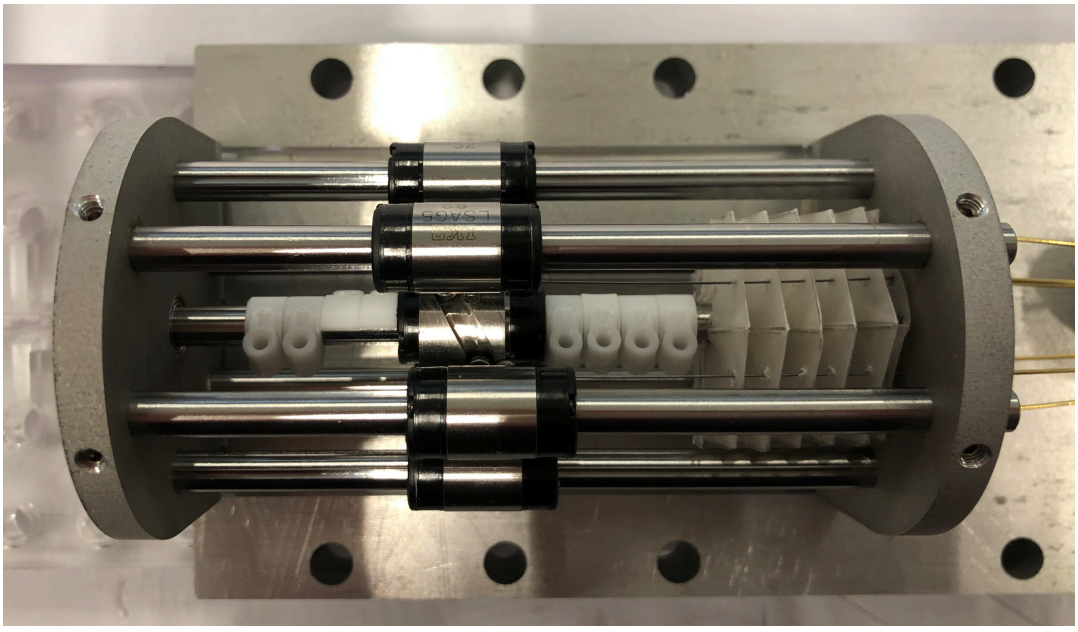

(c)

Figure 45: Set-up 1B: (a) Top view. (b) Side view. (c) Close-up of the fixed centre ball spline with cable clips.

F. Experiment results

This appendix shows the results of the experiments discussed in Section 4.2 and 5.

F.1. Preliminary experiment

Table F.1: Test results of prototype performance with support or without the origami support in 5, 10 and 15 wt% gelatin sample. The insertion velocity was 2 mm/s, the number of rotations 15 and the true distance s_t = 60 mm.

#	Support	wt %	Mass sample (g)	d_m (mm)	s_r	s_{rmean}
NS.5.1	no	5		53	0.117	
NS.5.2	no	5	94.0	53	0.117	0.122
NS.5.3	no	5		52	0.133	
NS.10.1	no	10		47	0.217	
NS.10.2	no	10	72.2	44	0.267	0.222
NS.10.3	no	10		49	0.183	
NS.15.1	no	15		13	0.783	
NS.15.2	no	15	105.1	16	0.733	0.756
NS.15.3	no	15		15	0.750	
S.5.1	yes	5		59	0.017	
S.5.2	yes	5	92.2	58	0.033	0.017
S.5.3	yes	5		60	0	
S.10.1	yes	10		58	0.033	
S.10.2	yes	10	71.6	59	0.017	0.028
S.10.3	yes	10		58	0.033	
S.15.1	yes	15		52	0.133	
S.15.2	yes	15	101.1	56	0.067	0.094
S.15.3	yes	15		55	0.083	

F.2. Experiment 1A: Insertion force of the needle bundle

Table F.2: Test results of experiment 1A: Insertion force of the needle in different gelatin concentrations, the measured insertion force, F_i and the calculated mean insertion force $F_{i,mean}$.

#	wt%	F_i(N)	$F_{i,mean}$(N)
A.5.1	5	0.25	
A.5.2	5	0.15	0.15
A.5.3	5	0.05	
A.10.1	10	0.75	
A.10.2	10	0.65	0.80
A.10.3	10	1.00	
A.15.1	15	-	
A.15.2	15	-	-
A.15.3	15	-	

F.3. Experiment 1B: Force of the y-direction moving parts of the prototype

Table F.3: Test results of experiment 1B: pulling force of the parts of the prototype that move in the y-direction (F_{proto}). Measurements have been conducted for the prototype with and without the origami support and the mean of the prototype force has been calculated ($F_{proto,mean}$)

#	Support	F_{proto}(N)	$F_{proto,mean}$(N)
B.NS.1	no	0.30	
B.NS.2	no	0.50	
B.NS.3	no	0.50	0.44
B.NS.4	no	0.35	
B.NS.5	no	0.55	
B.S.1	yes	1.50	
B.S.2	yes	1.35	
B.S.3	yes	1.10	1.27
B.S.4	yes	1.35	
B.S.5	yes	1.05	

F.4. Experiment 1C: Force of the moving gelatin on a cart

Table F.4: Test results of experiment 1C: force of pulling a gelatin sample on the cart.

#	F_{cart}(N)	$F_{cart,mean}$(N)
C.1	0.10	
C.2	0.25	0.13
C.3	0.05	

F.5. Experiment 1D: Net push force of the prototype

Table F.5: Test results of experiment 1D: net push force exerted by the prototype (F_{push})

#	Support	F_{push}(N)	$F_{push,mean}$(N)
D.NS.1	no	0.10	
D.NS.2	no	0.075	
D.NS.3	no	0.45	0.155
D.NS.4	no	0.10	
D.NS.5	no	0.05	
D.S.1	yes	0.15	
D.S.2	yes	0.10	
D.S.3	yes	0.05	0.175
D.S.4	yes	0.40	
D.S.5	yes	0.175	

F.6. Experiment 2: Performance in a gelatin sample of 15 wt%, with different insertion velocities. (A) of the prototype and (B) of the fixed prototype and the gelatin sample on a cart

Table F.6: Test results of experiment 2: the measured distances travelled (d_m) and slip ratio (s_r) under different insertion velocities.

#	Set-up	Velocity (mm/s)	Mass sample (g)	d_m (mm)	s_r	$s_{r,mean}$
2A.2.1	A	2	100.2	42	0.300	
2A.2.2	A	2	99.1	50	0.167	0.222
2A.2.3	A	2	99.6	48	0.200	
2A.4.1	A	4	99.0	48	0.200	
2A.4.2	A	4	99.2	46	0.233	0.167
2A.4.3	A	4	100.3	56	0.067	
2A.6.1	A	6	100.3	52	0.133	
2A.6.2	A	6	99.3	46	0.233	0.150
2A.6.3	A	6	99.1	55	0.083	
2B.2.1	B	2	99.0	29	0.517	
2B.2.2	B	2	100.8	38	0.367	0.450
2B.2.3	B	2	99.6	32	0.467	
2B.4.1	B	4	100.1	21	0.650	
2B.4.2	B	4	99.7	32	0.467	0.567
2B.4.3	B	4	100.3	25	0.583	
2B.6.1	B	6	99.1	26	0.567	
2B.6.2	B	6	100.8	25	0.583	0.589
2B.6.3	B	6	99.2	23	0.671	

G. Buckling calculations

The critical buckling load is defined by the Euler's load equation:

$$P_{cr} = \frac{\pi^2 EI}{(kL)^2} \tag{G.1}$$

Where E is the Young's Modulus of the needle, I the area moment of inertia of the needle, k is a coefficient corresponding to the end states of the needle and L the effective buckling length of the needle.

The Young's modulus of spring steel is [66]:

$$E = 206 \cdot 10^3 \text{ N/mm}^2 \tag{G.2}$$

For a disk the area moment of inertia is determined by:

$$I = \frac{\pi \cdot r^2}{4} \tag{G.3}$$

Hulburt *et al.* [67] determined the k-factor for a 22 Gauge needle of stainless steel that was inserted 50 mm into gelatin (10%). We assumed that the buckling node is comparable to needle insertion of the WASP in gelatin and took the average of the measured k-factors:

$$k = 0.780 \text{ mm} \tag{G.4}$$

The length of the needle rod from the distal end of the brass tubes to the distal end of the needle rods is varying between 60 mm and 120 mm. We took the maximum length of:

$$L_{max} = 120 \text{ mm} \tag{G.5}$$

The radius of one needle rod is:

$$r_{rod} = 0.15 \text{ mm} \tag{G.6}$$

The corresponding critical buckling load for one needle rod is:

$$P_{cr-rod} = \frac{\pi^2 \cdot 206 \cdot 10^3 \cdot 3.976 \cdot 10^{-4}}{(0.78 \cdot 120)^2} = 0.092 \text{ N} \tag{G.7}$$

The radius of the needle bundle is:

$$r_{bundle} = 0.45 \text{ mm} \tag{G.8}$$

The corresponding critical buckling load for the needle bundle is:

$$P_{cr-bundle} = \frac{\pi^2 \cdot 206 \cdot 10^3 \cdot 0.151}{(0.78 \cdot 120)^2} = 7.474 \text{ N} \tag{G.9}$$

H. Miura-tube pattern

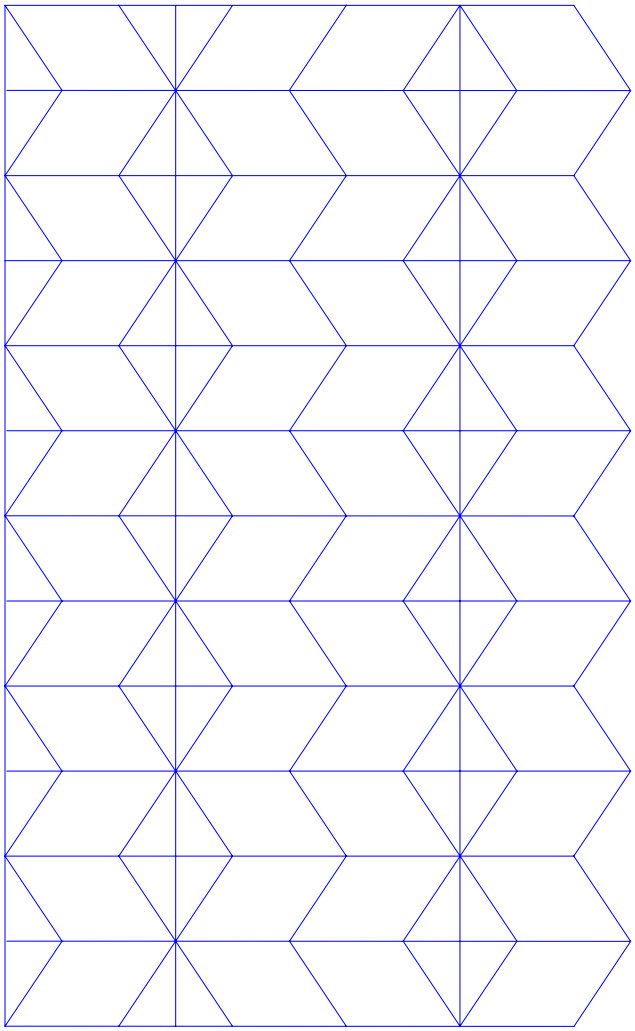

	units mm	scale 1:1	quantity 1	date 30-10-2023	
material			mass gr		
author Zola Fung-A-Jou				TU Delft Delft University of Technology	
name Modified Miura pattern H:\My Documents\Afstuderen\Origami\				format A4	drawing no.

I. Technical drawings of the prototype

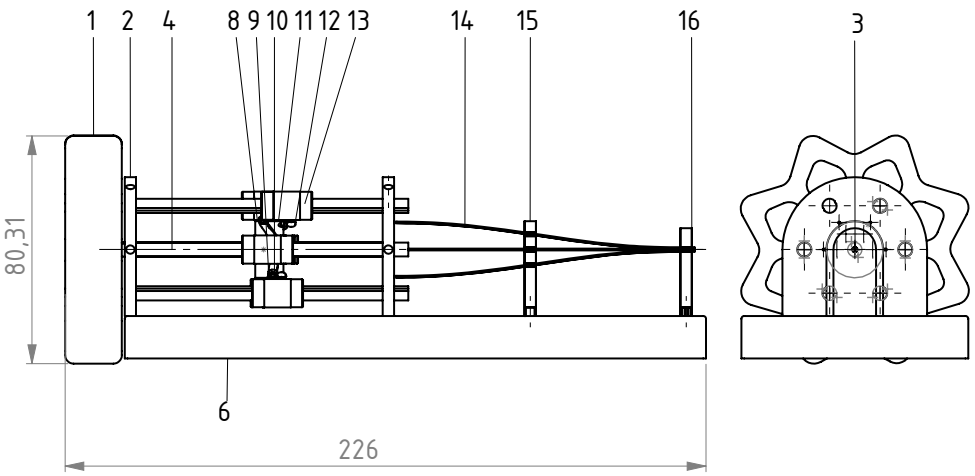

ITEM NO.	PART NUMBER	QTY.
1	Knob	1
2	Support block	2
3	Ball bearing	2
4	Drive cylinder	7
6	Base plate	1
8	Cam	1
9	Follower	6
10	Axis	6
11	Key	6
12	Rod holder	6
13	Follower cylinder	7
14	Rod support	6
15	Tube support middle	1
16	Tube support end	1

	units mm	scale 1:2	quantity 1	date 30-10-2023
material			mass gr	
author Zola Fung-A-Jou				TU Delft Delft University of Technology
name Final concept H:\My Documents\SolidWorks 2022\SW Files\			format A4	drawing no. 1

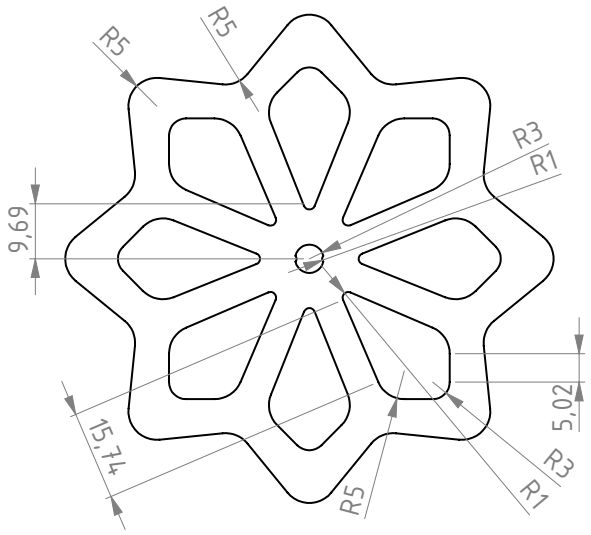

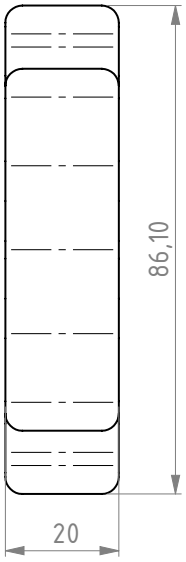

	units mm	scale 1:1	quantity 1	date 29-11-2023	
material				mass gr	TU Delft Delft University of Technology
author Zola Fung-A-Jou					
name Knob				format A4	drawing no. 2

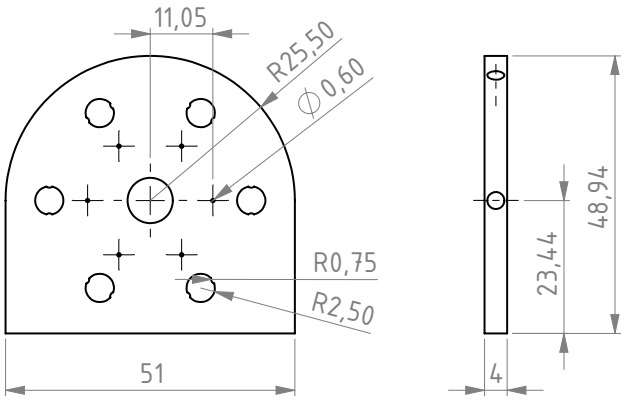

	units mm	scale 1:1	quantity 2	date 29-11-2023	
material				mass gr	TU Delft Delft University of Technology
author Zola Fung-A-Jou					
name Support block				format A4	drawing no. 3

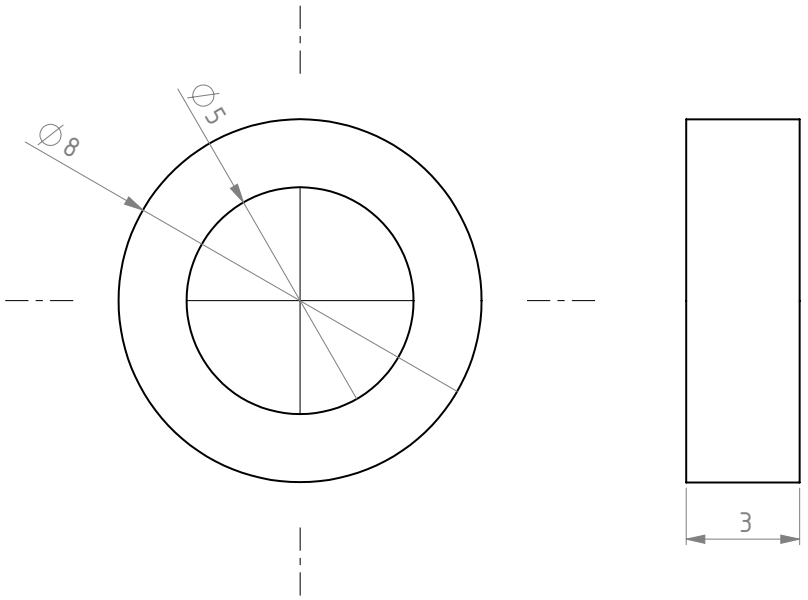

	units mm	scale 8:1	quantity 2	date 29-11-2023	
material				mass 0.08gr	TU Delft Delft University of Technology
author Zola Fung-A-Jou					
name Bearing				format A4	drawing no. 4

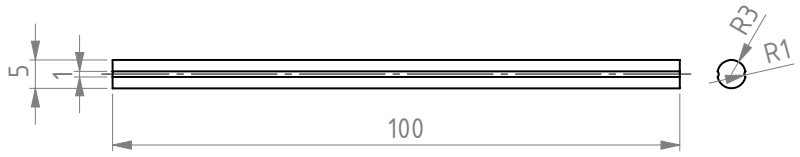

	units mm	scale 1:1	quantity 7	date 29-11-2023	
material				mass gr	
author Zola Fung-A-Jou					TU Delft Delft University of Technology
name Drive cylinder				format A4	drawing no. 5

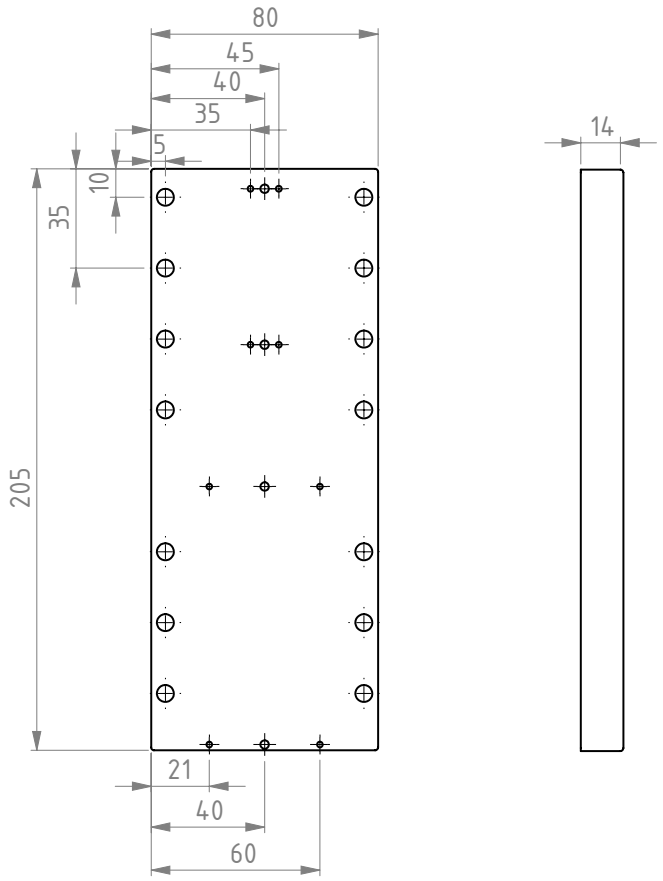

	units mm	scale 1:2	quantity <<nr>>	date 29-11-2023	
material				gr	
author Zola Fung-A-Jou					TU Delft Delft University of Technology
name Baseplate				format A4	drawing no. 6

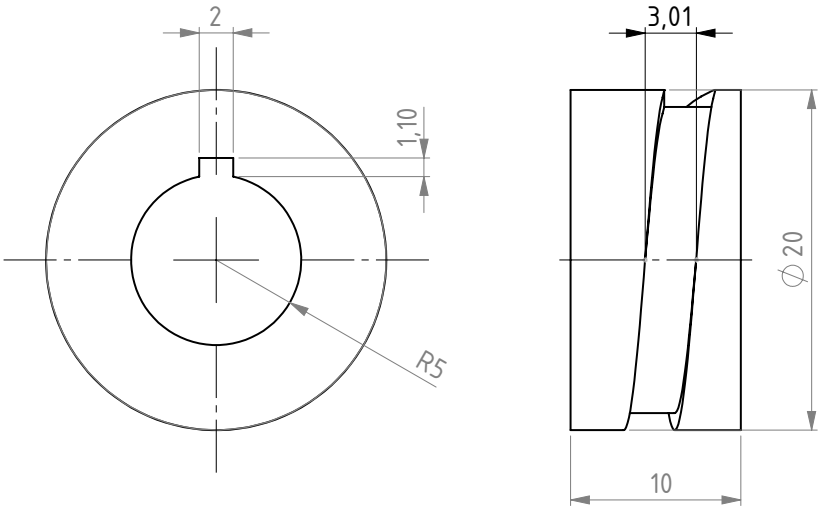

	units mm	scale 3:1	quantity 1	date 29-11-2023	
material	7075-T6, Plate (SS)			mass gr	
author	Zola Fung-A-Jou				TU Delft Delft University of Technology
name	Cam			format A4	drawing no. 7

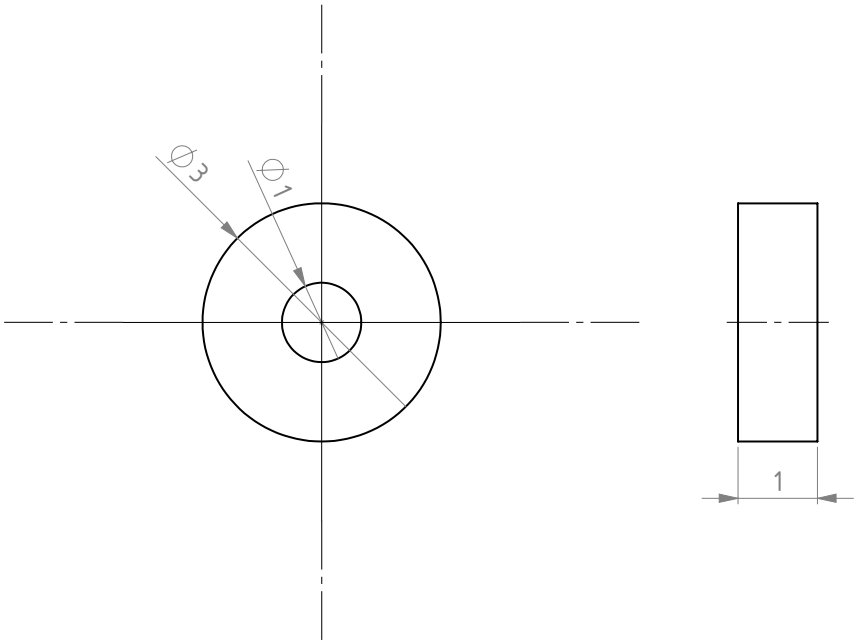

	units mm	scale 14:1	quantity 6	date 29-11-2023	
material				mass gr	
author Zola Fung-A-Jou					TU Delft Delft University of Technology
name Cam follower				format A4	drawing no. 8

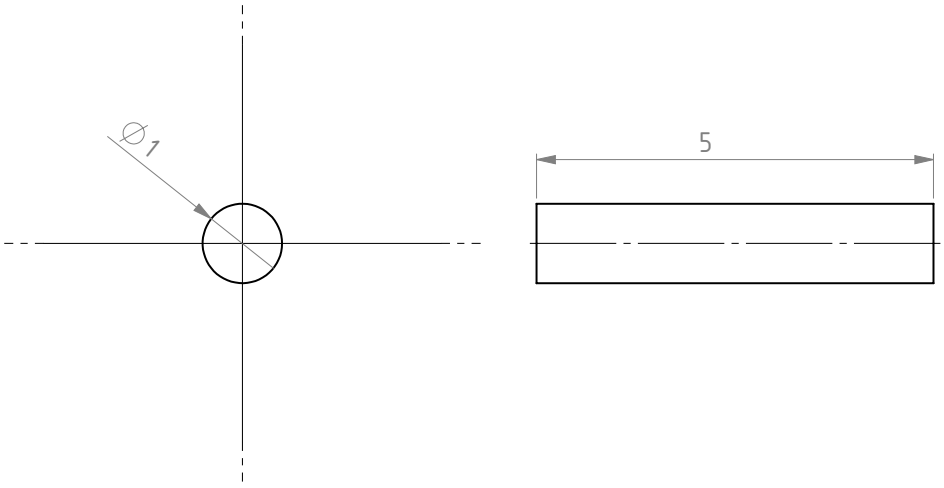

	units mm	scale 14:1	quantity 6	date 29-11-2023	
material	Material <not specified>			mass gr	
author Zola Fung-A-Jou					TU Delft Delft University of Technology
name Axis				format A4	drawing no. 9

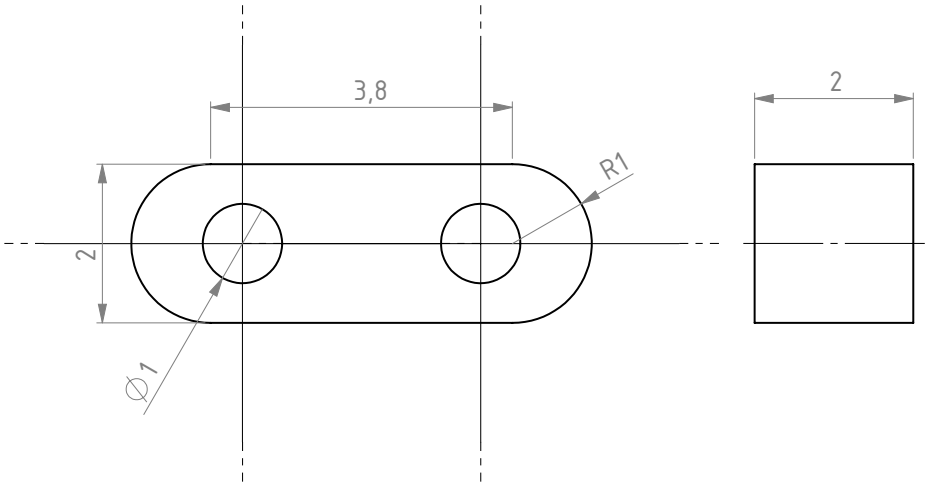

	units mm	scale 14:1	quantity 6	date 29-11-2023	
material	Material <not specified>			mass gr	TU Delft Delft University of Technology
author	Zola Fung-A-Jou				
name	Key			format A4	drawing no. 10

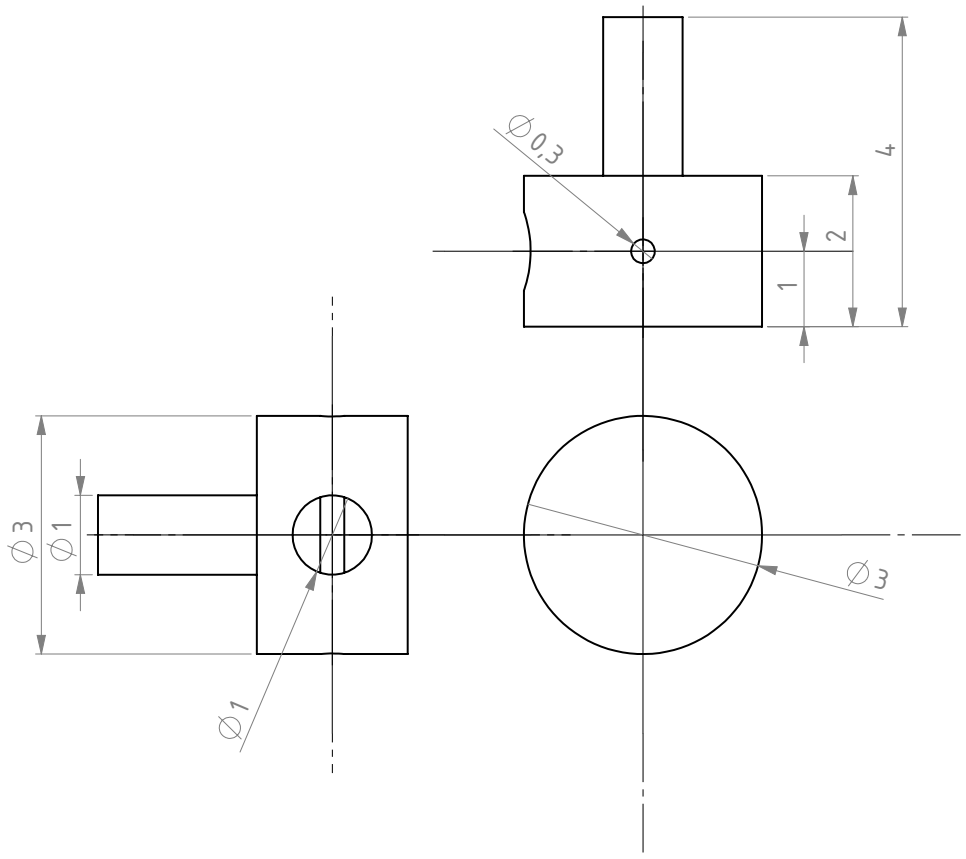

	units mm	scale 14:1	quantity 6	date 29-11-2023	
material				mass gr	
author Zola Fung-A-Jou					TU Delft Delft University of Technology
name Rod holder				format A4	drawing no. 11

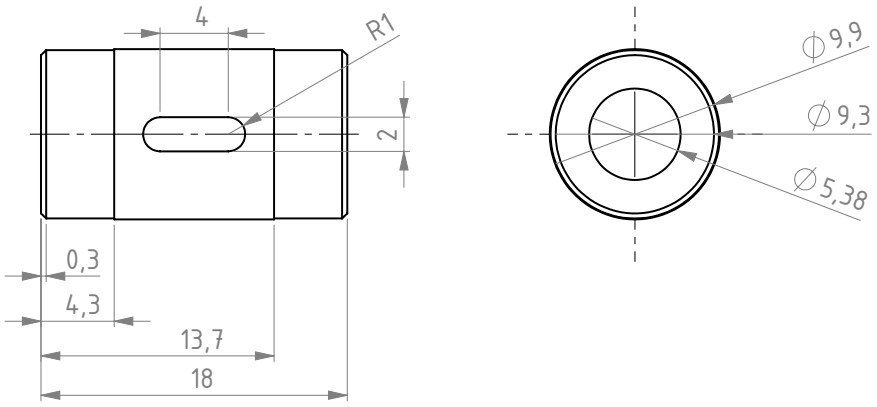

	units mm	scale 3:1	quantity <<7>>	date 29-11-2023	
material				mass gr	
author Zola Fung-A-Jou					TU Delft Delft University of Technology
name Follower cylinder				format A4	drawing no. 12

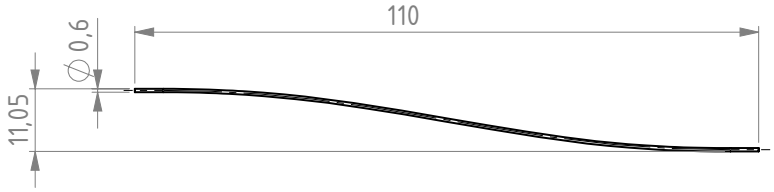

	units mm	scale 1:1	quantity <<nr>>	date 29-11-2023	
material	Material <not specified>			mass gr	
author Zola Fung-A-Jou					TU Delft Delft University of Technology
name Rod support				format A4	drawing no. 13

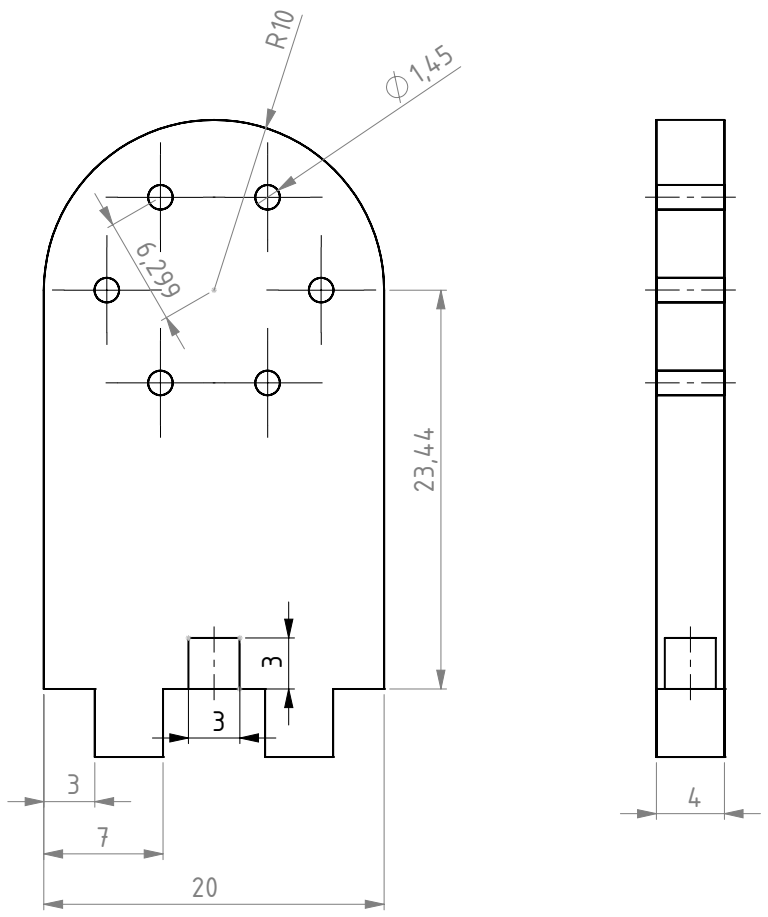

	units mm	scale 3:1	quantity 1	date 29-11-2023	
material	Material <not specified>			mass gr	
author	Zola Fung-A-Jou				TU Delft Delft University of Technology
name	Tube support middle			format A4	drawing no. 14

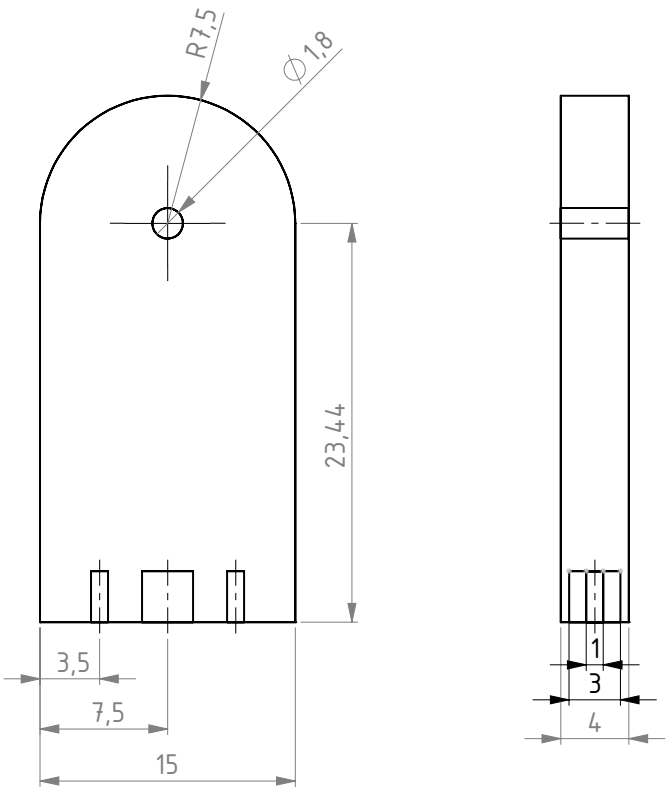

	units mm	scale 3:1	quantity 1	date 29-11-2023	
material	Material <not specified>			mass gr	TU Delft Delft University of Technology
author	Zola Fung-A-Jou				
name	Tube support end			format A4	drawing no. 15